Mean motion resonances among the small satellites of Saturn and Pluto

Thamiris de Santana

Mean motion resonances among the small satellites of Saturn and Pluto

Thesis submitted to the School of Engineering of Guaratinguetá, São Paulo State University, in partial fulfillment of the requirements for the degree of Doctor of Philosophy.

Advisor: Professor Dr. Othon Cabo Winter
Co-advisor: Professor Dr. Douglas P. Hamilton

Guaratinguetá

2019

unesp

UNIVERSIDADE ESTADUAL PAULISTA
CAMPUS DE GUARATINGUETÁ

THAMIRIS DE SANTANA

ESTA TESE FOI JULGADA ADEQUADA PARA A OBTENÇÃO DO TÍTULO DE
"DOUTOR EM FÍSICA"

PROGRAMA: FÍSICA

APROVADA EM SUA FORMA FINAL PELO PROGRAMA DE PÓS-GRADUAÇÃO

Prof. Dr. Konstatin Georgiev Kostov
Coordenador

BANCA EXAMINADORA:

Othon Cabo Winter

Prof. Dr. OTHON CABO WINTER
Orientador / UNESP/FEG

Prof. Dr. SILVIA MARIA GIULIATTI WINTER
UNESP/FEG

Rodney Gomes

Prof. Dr. RODNEY DA SILVA GOMES
Observatório Nacional - RJ

Prof. Dr. TABARÉ GALLARDO CASTRO
Universidad de La Republica de Uruguay

P. Nicholson.

Prof. Dr. PHILIP DAVID NICHOLSON
Cornell University

Outubro de 2019

Curricular data

Thamiris de Santana

BORN	06.01.1991 - GUARUJÁ / SP
FILIATION	Ariovaldo Antônio de Santana Egle Varela Carlota
2009 - 2012	Lic. in Mathematics School of Engineering, Guaratinguetá UNESP - Sao Paulo State University
2013 - 2015	Master in Physics School of Engineering, Guaratinguetá UNESP - Sao Paulo State University
2015 - 2019	Ph.D. in Physics School of Engineering, Guaratinguetá UNESP - Sao Paulo State University
2017 - 2018	Sandwich Ph.D. in Orbital Dynamics Department of Astronomy University of Maryland, USA

For all women before me, with me and after me.

Thanks

I would like to thank everyone who has been by my side in recent years. In special:

To Rafael Sfair, my life partner and loyal friend at all times, who countless times was the one who pushed me forward like a migrating body who locked a small moon with him, he never let me give up during the hard path of the life grad.

To Othon, my advisor, who is always present and available to share his enormous knowledge about science and everything else. He has always been lavish about the time devoted to me, and he was the one that bet I could do this. In the end, it looks like he was right.

To my co-advisor Doug Hamilton, who was so generous in sharing with me his brilliant way of looking at science. He provided me with one of the most remarkable moments of my academic and personal life during my time at the University of Maryland.

To Radwan Tajeddine, who invited me for a unique opportunity to collaborate at Cornell University, of which I will be forever grateful.

To my friends Patricia, Amira, Hanik, Stela, and Helena that I could always count on to let off steam. They reminded me that there is life outside the university, or I would perish.

To Bruno Morgado for the partnership. To Thomas and Zeeve to kindly receive me at UMD.

To Daniela Mourão and Maryame El Moutamid for their essential collaboration in this work.

To all my graduate friends, especially Rafael Ribeiro, Barbara, and Tamires, for sharing the life of the graduate

To my students, for professional growth. They never let me forget that it was for the joy of knowing and transmitting the knowledge that all this began.

To my teachers, for sharing their knowledge with me so generously and provide me with challenging times that have made me evolve.

To my family, for all their support over all these years, understanding my absence at some important moments.

This study was financed in part by the Coodernação de Aperfeiçoamento de Pessoal de Nível Superior- Brasil (CAPES) - Finance Code 001

Sometimes science is more art than science.

(Rick Sanchez)

SANTANA, T. **Mean motion resonances among the small satellites of Saturn and Pluto**. 2019. 103 p. Thesis (PhD in Physics) - Sao Paulo State University (UNESP), School of Engineering, Guaratinguetá, 2019.

Abstract

This work is organized into three parts. In Part I, we present a quick review of Saturn's satellites Prometheus and Pandora lags problem. We analyzed the lags ratio $\left(\mathcal{Q} = \left|\frac{\Delta\lambda_{\rm pro}}{\Delta\lambda_{\rm pan}}\right|\right)$ through the conservation of the angular momentum, that implies the ratio of the lags due to this mutual interaction must be almost constant. However, we found that the values obtained using observational data fit $\mathcal{Q}_{\rm obs}$ does not agree with the assumed masses $m_{\rm pan}/m_{\rm pro} = 0.56$ and is not even nearly constant. It presents a robust linear increasing rate given by $\mathcal{Q}_{\rm obs}(t) = 0.667 + 0.013t$, with t given in years. In this way, we show that only the gravitational interaction between the satellites does not fully explain the lags values. This indicates that a non-mutual mechanism should provoke at least a mean motion changing of 0.45°/year, also affecting Prometheus or Pandora, contributes to the lag values.

In Part II, we performed the astrometry of the satellite Daphnis using the Caviar software in a selected set of images from the ISS-NAC camera of Cassini spacecraft. Daphnis' astrometry of all Cassini mission period showed that Daphnis had changed its orbit twice. So, we have investigated the stability of Daphnis' orbit by implemented numerical simulations considering Saturn plus five satellites: Daphnis, Atlas, Prometheus, Pandora, and Mimas and computing the evolution of the Fast Lyapunov Indicator FLI. We showed that Daphnis is on a chaotic orbit with a Lyapunov time of ∼13 years. By investigating possible resonances between Daphnis and other satellites, we found that Prometheus and Atlas with 129:125 and 157:155 mean motion resonant angles, respectively, present some features that could indicate chaos. Additionally, we found that when Prometheus and Atlas are not included in the numerical simulation, Daphnis' orbit became regular, reinforcing the suggestion that both satellites are playing a role in Daphnis' chaotic behavior.

In Part III, we presented a study of the origin of resonance between the satellites of Pluto. We performed N-body numerical simulations considering the small satellites and Charon evolving under the influence of the tidal force due of Pluto on Charon. Using the J_2 *effective* approach, we showed that the small satellites could be captured into the 3:1, 4:1, 5:1, 6:1 mean motion resonances with Charon. Even for the case of the 5:1 and 6:1 mean

motion resonances, it was possible to achieve a capture only when some non-zero eccentricity was added to Charon. Moreover, the 3:1 mean motion resonance between Charon and Styx, in inclination, was the easiest to happen. To find the three body resonance 3:5:2 among Styx, Nix, and Hydra, we looked for two particular resonances among them: 2:1 between Styx and Hydra and 5:4 between Nix and Styx. We have found parameters that allow the capture of the small bodies into the exact two 2-body resonant arguments we need, but not at the same time. In this way, we perceive that we are close to finding the right parameters to represent all the paths of the Pluto's moons from their past to the current intriguing configuration. Some different ideas may be tested to bring us to the present scenario.

Keywords: Resonances, satellites, Saturn, Pluto.

SANTANA, T. **Ressonâncias de movimento médio entre pequenos satélites de Saturno e Plutão.**. 2019. 103 p. Tese (Doutorado em Física) - Faculdade de Engenharia do Campus de Guaratinguetá, Universidade Estadual Paulista, Guaratinguetá, 2019.

Resumo

Este trabalho está dividido em três partes.

Na Parte I é apresentada uma breve revisão sobre o problema da defasagem dos satélites Prometeu e Pandora de Saturno. Analisamos a razão entre as defasagens $\left(\mathcal{Q} = \left|\frac{\Delta\lambda_{\rm pro}}{\Delta\lambda_{\rm pan}}\right|\right)$ através da conservação do momento angular, o que implica que o fator $\mathcal{Q}$ devido à perturbação deve ser praticamente constante. Contudo, verificou-se que os valores ajustados a partir de dados observacionais $\mathcal{Q}_{\rm obs}$ não está de acordo com a razão de massas assumidas $m_{\rm pan}/m_{\rm pro} = 0.56$ e também não tem um comportamento constante. Verificou-se que há um aumento linear dado por $\mathcal{Q}_{\rm obs}(t) = 0.667 + 0.013t$, com t dado em anos. Desta forma mostrou-se que somente a interação gravitacional entre os satélites não explica completamente os valores das defasagens. Isso indica que algum mecanismo não-mútuo deve causar pelo menos uma alteração no movimento médio de $0.45°$/ano de Prometeu ou Pandora e contribui para os valores das defasagens.

Na Parte II é realizada a astrometria do satélite Daphnis utilizando o software CAVIAR para um conjunto selecionado de imagens da câmera ISS-NAC da sonda Cassini. A astrometria do satélite para todo o período da missão Cassini mostrou que Daphnis mudou sua órbita duas vezes. Assim, foi investigada a estabilidade orbital de Daphnis através de simulações numéricas considerando Saturno e cinco satélites (Daphnis, Atlas, Prometeu, Pandora e Mimas) e calculando a evolução do Indicador Rápido de Lyapunov. É mostrado que Daphnis está em uma órbita caótica com um tempo de Lyapunov de $\sim$22 anos. Investigando possíveis ressonâncias entre Daphnis e outros satélites, verificou-se que as ressonâncias 129:125 e 157:155 com Prometeu e Atlas, respectivamente, apresentam algumas características que podem indicar caos. Adicionalmente, em simulações numéricas sem os satélites Prometeu e Atlas a órbita de Daphnis permaneceu regular, reforçando a idéia que são estes dois satélites que tem um papel relevante no comportamento caótico de Daphnis.

Na Parte III é apresentado um estudo da origem das ressonâncias entre os satélites de Plutão. Foram realizadas simulações numéricas do problema de N-corpos considerando os pequenos satélites e Caronte, incluindo a migração de Caronte devido à força de maré. Utilizando a abordagem do J_2 *efetivo* mostrou-se que os pequenos satélites podem ser capturados nas ressonâncias de movimento médio 3:1, 4:1, 5:1, 6:1 com Caronte. Para os casos das ressonâncias 5:1 e 6:1 foi possível obter uma captura somente quando uma excentricidade não nula foi considerada para Caronte. Além disso, a ressonância de movimento médio 3:1 em inclinação entre Caronte e Estige é a mais fácil de ocorrer. Para encontrar a ressonância de três corpos 3:5:2 entre Estige, Nix e Hidra procurou-se por duas ressonâncias específicas entre os satélites: 2:1 entre Estige e Hidra, e 5:4 entre Nix e Estige. Foram encontrados parâmetros que permitem a captura dos pequenos satélites exatamente com os argumentos das ressonâncias de dois corpos necessárias, porém não simultaneamente. Desta forma, sabe-se que é um caminho promissor para determinação dos parâmetros para representar a evolução dos satélites de Plutão até suas posições atuais.

Palavras-chave: Ressonâncias, satélites, Saturno, Plutão.

List of Figures

List of Tables

Contents

Chapter 1

Introduction

In this work, we present three different dynamic systems of small bodies under the influence of mean motion resonances.

The text is divided into three independent parts. In Part I, we present a quick review of Saturn's satellites Prometheus and Pandora lags problem, defined by the difference in their angular positions found fifteen years after their discovery. In Chapter 2, we present a bibliographical review of the works on this topic. In Chapter 3, we show the implications of the conservation of angular momentum on this system, and we show the ratio between the lags will be nearly constant and inversely proportional to the ratio of their masses. Chapter 4 is devoted to the discussion of the evolution of the ratio between the lags, and later it is presented a brief discussion on the satellites mass ratio related to those values. We highlight some known interaction with Prometheus or with Pandora that could be causing the anomaly found, and the final comments on this part are presented.

In Part II, we show a study regarding the Daphnis satellite, starting from the analysis of its images taken by Cassini to its orbit. In Chapter 5, we introduce the satellite and its discovery by Cassini. Chapter 6 presents the process to make the astrometry of Daphnis using Caviar. By using images from 2004 to 2014, it is shown that Daphnis has changed its orbit. So, in Chapter 7 Fast Lyapunov Indicator (FLI) is presented, by performing numerical simulations we investigate the stability of Daphnis orbit, and we show its chaotic movement. Moreover, we investigate if there are any moons related to Daphnis chaotic behavior and analyzing mean motion resonances. It also contains the final comments on this part.

Finally, in Part III, we present a study of the origin of the resonance between the satellites of Pluto. In Chapter 8, we describe the system and its particular configuration. Chapter 9 presents our methodology and how we proceed to take Charon's presence into account to analyze the small satellites orbits. In Chapter 10, we show the numerical simulations, analyze the results and it contains the final comments on this part.

Chapter 11 summarizes all the three parts of the work, highlighting the main results.

Part I

Prometheus and Pandora

Chapter 2

Introduction

2.1 Two small satellites graze a ring

Saturn, the second largest planet in our Solar System, is mainly composed of hydrogen and helium, and it has about 100 Earth masses. So far, 62[1] satellites are known orbiting Saturn (Giorgini et al. 1996), and the planet hosts the most extensive ring system among the planets. The denser part of the ring covers a region almost 70,000 km wide, while the dusty rings extend beyond the orbit of the irregular satellite Phoebe.

The called main ring system is composed of the A, B, C, and D rings. The innermost and fainter is the D ring, followed by the C ring. Moving further from the planet are the B and A rings, separated by the Cassini Division, a region with low optical depth. Within the A ring is located the Encke gap, a 325 km region where the moon Pan orbits (Porco et al. 2005). Beyond the edge of the A ring are the F, G, E, and Phoebe rings.

The narrow F ring lies just outside the A ring, and it is the most studied ring due to a large number of unusual structures it presents, such as braids, gaps, and clumps. The F ring is followed by two small satellites, Prometheus close to the inner edge, and Pandora that is exterior to the ring.

Prometheus and Pandora were discovered by Voyager images in 1980 (Synnott et al. 1981, 1983). Prometheus, originally S/1980 S27, has an irregular shape, presents craters up to 20 km in diameter, and it has a low density, indicating a high porosity. The satellite orbits at $139,353.43$ km from Saturn and its orbital period is $\sim 14,4$ hours[2].

Pandora, first named as S/1980 S26, is covered by a fine layer of dust that makes its surface smoother than other comparable moons. Its semi-major axis is $141,711.61$ km and it takes $\sim 15,1$ h to complete an orbit around Saturn[1].

Initially, it was believed that Prometheus and Pandora shepherd the F ring similarly to the proposed model for the ϵ of Uranus (Goldreich & Tremaine 1979). However, the torques from the satellites into the ring edges do not compensate as it is required to confine the particles (Lissauer & Peale 1986) (See Fig. 2.1).

Since the discovery, the orbits of the satellites have been followed. Fifteen years after Voyager observation, the Saturn ring-plane crossing (RPX), when the Earth crosses through

[1]Twenty new more moons were just announced!
[2]saturn.jpl.nasa.gov/ .

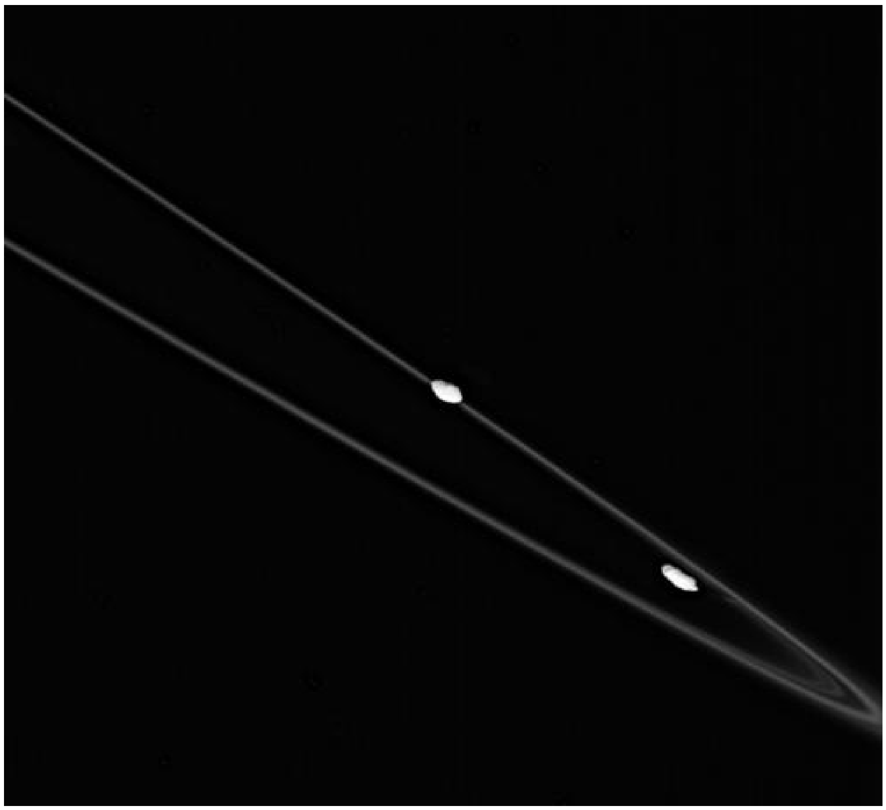

Figure 2.1: Prometheus, Pandora and the F ring in a Cassini image. Pandora is the moon on the left and Prometheus on the right. Source: NASA/JPL/Space Science Institute

Saturn's ring plane (RPX) happened. At this time, the light scattered from the rings was markedly reduced due to an edge-on configuration, and it was possible to observe the small inner satellites of the Saturn system, including Prometheus and Pandora, using the Hubble Space Telescope (HST). These images revealed that the satellites were at orbital longitudes quite different than expected by extrapolation of Voyager data.

Nicholson et al. (1996) and Bosh & Rivkin (1996), using Voyager data as a starting point, performed numerical integrations of Prometheus' orbit over 15 years assuming a two-body problem (Saturn and Prometheus), taking into account the oblateness of Saturn. The difference between the estimated mean longitude of Prometheus and that observed by HST was found to be -19 degrees.

Different explanations were proposed to account for this lag of Prometheus. Murray & Giuliatti Winter (1996) suggested a physically encroach upon the F-Ring by Prometheus that would occur every 19 years. Barbara & Esposito (2002), following the work by Cuzzi & Burns (1988) regarding a belt of moonlets that occupies the radial region between Pandora and Prometheus, studied the gravitational perturbations by these unseen moonlets on Prometheus. Showalter et al. (1999b,a) argued that the quasi-periodic clumping production of F-ring material caused by close approaches of Prometheus could produce a push back in itself.

Initially, Pandora was at around predicted location. However, using data from a different period of the RPX, McGhee (2000) found that Pandora also presented a lag ahead of predicted position. The value was found to be around $+25$ degrees (McGhee et al. 2001, Evans 2001, French et al. 2003).

To explain both satellites being at different positions, several authors investigate distinct mechanisms. Esposito (2002) explored effects of hypothetical unseen moonlets (10 km of radius), small enough to be missed in Voyager images, whose random gravitational interaction with Prometheus and Pandora could result in an errant behavior of the satellites. The tidal force and resonances in the F-ring region were analyzed by Poulet & Sicardy (2001) . They explored a possible resonant capture for the satellites, but it was shown that such mechanism is inefficient and transient.

French et al. (2003) carried out a deep astrometric analysis and fitted orbits for Prometheus and Pandora. They propose a common origin for the wandering movement of the satellites that could be related to a resonance involving the F-ring.

Another resonant mechanism was pointed out by Renner & Sicardy (2003) to explain the chaotic behavior of the system. The overlap of four apse-type arguments from the 121:118 mean motion resonance between Prometheus and Pandora would be the origin of chaos.

Goldreich & Rappaport (2003a), taking into account that the two satellites are exchanging energy and angular momentum, found that their orbits are chaotic and every 6.2 year they would present a significant change in their mean longitudes. This 6.2 year period is related to the anti-alignment of the orbits periapses, a configuration where the satellites are closer to each other, and the interactions between them are stronger.

In a following work, Goldreich & Rappaport (2003b) proposed the same mean motion resonance 121:118 between the satellites pointed out by Renner & Sicardy (2003) as responsible for the chaotic behavior of the satellites that would result in the observed lags. This resonance has four arguments, and, due to the pericentre precession caused by Saturn's non-spherical shape, the widths of the libration amplitude of these arguments are overlapped, originating the chaos. Numerical simulations performed by the authors were compatible with the observed lags.

Based on the solution presented by Goldreich & Rappaport (2003b) and Renner & Sicardy (2003), Cooper & Murray (2004) carried out a numerical and analytical study of the orbits of Prometheus and Pandora, including now the gravitational perturbing of other moons. They found out the existence of an anti-correlation in the temporal variation of the mean longitudes of the two satellites and also confirmed the chaotic nature of the Prometheus-Pandora system as indicated by Goldreich & Rappaport (2003a,b). Renner et al. (2005) also confirmed the chaos indicated by Goldreich & Rappaport (2003a,b) through numerical integrations, including the perturbations of other Saturnian satellites and used the HST data to derive the masses of the satellites.

Cruz (2004) proposed a different approach, that argued that the lags could be better understood when the evolutions of the semi-major axes are analyzed. The author argues that chaos is not a main point in the Prometheus and Pandora lags problem.

Currently, the resonant model proposed by Goldreich & Rappaport (2003a,b) is the most accepted explanation for the lags. Since the lags result directly from the mutual interaction between Prometheus and Pandora, the ratio between the lags should be nearly constant due to the conservation of the angular momentum.

However, the observational presented by French et al. (2003) indicates that the ratio between the lags is growing in time. It indicates that an additional mechanism in the theory is necessary to take into account the increase in the ratio between the lags, and that is the problem we aim to discuss in the present work.

In the next section, we start presenting the well-accepted theory briefly to explain the lags on the Prometheus and Pandora positions (Goldreich & Rappaport 2003a,b). Thus, in Chapter 3 we show some implications of the conservation of angular momentum, and Chapter 4 a discussion of the evolution of the ratio between the lags is made and the final comments are presented.

2.2 Chaotic motion of Prometheus and Pandora

Goldreich & Rappaport (2003a) made a careful numerical integration of the Saturn-Prometheus-Pandora system using the Bulirsch & Stoer (1980) algorithm. To perform the numerical simulation, which was named FSHEP, they employed the algorithm derived in Borderies-Rappaport & Longaretti (1994) to convert between cylindrical elements and epicyclic elements. Their goal was to calculate the expected lag for each satellite.

To demonstrate that the lags of Prometheus and Pandora arises from the chaos due to the 121:118 resonance, Goldreich & Rappaport (2003b) integrated a simplified set of the Lagrange's Equations taking into account only the resonant terms from the disturbing function and assuming low eccentricity orbits. They made two different simulations, FSHEPRES and FSHEPSIM. FSHEPRES simulation considered the changes of the semi-major axes, mean longitudes, apsidal angles, and eccentricities of the satellites, while on FSHEPSIM the eccentricities and apsidal angles were assumed to be constant.

Using the Mercury package (Chambers 1999) with the Bulirsch-Stoer algorithm (Bulirsch & Stoer 1980), we were able to reproduce the full numerical integration of Goldreich &

Rappaport (2003a,b) as shown in Fig. 2.2. The same initial conditions used by the authors were considered: $m_{\rm pan} = 3.43\times10^{-10}M_s$, $m_{\rm pro} = 5.80\times10^{-10}M_s$, where $m_{\rm pan}$ and $m_{\rm pro}$ denotes Pandora and Prometheus masses respectively and M_s is the Saturn mass. The oblateness of Saturn up to the term J_6 of its gravitational potential has also been considered and the conversion of the initial osculating orbital elements to the geometric elements were carried out following the work of Renner & Sicardy (2006).

The lags showed in Fig. 2.2 were calculated as the difference between the mean longitudes obtained from the two-body problem (Saturn-Prometheus or Saturn-Pandora) and the three-body problem (Saturn-Prometheus-Pandora). The variation for Pandora ($\Delta\lambda_{\rm pan}$) is always larger, what is expected due to its lower mass when compared with Prometheus.

We can now define the quantity $\mathcal{Q}_{\rm mutual} = \Delta\lambda_{\rm pro}/\Delta\lambda_{\rm pan}$ as the ratio between the lags of Prometheus ($\Delta\lambda_{\rm pro}$) and Pandora ($\Delta\lambda_{\rm pan}$) that are due to the mutual gravitational interaction between them. This parameter is inversely proportional to the mass ratio of the satellites, $\mathcal{Q}_{\rm mutual} \simeq -m_{\rm pan}/m_{\rm pro}$($\simeq 0.59$ for the assumed masses) as will be shown in the next chapter.

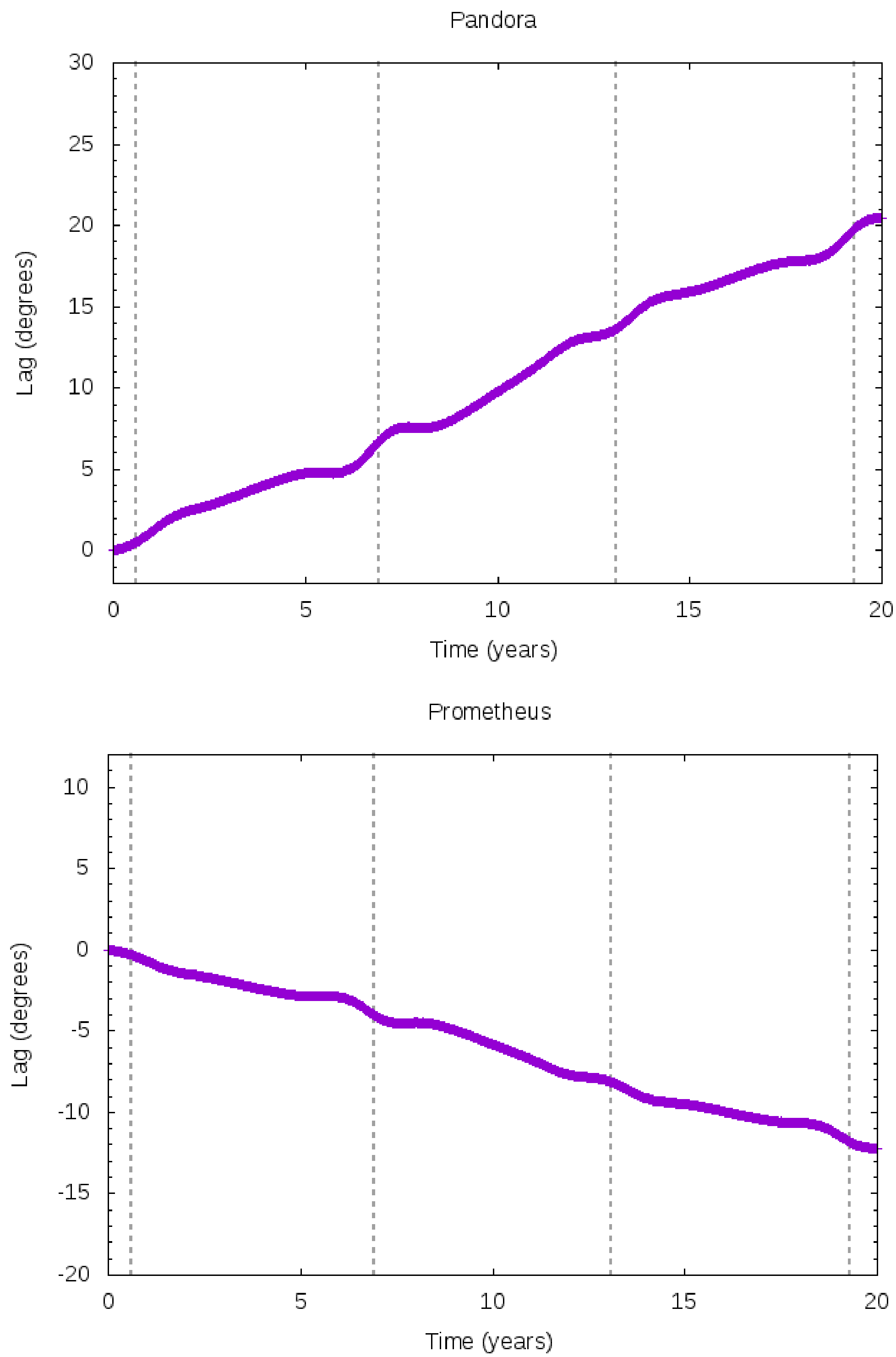

Figure 2.2: Prometheus and Pandora longitude difference in degrees as a function of time, over 20 years. A drift based on the initial mean motion has been subtracted from the longitudes. The masses of Pandora and Prometheus are the same adopted by Goldreich & Rappaport (2003a,b), whose mass ratio is $m_{\rm pan}/m_{\rm pro} = 0.59$. Dashed lines indicate the moment of the orbits periapsis antialignment.

Chapter 3

A mutual mechanism

3.1 Angular momentum conservation

Ignoring external perturbations, the total angular momentum of the Prometheus-Pandora system is given by the sum of the angular momentum of each body and should be a constant quantity. Neglecting the interaction term between the moons and considering small eccentricities ($e \ll 1$), we have

$$L = m_{\mathrm{pro}}\sqrt{\mu a_{\mathrm{pro}}} + m_{\mathrm{pan}}\sqrt{\mu a_{\mathrm{pan}}} = constant, \tag{3.1}$$

where $\mu = G(M_{\mathrm{Saturn}} + M_{\mathrm{satellite}}) \approx G(M_{\mathrm{Saturn}})$, G is the gravitational constant, $M_{\mathrm{satellite}}$ is the satellite mass, M_{Saturn} is the Saturn mass. a_{pro} and a_{pan} are the semi-major axes of Prometheus and Pandora, respectively.

Taking the differential of L with respect to a_{pan} and a_{pro} we can write

$$\Delta a_{\mathrm{pro}} \simeq -\frac{m_{\mathrm{pan}}}{m_{\mathrm{pro}}}\sqrt{\frac{a_{\mathrm{pro}}}{a_{\mathrm{pan}}}}\Delta a_{\mathrm{pan}}, \tag{3.2}$$

with Δa_{pro} and Δa_{pan} begin small variations in the semi-major axes of Prometheus and Pandora, respectively.

Equation 3.2 presents a relation between the changes of the semi-major axes due to the mutual gravitational perturbations of the satellites as a consequence of the conservation of the angular momentum. Since the satellites have semi-major axes very close to each other ($a_{\mathrm{pan}} = 139377.43$ km and $a_{\mathrm{pan}} = 141712.65$ km (Evans 2001)), the square root in equation 3.2 is nearly the unity. Thus, the equation can be rewriten as

$$\frac{\Delta a_{\mathrm{pro}}}{\Delta a_{\mathrm{pan}}} \simeq -\frac{m_{\mathrm{pan}}}{m_{\mathrm{pro}}}. \tag{3.3}$$

We now want to derive an expression for the ratio between the lags of Prometheus and Pandora ($\mathcal{Q}$). If the lags are defined as $\Delta\lambda = \lambda_t - \lambda_0$, and from the definition of the mean longitude ($\lambda = n(t-\tau) + \varpi$), where ϖ is the longitude of the pericenter,we have

$$\Delta\lambda = t(n_t - n_0), \tag{3.4}$$

where t is the time, and n_0 and n_t are the mean motion at the initial and final time, respectively. It was assumed that $\tau = 0$.

Using Kepler's third law, we have

$$\Delta\lambda \simeq t\sqrt{\mu}\left(-\frac{3}{2}\frac{\Delta a}{\sqrt{a^5}}\right). \tag{3.5}$$

so $\mathcal{Q}$ can be written as

$$\mathcal{Q}_{\mathrm{mutual}} = \frac{\Delta\lambda_{\mathrm{pro}}}{\Delta\lambda_{\mathrm{pan}}} \simeq \frac{\Delta a_{\mathrm{pro}}}{\Delta a_{\mathrm{pan}}}. \tag{3.6}$$

This last expression shows that in the case of mutual gravitational interaction between the satellites, where the angular momentum of the system must be conserved, the ratio between the lags will be nearly constant in time and inversely proportional to the ratio of their masses. It is possible to reach an equivalent result from the conservation of energy French et al. (2003).

The validity of this result can be verified in the cases showed in Fig. 2.2. Assuming $m_{\mathrm{pan}}/m_{\mathrm{pro}} = 0.59$ (Goldreich & Rappaport 2003a,b), while from the numerical simulation we have $\Delta\lambda_{\mathrm{pro}}/\Delta\lambda_{\mathrm{pan}} = 0.60$.

Chapter 4

Discussion

4.1 Observed lags ratios

French et al. (2003) determined sky-plane positions for Prometheus and Pandora, their mean longitudes and the lags for several datasets: HST data from 1994, previously not analyzed RPX images, and also a series of images from HST WFPC2 between 1996 and 2002. They calculated the mean longitudes adjusted for HST data and then computed the difference between these values and the mean longitudes extrapolated from the Voyager epoch. Table 4.1 shows some data from this work, considering only the dates when lag values for both satellites are available. There are twenty-one pairs of what we called "observed lags", covering from November 1994 to January 2002. A column with the ratio between the absolute values of the lags of Prometheus and Pandora was added and it is indicated as $\mathcal{Q}_{\rm obs} = \left|\Delta\lambda_{\rm pro}/\Delta\lambda_{\rm pan}\right|$.

Over the time span of seven years, the satellite lags $\Delta\lambda_{\rm pro}$ and $\Delta\lambda_{\rm pan}$ change. It is expected since the mean longitude increases over time. However, the values $\mathcal{Q}_{\rm obs}$ varies from 0.83 up to 0.96 in the same period.

Figure 4.1 shows time variation of $\mathcal{Q}_{\rm obs}$, covering the period from the satellites discovery in 1980 ($t = 0$) up to HST observations. The points indicate the values from Table 4.1, while the purple line is a linear fit of the point. The best fit is given by $\mathcal{Q}_{\rm obs}(t) = 0.013t + 0.667$ with a standard deviation of $\sigma = 0.021$.

The linear regression shows a growing trend at a rate of 0.013 per year. This variation is significant since it was expected this value should be constant according to the angular momentum conservation.

We can also note the pink line, that represents the value of $\mathcal{Q}_{mutual} = 0.56$, was determined with a mass ratio adopted by French et al. (2003) to fit the observational data and were used to compute the lags (black dots). Nevertheless, the actual values of $\mathcal{Q}_{obs}$ from the measured lags are much higher, ranging from 48% up to 68% larger.

Assuming there is an additional effect that changes the satellites' angular positions, we estimate this phenomenon needs to increase the mean motion about 0.45°/year in one of the satellites.

Since Pandora and Prometheus masses are a key factor in this analysis, a brief discussion will be presented, along with a compilation of known physical effects that might be relevant to explain the change in the lag ratio.

	$\Delta\lambda$ Observed Lags (°)		
Date	Prometheus	Pandora	$\mathcal{Q}_{\rm obs}$
November 1994	-19.82 $\pm$ 0.27	23.93 $\pm$ 0.20	0.83
May 1995	-20.41 $\pm$ 0.08	23.98 $\pm$ 0.07	0.85
August 1995	-20.18 $\pm$ 0.18	32.30 $\pm$ 0.22	0.87
August 1995	-20.28 $\pm$ 0.08	23.48 $\pm$ 0.06	0.86
November 1995	-20.40 $\pm$ 0.08	23.00 $\pm$ 0.09	0.89
November 1995	-20.32 $\pm$ 0.16	22.85 $\pm$ 0.16	0.89
September 1996	-20.93 $\pm$ 0.12	24.53 $\pm$ 0.09	0.85
October 1997	-21.82 $\pm$ 0.06	23.82 $\pm$ 0.08	0.92
December 1997	-21.92 $\pm$ 0.07	24.63 $\pm$ 0.14	0.89
October 1998	-22.51 $\pm$ 0.05	25.11 $\pm$ 0.19	0.89
October 1998	-22.55 $\pm$ 0.15	24.95 $\pm$ $0,07$	0.90
August 1999	-22.96 $\pm$ 0.15	24.98 $\pm$ 0.09	0.92
November 1999	-23.19 $\pm$ 0.29	25.70 $\pm$ 0.18	0.90
November 1999	-23.18 $\pm$ 0.11	25.79 $\pm$ 0.22	0.89
August 2000	-23.87 $\pm$ 0.39	25.35 $\pm$ 0.16	0.94
November 2000	-24.20 $\pm$ 0.10	25.08 $\pm$ 0.18	0.96
November 2000	-24.19 $\pm$ 0.19	25.12 $\pm$ 0.19	0.96
December 2000	-24.19 $\pm$ 0.56	25.22 $\pm$ 0.12	0.96
September 2001	-25.39 $\pm$ 0.13	27.70 $\pm$ 0.09	0.91
November 2001	-25.64 $\pm$ 0.56	27.66 $\pm$ 0.12	0.93
January 2002	-25.91 $\pm$ 0.16	27.51 $\pm$ 0.12	0.94

Table 4.1: Observed lags values through Voyager I, II, and HST data. Extracted and adapted from French et al. (2003). The quantity $\mathcal{Q}_{\rm obs}$ is calculated by the ratio between the Prometheus and Pandora lags.

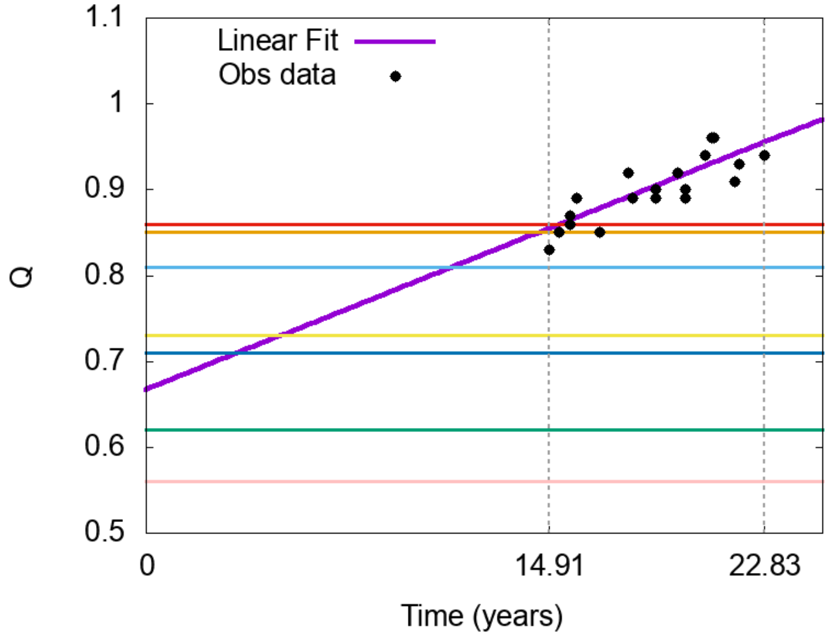

Figure 4.1: Plot of $\mathcal{Q}$ as a function of time. The black dots correspond to the values from observations (Table 4.1), and the vertical dashed lines mark the first and last values. The purple line is a linear regression $\mathcal{Q}_{\rm obs}(t) = 0.013t + 0.667$. $t = 0$ corresponds to 1980 when the satellites were discovered. The horizontal colored lines correspond to different Pandora/Prometheus mass ratio values. From top to bottom: $\mathcal{Q} = 0.86$ in red (Spitale et al. 2006); $\mathcal{Q} = 0.85$ in orange (Jacobson et al. 2008); $\mathcal{Q} = 0.81$ in light blue (French et al. 2003); $\mathcal{Q} = 0.73$ in yellow (Renner et al. 2005); $\mathcal{Q} = 0.71$ in blue (Jacobson & French 2004); $\mathcal{Q} = 0.62$ in green (Goldreich & Rappaport 2003b); $\mathcal{Q} = 0.56$ in pink (French et al. 2003).

4.2 Mass ratio values

To test the coupling between the satellites, French et al. (2003) fitted the observed longitude changes in different three epochs: August 1981, December 1994, and December 2000. The best fit that takes into account both Voyager and HST data presented expressive errors on orbital longitude of 0.41°.

To improve the agreement with the observations, they solved for the mean motion of Prometheus, allowing correction to be applied to Pandora's mean motion at the Voyager epoch and the mass ratio. The best fit to all of longitudes presented in Table 4.1 corresponds to a mass ratio of $m_{\rm pro}/m_{\rm pan} = 0.56$.

According to Eqs. 3.3 and 3.6, assuming the lags in longitudes were generated solely by the gravitational disturbance between Prometheus and Pandora, all the points in the plot should lie around the value $\mathcal{Q} = 0.56$ (pink line in Fig. 4.1). However, the minimum value of $\mathcal{Q}$ from our adjust showed in Table 4.1 is 0.67, and it happens close to the Voyager epoch.

The horizontal lines in Fig. 4.1 were computed for different mass ratios for Pandora and Prometheus. The pink line at 0.56 is from French et al. (2003). For completeness we also indicate other mass ratio values derived by other works: 0.73 from Renner et al. (2005), 0.71 from Jacobson & French (2004), 0.81 from French et al. (2003), 0.86 from Spitale et al. (2006)

and 0.85 from Jacobson et al. (2008).

In some cases, there is an agreement only with the initial $\mathcal{Q}_{\text{obs}}$ values, from 0.83 in November 1994 to 0.87 in August 1995. However, this does not correct the increasing behavior, and this is not consistent with the mass ratio used to derive the data shown in Fig. 4.1.

4.3 Non-mutual effects on the satellites

As it was shown before, the mutual effect between the satellites produces a quantity $\mathcal{Q}$ that must be constant due to the angular momentum conservation. The growing trend identified previously requires the existence of a non-mutual effect, that acts differently in each one of the moons. In fact, this could be a mechanism that affects only one satellite.

We now highlight some interactions with Prometheus or Pandora that could eventually be responsible for this phenomenon that could be worthy of further investigation.

Prometheus is known to act as a sculptor of interesting features on the F-ring of due to their gravitational interaction. Due to the eccentricity and the orbital precession, the distance between the satellite and the ring changes over time, and every 17 the orbital configuration reaches the minimum distance when the orbits are anti-aligned. At this geometry, the moon orbits within the ring, and Prometheus is hit by particles. According to Murray & Giuliatti Winter (1996), these collisions may modify the orbit of the satellite, resulting in a change of longitude of $3°$ in a four months interval. This effect is noticeable, but since the collision happens every two decades, it may not be directly related to the linear increase we have found.

Porco et al. (2005), using images took by Cassini Spacecraft, investigated the small satellites of Saturn. Their model proposes that if the closest approach between Prometheus and the F-ring happens before the satellite's orbit apocenter, Prometheus is going to be dragged backward and experiences a change in its semi-major axis. At the same time, the particles that encounter the satellite are thrown forward, changing their semi-major axes and opening a gap in the F-ring.

Spitale et al. (2006) derived the orbits of some of Saturn's small satellites through the combination of images from the Cassini Spacecraft. They pointed out that Prometheus is strongly disturbed by Atlas due to a possible 54:53 mean motion resonance. The resonance introduces a periodic perturbation with an amplitude of about 600 km and a period of around 3 yrs. This was investigated further by Cooper et al. (2015) and Renner et al. (2016). Another possibility is the 70:67 mean motion resonance between Atlas and Pandora with an amplitude of around 150 km. These two resonances open the possibility that the satellite Atlas could be responsible for the effect measured for the lags.

Spitale et al. (2006) also identified a 16:15 mean motion resonance between Prometheus and Pan. They found an effect of a nearby 16:15 inner mean longitude resonance with Prometheus with a libration period of near 108 days and an amplitude of about 3 km in the in-orbit direction.

A numerical simulation considering ten major Saturn satellites was carried out by Cooper & Murray (2004). They identified that both Prometheus and Pandora are close to mean motion resonances with Epimetheus: 17:15 for and 21:19, respectively. Since Epimetheus switches position with Janus, these resonances sweep locations. Moreover, even neglecting

Pandora's effect, they showed that Janus and Epimetheus seem to play a role in Prometheus's chaotic movement.

The interaction between Prometheus and the A-ring was analyzed by Tajeddine et al. (2017). A 32:31 Lindblad resonance was found, which raises the possibility that that different groups of particles from the inner edge of A-Ring may be reacting differently to the resonance with Prometheus, with variations in the forced eccentricity and/or in the pericenter.

An effect that could act only in Pandora is the known 3:2 mean motion resonance with Mimas. Such effect was quantified in terms of Pandora's longitude offset by French et al. (2003) (Table 6, last column). A straightforward analysis shows that the values are too small and do not present the trend profile needed to explain the $\mathcal{Q}$ parameter issue.

There are other interactions not listed here, for instance, the one among Prometheus with ringlets (Winter et al. 2006, Porco et al. 2005, Hedman & Carter 2017), and the waves (Tajeddine et al. 2017, Hedman & Nicholson 2019). At first look, they are not relevant to provoke significant changes in the satellite orbits.

4.4 Final Comments on Part I

In this study we briefly review the Prometheus-Pandora lags problem focusing on the anlaysis of the ratio between the lags denoted by $\mathcal{Q} = \left|\Delta\lambda_{\rm pro}/\Delta\lambda_{\rm pan}\right|$.

The explanation proposed by Goldreich & Rappaport (2003b) for the lags is related to the 121:118 mean motion resonance between Prometheus and Pandora. Through the conservation of the angular momentum, it can be shown that due to the mutual interaction between the satellites, $\mathcal{Q}$ must be almost constant. However, the values obtained using observational data fit French et al. (2003), denoted $\mathcal{Q}_{\rm obs}$, do not agree with the assumed masses for the satellites $m_{\rm pan}/m_{\rm pro} = 0.56$. Furthermore, the lag ratio is not even nearly constant, presenting instead a clear linear increasing trend given by $\mathcal{Q}_{\rm obs}(t) = 0.667 + 0.013t$, with t given in years.

In this way, we showed that only the gravitational interaction between the satellites could not account for explaining all the lags values. There must be an additional non-mutual mechanism that causes a mean motion change of $0.45°$/year.

We have listed a set of known gravitational interactions involving Prometheus and/or Pandora. However, it is necessary to investigate further each phenomenon to identify and quantify those that might be responsible for the discrepancies found. This careful and detailed analysis is beyond the scope of the current work.

Part II

Daphnis

Chapter 5

Introduction

In this chapter, we present a study about the behavior of a Saturn's small moon called Daphnis, discovered by Cassini in 2004. We made a complete work starting from the moon's astrometry up to the analysis of its orbit through numerical simulations, considering Daphnis and others Saturn's moons to better understand some unexpected results derived from Cassini observations.

The astrometry of the satellite and pointed out that Daphnis has changed its orbit twice during the mission years, first in late 2010 and then in early 2016.

From this discovery, we wanted to investigate the possibility of Daphnis being in a chaotic orbit. Using RADAU, we run simulations taking into account Daphnis, Atlas, Prometheus, Pandora, and Mimas, and calculated the Fast Lyapunov Indicator (FLI) (Froeschlé et al. 1997, Froeschlé & Lega 2000). The simulations revealed that Daphnis has a chaotic orbit.

One possibility for provoking this chaos is the presence of resonances between Daphnis and other moons close by. We explore this idea simulating Saturn, Daphnis plus five other satellites, looking for the mean motions resonances near to Daphnis.

5.1 Discovery

The mission Cassini was launched to explore the Saturn system in 1997. A cooperation by NASA, European Space Agency (ESA) and the Italian space agency, Agenzia Spaziale Italiana (ASI), Cassini was one of the most successful missions in the planetary exploration history. This spacecraft explored in detail the most extraordinary features of Saturn system, by orbiting it and diving into the rings during the last phase of the mission, the Grand Finale, bringing to humanity a knowledge about these structures never achieved before.

The mission lasted more than twenty years in space. This long period made it possible to reach many observational goals for the first time, like the resolutions and geometries of the images never seen before, and also the possibility to follow the evolution of rings structures closely for more than one decade.

The Cassini Imaging Science Subsystem (ISS), during the year of 2004, started to produce a lot of data from the system, allowing a more detailed study of the small internal satellites, the ring system and its gaps (Fig. 5.1).

Images took by the ISS-Narrow Angle Camera dayside sequence showed discontinuities in

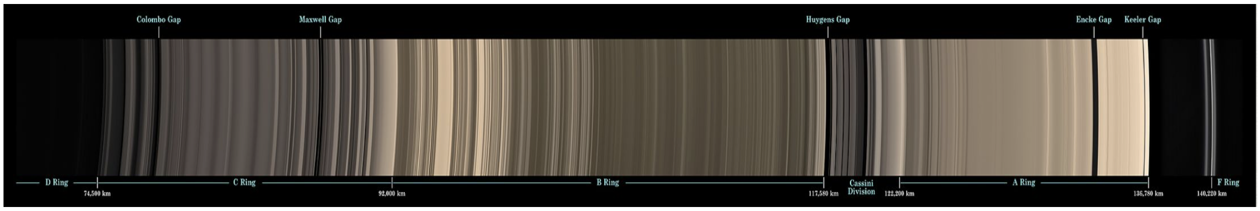

Figure 5.1: Saturn ring and its gaps. Mosaic in natural color of Cassini narrow-angle camera images of Saturn's D, C, B, A and F rings (left to right), taken on May 9, 2007. Source: NASA/JPL/Space Science Institute

Daphnis	
Mass [a]	7.793×10^{13} kg
Radius[a]	3.8 km
Density[a]	$0.34\mathrm{g/cm}^3$
Semi-major axis[b]	136505 km
Eccentricity[b]	3.31×10^{-5}
Inclination[b]	0.0036°

Table 5.1: Physical and orbital parameters of Daphnis. [a]Thomas (2010). [b]Jacobson et al. (2008)

the outer Keeler Gap edge, with 5 km long spikes. Owing to the similarities with Prometheus and the F ring, it was suggested that a small moon causes these structures inside the gap (Porco 2005). Confirmed later in a sequence of images taken on May 2005, S/2005 S1, a moon called Daphnis was found orbiting Saturn with a period of 0.594 days at a distance of 136500 km. Fig.5.2 shows an image from that sequence (Porco 2005).

Using about half a year of Cassini's observations, Spitale et al. (2006) determined Daphnis's orbit by fitting precessing Keplerian ellipses and found no apparent external perturbations. Some Daphnis physics parameters are shown in Table 5.1.

The gravitational influence allows Daphnis to work as a sculptor on the rings. Some structures are the waves on the Keeler Gap edge, result from perturbations from Daphnis on the A ring particles. Newest images from Cassini's Grand Finale show some material been pulled out from the ring edge and spreading as a result of Keplerian shear (Tiscareno et al. 2019).

5.2 Daphnis' orbit

Jacobson et al. (2008) revised the orbits of the small satellites of Saturn using data from Cassini, covering additional images taken up to March 2007. They numerically integrated the equations of motion for several small moons and considered the perturbation of the major Saturnian satellites. For Daphnis, as the same as for Pan, they assumed the orbit to be a

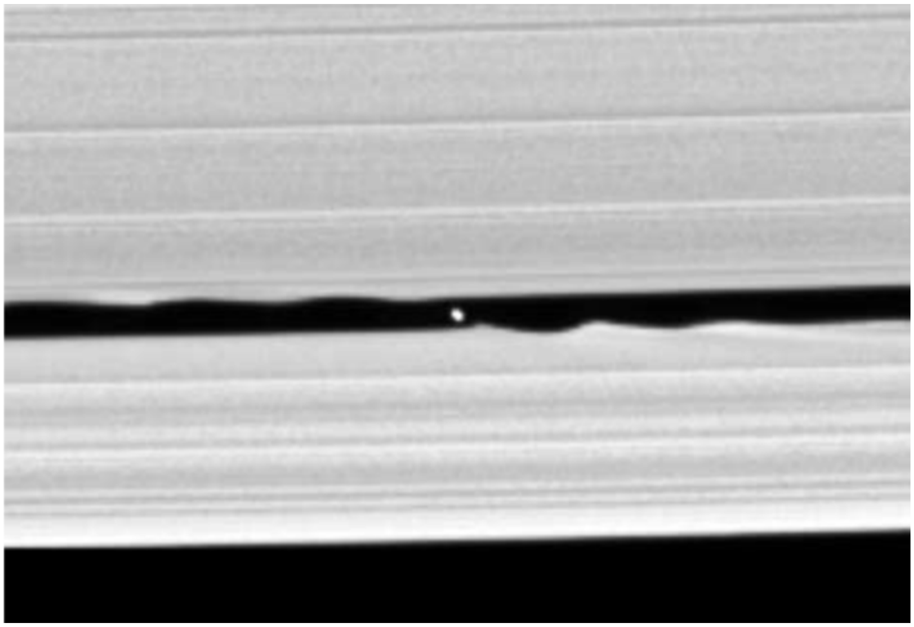

Figure 5.2: Daphnis (S/2005 S1) seen on 2005 May 5. Source: Cassini Imaging Team and NASA JPL SSI.

precessing ellipse only influenced by Saturn, since the planet seems to dominate those small satellites motion, and found out the eccentricity as 3.31×10^{-5} and inclination as $0.0036°$ for Daphnis.

Later, Jacobson (2014) reported that Daphnis changed its orbit. The orbital parameters that fit Cassini data from 2004 to 2010 do not fit the data from 2012 to 2014. It is relevant to mention that there is a lack of observations between those two periods. Spahn et al. (2018) also reported Daphnis orbit changes, and using two harmonics to model data through to 2015, the authors suggest that the satellite does an oscillatory motion.

During the final years of Cassini Mission, including the ring grazing orbits and the Grand Finale, the spacecraft was able to pass in the vicinity of the main rings and register them and other objects, like embedded moons, very close, and with high resolution (See Fig. 5.3).

The latest data from the Cassini Mission of Daphnis allows a new analysis of its orbit.

Figure 5.3: Daphnis seen during Cassini's Grand Finale. The Daphnis passage provokes some material to been pulled out from the ring edge and spreading as a result of Keplerian shear. Source: Tiscareno et al. (2019)

Therefore, this work is organized as follows. In the Chapter 6, we present the astrometry of Daphnis using images taken by Cassini from 2004 to 2017. Chapter 7 presents the Fast Lyapunov Indicator that we use to check the possibility of Daphnis being in a chaotic orbit and we present a numerical simulation that takes into account four other satellites of Saturn: Atlas, Prometheus, Pandora, and Mimas, in order to investigate the relevance of each moon on the understanding of Daphnis' motion. Lastly we present the final comments.

Chapter 6

Astrometry of Daphnis

Astrometry is an essential tool for orbital studies. It involves precise measurements of the positions and movements of celestial bodies.

In this chapter, we perform the astrometry of Daphnis using the CAVIAR software in a select set of images from the ISS-NAC camera until 2014. This analysis was made by the author during a COSPAR Capacity Buiding Workshop in 2015 under the supervision of Dr. Radwan Tajeddine and in collaboration with Dr. Bruno Morgado and Annabella Mondino. Later, the full astrometry of Daphnis orbit using Cassini data made by Dr. Tajeddine is mentioned here as part of ongoing collaboration work.

6.1 The images

6.1.1 Imaging Science Subsystem

The Optical Remote Sensing of Cassini spacecraft was developed to study Saturn, its rings and moons in the electromagnetic spectrum. It was composed of four instruments: *Composite Infrared Spectrometer* (CIRS), *Imaging Science Subsystem* (ISS), *Ultraviolet Imaging Spectrograph* (UVIS) and *Visible and Infrared Mapping Spectrometer* (VIMS).

The *Imaging Science Subsystem* consisted of a wide-angle camera (WAC) and a narrow-angle camera (NAC). The cameras were sensitive to visible wavelengths and some infrared and ultraviolet wavelengths. They also had multiple filters mounted on wheels allowing to select in each image the wavelengths to be sampled (Fig. 6.1).

The wide-angle camera was built with lenses, and it was projected to provide context. It was used to the navigation and to take images of the Saturn and rings in its fullness, broad scenes, and rings from more than one and a half million kilometers of distance.

The narrow-angle camera, built with mirrors, was projected to offer higher resolution, and it was used to take images of fractures or craters on Saturn's moons surfaces.

At the heart of each camera, there was a Charged-Coupled Device (CCD) detector that converted light into a digital image consisting of a 1024 square array of pixels, each 12 microns on a side[1].

[1]https://solarsystem.nasa.gov

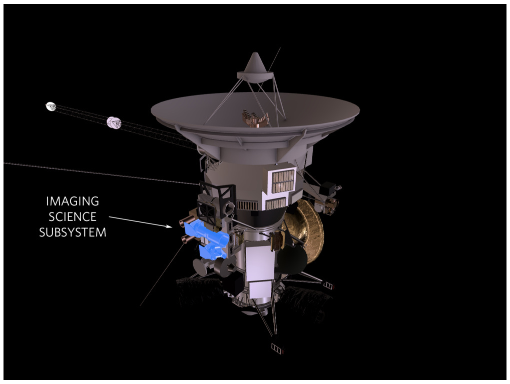

Figure 6.1: The Imaging Science Subsystem of Cassini Spacecraft (ISS) (left), and The Imaging Science Subsystem Narrow Camera (ISS NAC) (right); The ISS consisted of a wide-angle and a narrow-angle digital camera. The narrow-angle camera provided high resolution images of, among other, the surfaces of Saturn's moons.

The data used in this work was obtained by the *Narrow Angle Camera* ISS-NAC and was acquired using the OPUS[2] system.

6.1.2 Using OPUS

The Ring-Moon Systems Node is an online repository maintained by the SETI Institute, devoted to archiving, cataloging, and distributing scientific data sets relevant to planetary rings and moons. It is part of The Planetary Data System (PDS) archive, maintained by NASA, that contains digital data products returned from NASA's planetary missions, flight and ground-based data acquisitions, including laboratory experiments.

The Outer Planets Unified Search (OPUS) is a project of the PDS Ring-Moon Systems Node that allows the users to search for data of the systems of Jupiter, Saturn, Uranus, Neptune, and Pluto from missions such as Cassini, New Horizons, Voyager, Galileo, HST, and others. It allows search options as surface geometry for moons, planets and rings, lighting geometry, resolution, among other parameters.

The images used in this work can be select through the following steps from OPUS: the planet Saturn - Cassini Spacecraft - the small body Daphnis - the instrument ISS-NAC - observational resolution higher than 15 km.

A total of 109 images was found. They are distributed in two time intervals, the first between 2007-2010 and the other 2012-2014. These intervals are due to the equatorial orbit of Cassini when it can not observe Daphnis in the geometry as we need. This set of images has a resolution from 2 to 15 kilometers per pixel and solar phase angle from 15 to 125 degrees. An example of how Daphnis has to appear on a useful image is shown in Fig. 6.2. It is possible to see Daphnis in the Keller Gap.

[2]https://tools.pds-rings.seti.org

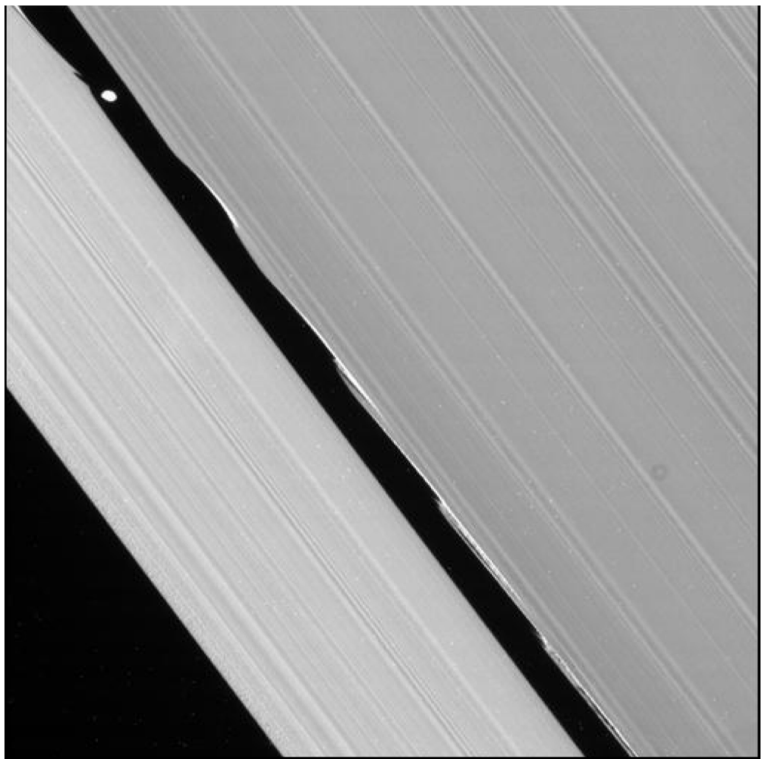

Figure 6.2: Example of a select image of Daphnis obtained from OPUS. To an image be useful to perform the astrometry it is necessary Daphnis appears on the image, enough sky area and some catalogued stars.

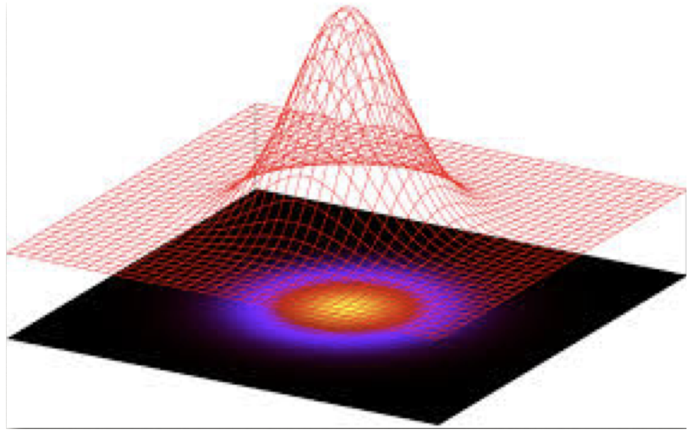

Figure 6.3: Example of a gaussian model to determine the centroid of the image.

6.1.3 Using SPICE

The next step is to find the Daphnis' position on the images. First, we need to convert between the ICRS reference frame (J2000) to the camera frame.

To do that, we use NASA's observation geometry system for space science missions *SPICE* (Spacecraft Planet Instrument C-matrix Events). It computes many kinds of observational geometry parameters at selected times as positions, velocities, size, shape, and orientation of planets, satellites, comets, asteroids. It also computes positions, velocities, and orientation of a spacecraft and its various moving structures, based on the spacecraft ephemeris.

We follow the next steps on SPICE to determine Daphnis position:

- Calculate the image time;
- Calculate the position of Cassini and Daphnis in the J2000 reference frame;
- Calculate the rotational matrix between J2000 frame and the camera frame;
- Determine the Daphnis' position in the camera frame.

This process results in the Daphnis ephemeris position in kilometers. After that, we convert the position of Daphnis from kilometers to pixels using the angular resolution of 0.35 degrees per 1024 pixels. Calculating the product between the angular resolution and the distance results in Daphnis' position in pixels.

6.1.4 Centroid position

Next, we need to determine the centroid of Daphnis on the image. A tool of the IDL Astronomy User's Library from NASA GCNTRD is used to fit a gaussian model to the brightness of the satellite in the image (See Fig. 6.3).

As the photo-center of the satellite is not the same as its center of mass, we must correct it before comparing Daphnis ephemeris. That happens because the observer is not in the same direction as the light source, so it will be looking only part of the object that is reflecting

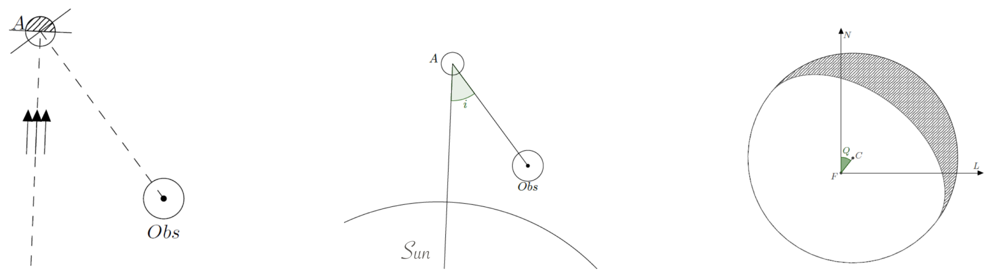

Figure 6.4: Photo-center, solar phase angle and subsolar point angle. Source: Morgado (2019)

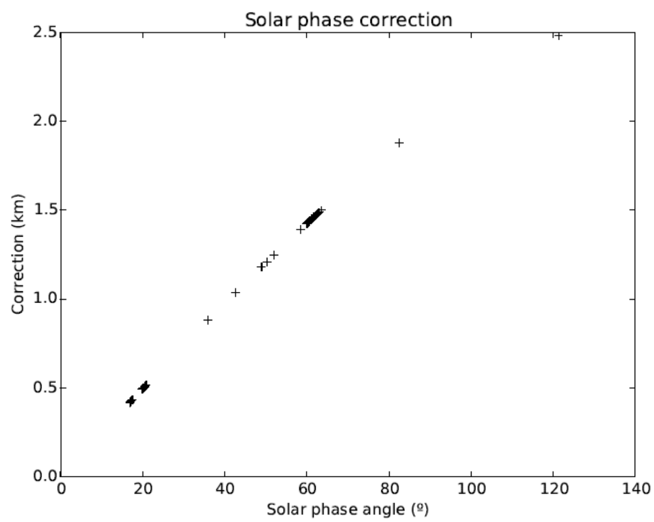

Figure 6.5: Correction of centroid on Daphnis images as function of the solar phase angle. The correction can reach up to 2 km for the set of images.

light. The angle between the light source and the observer is the solar phase angle, while the angle between the photo-center and the real center of the body is called the subsolar point angle, as shown in Fig. 6.4.

We can calculate the position of the center of Daphnis using

$$\begin{cases} x_f = C(i) r \sin i/2 \sin Q \\ y_f = C(i) r \sin i/2 \cos Q \end{cases}, \tag{6.1}$$

where x_f and y_f are the positions of the centroid, i is solar phase angle, and Q is the subsolar point angle. $C(i)$ is a coefficient from the law of reflection and r is the apparent radius of the object (Kaasalainen & Tanga 2004). On these images, the correction may mean more than 2 kilometers on the position, as shown in Fig 6.5.

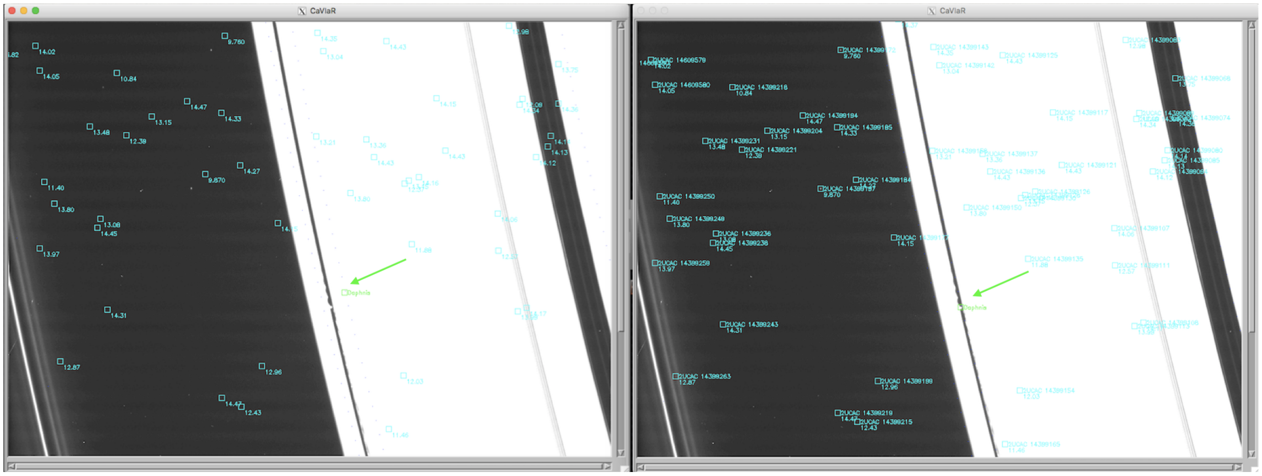

Figure 6.6: Two screen captures from CAVIAR. The left one is from before the correction, the small green square named Daphnis is at a wrong location, far from Daphnis actual position. On the right, after the correction, the green square is matching with Daphnis position on the image.

6.2 Astrometry with CAVIAR

We use a modified version of the CAVIAR software package for the astrometric reduction of Cassini ISS images (Cooper et al. 2018) as the last step to obtain Daphnis position in the ICRS. Also, this software converts the pixel position of a satellite in the image into a mean longitude assuming the satellite has zero inclination. This is a reasonable approximation to the present study, as will be seen in the next chapters.

On CAVIAR, the positions are estimated by fitting a model to the imaged limbs of the target satellites. Using the position of cataloged stars in the background, here we use the UCAC5 (Zacharias et al. 2017) and Tycho2 (Høg et al. 2000), to allow corrections to the nominal spacecraft pointing. In this work, we use UCAC5, which is currently preferred because of the availability of proper motion information.

For each image, we correct the pattern of positions from CAVIAR to match with the bodies on the image, using the stars as a guide to move it. This task can make a reasonable number of images inappropriate to use because Daphnis is inside the Keeler Gap at A ring, so it may be hard to have enough sky visible on the image, implying a smaller number of detectable stars to use.

Fig. 6.6 shown two screen captures from CAVIAR. The left one is from before the correction be made, the small green square named Daphnis is at a wrong location, far from Daphnis' actual position. On the right, after the correction, the green square is matching with Daphnis' position on the image.

The Fig. 6.7 shows the offset in x and y coordinates given in kilometers over the years, from 2006.5 to 2010. The blue dots are the positions for Daphnis before the pointing correction with CAVIAR, while the red dots are the same data after the correction. By analyzing the plot, it is clear that the pointing correction of the camera is indispensable. It improved the

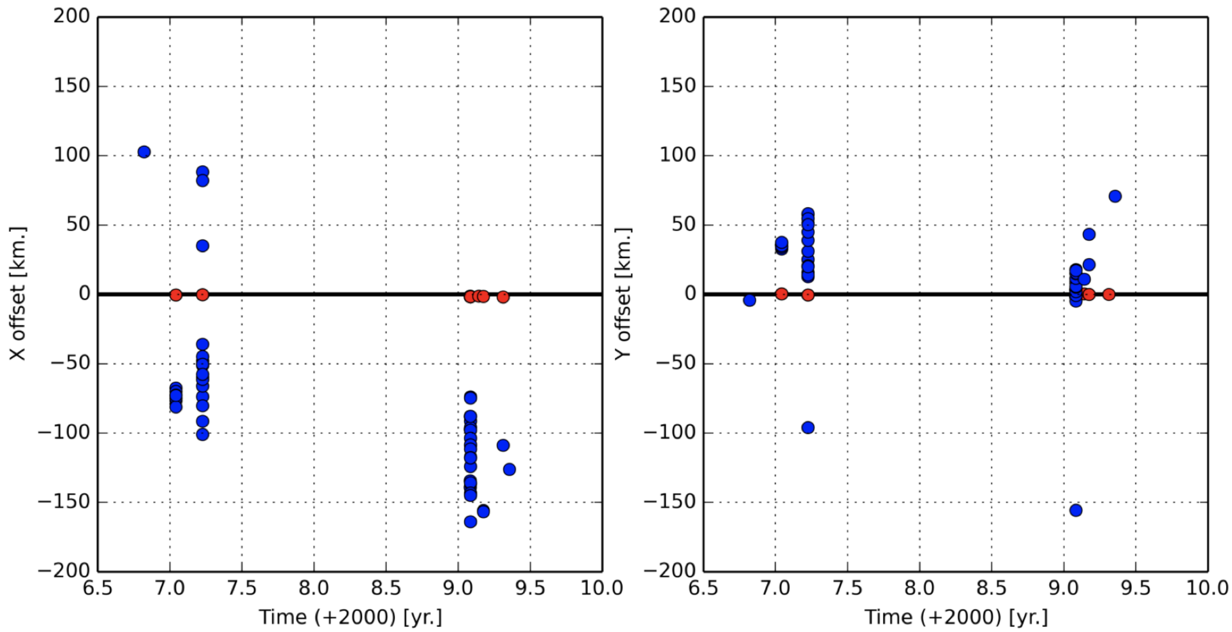

Figure 6.7: Offset of Daphnis position coordinates with and without pointing correction.

result by more the 150 kilometers in some epochs.

6.3 Results

The result using a total of 54 images is shown in Fig. 6.8. The first set of images, from 2006.5 to 2010, is well resolved, since the differences between the calculated and real position of Daphnis are near to zero, with an average precision of 1.5 km. However, after the interval of missing data between 2010 and 2012, due to Cassini switching to equatorial orbit, there is an increasing difference between the expected and the real positions.

The dispersion of the points is related to the Gaussian fitting, and this does not imply any constraints on Daphnis orbit. In other hand, the growing trend on these data corresponds a change on Daphnis mean motion that we can calculate using

$$\Delta\alpha = \frac{\text{offset}}{a_{Daphnis}} = \Delta n \cdot t + c, \tag{6.2}$$

where $\Delta\alpha$ is X and then

$$\Delta n = -5.52 \times 10^{-3} \text{ rad/yr.} \tag{6.3}$$

Astrometry comprehending the full Cassini mission period for Daphnis was made using

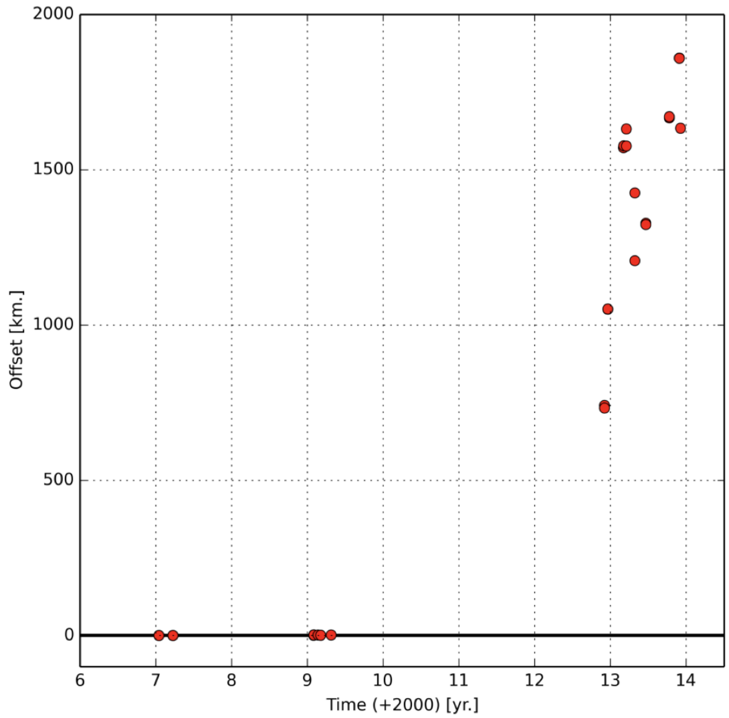

Figure 6.8: Result of the astrometry of Daphnis position using 54 Cassini images from 2006 to 2014. Offset in kilometers per time in years after 2000. The first period of images fit does not match the second period of images.

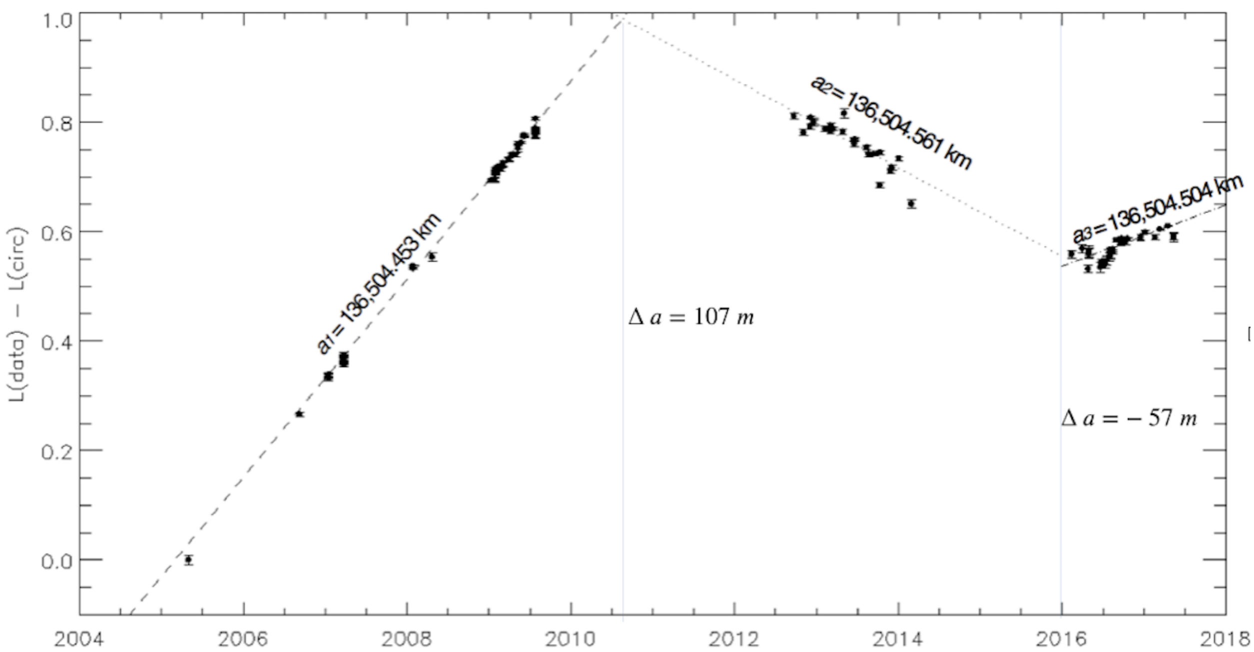

Figure 6.9: Daphnis' residual longitude relative to a circular orbit at 136,504.5 km, by Radwan Tajeddine (private communication) Missing data between 2010 and 2012, then between 2015 and 2016 are due to Cassini switching to equatorial orbits.

129 images from 2005 to late 2017, by Radwan Tajeddine (private communication). For each position of Daphnis, the authors calculated the residual longitude relative to an assumed circular orbit at the radius of $136,504.5$ km. It reveals, beyond the change shown in Fig. 6.8, a second change on Daphnis' semi-major axis.

Fig. 6.9 shown the first increase on the residual longitude of ∼107 meters around late 2010 and later a decrease of ∼57 meters around early 2016 (an interval about 5.5 years). Missing data between 2010 and 2012, and between 2015 and 2016, are due to Cassini switching to equatorial orbits.

Those results mean that only one semi-major axis Daphnis cannot match all the years of the Cassini mission, but it changed through three different orbits.

The Daphnis orbital changes were reported by R.A. Jacobson (private communication) and Spahn et al. (2018). The later, using two harmonics to model data through to 2015, suggested that the satellite does an oscillatory motion, with a 15-year period. However, data after 2016 pointed out this is not a periodic event.

Therefore, Daphnis has been unpredictably changing orbit, raising the possibility of the moon to be into an unstable region. This possibility will be explored in the next chapter.

Chapter 7

Numerical Simulations

7.1 Study of Stability

In this section, to investigate if Daphnis is orbiting in a stable region, we perform a numerical simulation of the system and analyze the Fast Lyapunov Indicator for its orbit.

This study has been developed in collaboration with Dr. Maryame El Moutamid, that started during a short visit at Cornell University.

Fast Lyapunov Indicator

Using an implementation of the RADAU 15th order algorithm (Everhart 1985), we consider Saturn plus five satellites: Daphnis, Atlas, Prometheus, Pandora, and Mimas. The latter two satellites were included because they are the strong perturbers of Prometheus.

The initial orbital elements of the satellites are taken from Jacobson et al. (2008), except for Mimas that is taken from Horizons website for the same epoch (Giorgini et al. 1996). We have considered the physical parameters of Saturn given in Table 7.1 and initial masses for the satellites from Tables 7.2.

To measure the stability of the Daphnis' semimajor axis, we use the Fast Lyapunov Indicator method, hereafter FLI (Froeschlé et al. 1997, Froeschlé & Lega 2000). To compute the evolution of the FLI over time, simultaneously with the full equations of motion is started the integration of the variational equations. A similar use of this tool can be found in Cooper et al. (2015).

Saturn	
Mass	379.312×10^{5}
Radius	60330.0
J_2	16299×10^{-6}
J_4	-916×10^{-6}
J_6	81×10^{-6}

Table 7.1: Saturn parameters used on the numerical simulations: mass, radius and the zonal harmonic coefficients. The mass is given in km^3/sec^2 and the radius in kilometers. Jacobson et al. (2006)

Satellites masses	
Mimas	3.751×10^{19}
Daphnis[a]	7.793×10^{13}
Prometheus	1.594×10^{17}
Pandora	1.370×10^{17}
Atlas[a]	6.593×10^{15}

Table 7.2: Masses of Daphnis, Prometheus, Pandora, Mimas and Atlas are given in kg and are from Horizons (Giorgini et al. 1996) except ([a]) there are from Thomas (2010).

The Fast Lyapunov Indicator is a useful tool based on the Lyapunov characteristic exponent theory, a well known and used method to estimate the chaoticity on dynamical systems. Considering neighboring trajectories in phase space, these exponents measure the rate of the divergence among them.

For a given autonomous dynamical system $\dot{\mathbf{x}} = \mathbf{f}(\mathbf{x})$, the maximum Lyapunov characteristic exponent (hereafter MLCE) is defined by

$$\mathrm{MLCE} = \lim_{t\to\infty} \frac{1}{t} \ln\|\mathbf{w}(t)\|, \tag{7.1}$$

where $\mathbf{w}$ is the deviation/tangent vector solution of the variational equations of the system.

The FLI is also based on the computation of the norm of the tangent vector $\mathbf{w}$, and is defined as the initial part, up to a stopping time t_f, of the computation of the MLCE:

$$\mathrm{FLI} = \sup_{0<t<t_f} \ln\|\mathbf{w}(t)\|. \tag{7.2}$$

This allows FLI to be faster than MLCE to discriminate chaotic orbits from regular orbits. If the initial condition used on a simulation presents a FLI growing linearly in time, that means this initial condition is from a chaotic region, in other words, that this orbit is chaotic. Whereas to an initial condition taken from a stable region, in other words, of a stable orbit, the FLI will present a logarithmic growth on time.

The Daphnis orbit was numerically integrated for a timespan of 500 years and the FLI evolution in time are presented in Fig.7.1.

The blue line indicates the FLI evolution of an orbit starting on the nominal semi-major axis of Daphnis of $a = 136505.5$ km, that showed to be chaotic, once their FLI are increasing nearly linear. Otherwise, in the case of a different orbit, with a semi-major axis of $a = 136600.5$ km, the FLI is slowly growing in a logarithmic behave, indicating that it consists in a regular orbit, as shown the dashed green line.

From the FLI measurement, we can extract the Lyapunov time, which is obtained by computing the inverse of the FLI slop. The Lyapunov time represents the time needed for nearby orbits to diverge exponentially. The FLI in Fig. 7.1 indicates that Daphnis is on a chaotic orbit with a Lyapunov time around 22 years, which consists of a short Lyapunov time, implying that Daphnis is into a highly chaotic region.

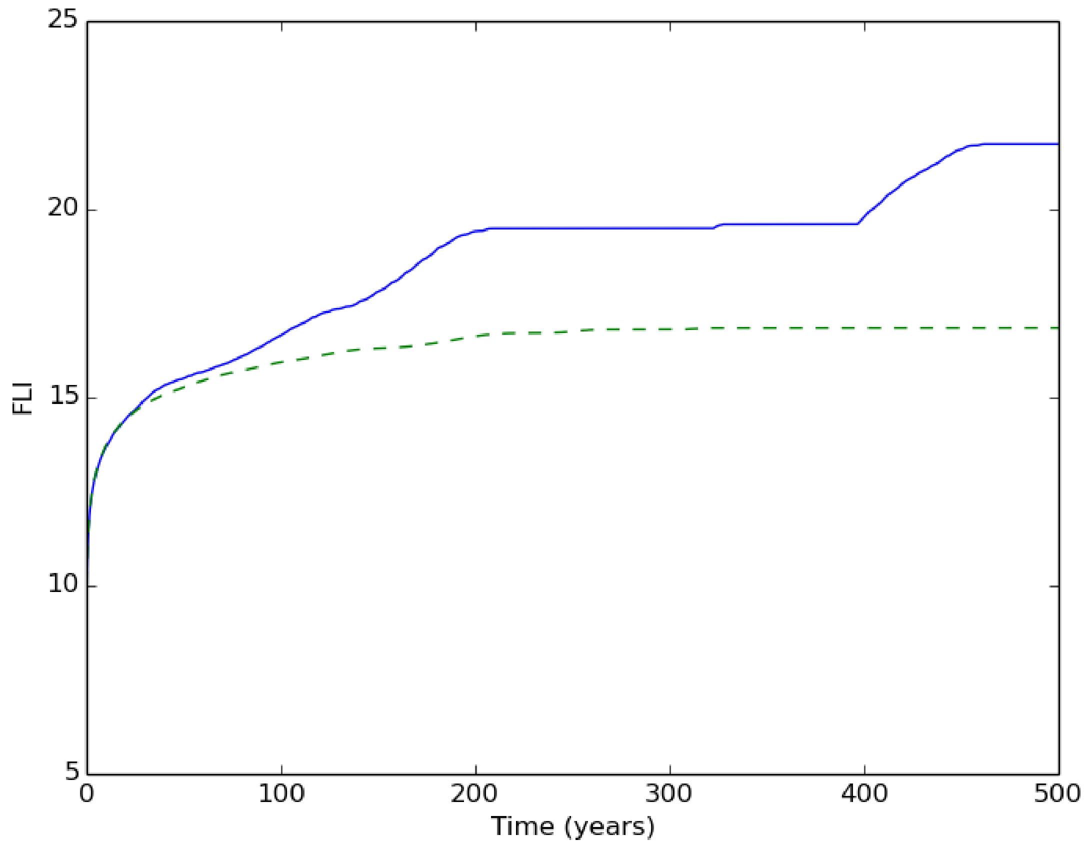

Figure 7.1: FLI vs. time for Daphnis, using the physical parameters from Tables 7.1 and 7.2. Obtained from a model consisting of Saturn, Atlas, Prometheus, Pandora, Mimas, and Daphnis. The upper solid blue curve represent a chaotic orbit obtained using the nominal semi-major axis of Daphnis of $a = 136505.5$ km. In order to compare with a non-chaotic orbit, the lower dashed green curve shows a regular orbit behavior obtained using a semi-major axis 0.07% away from Daphnis.

Nearby Resonances		
Satellite	Res	Order
Prometheus	129:125	4
Atlas	157:155	2
Atlas	236:233	3
Atlas	314:310	4
Atlas	315:311	4

Table 7.3: Nearby resonances to Daphnis with Prometheus and Atlas, with their respective orders and their distance from Daphnis position. We selected the resonances up to fourth order and closer than 2.5 kilometers from Daphnis' semimajor axis.

7.2 Resonances

As seen in Chapter 2, in the work by Goldreich & Rappaport (2003a), the authors identified that Saturn's small moons Prometheus and Pandora are in chaotic orbits. Later, Goldreich & Rappaport (2003b) identified a mean motion resonance split into four arguments that are overlapping, which was associated with the moons' chaotic behavior. This result was previously identified by Renner & Sicardy (2003), and developed further studies by Cooper & Murray (2004) and Renner & Sicardy (2006) also confirmed this result.

Following this idea, once we verified that Daphnis is in a chaotic orbit, as shown in Section 7.1, we investigated the existence of some possible resonances between Daphnis and other moons that could be relevant for Daphnis' orbital motion.

Using the Mercury package (Chambers 1999, Bulirsch & Stoer 1980), we performed a full numerical simulation considering Saturn as a central body with its zonal gravitational harmonics up to J_6 plus Daphnis, Prometheus, Pandora, Atlas, and Mimas. This is the same setup we used to calculate the FLI indicator as shown in Section 7.1 and is shown on Table 7.1, Table 7.2 and Table **??**.

A routine that systematically searched for $(p : p-q)$ mean motion resonances considering q up to 4 (equivalent to a fourth-order resonance) was used to found resonances nearby to Daphnis that are more likely to have considerable interaction with it.

The five resonances selected are shown in Table 7.3. Among the seven resonances found, one is between Daphnis and Prometheus and six between Daphnis and Atlas, resulting in one second order, one third order and three fourth order.

A mean motion resonance can split into multiple resonant arguments, depending on its order. Considering a general form for the argument in the expansion of the disturbing function we have

$$\phi = j_1\lambda' + j_2\lambda + j_3\varpi' + j_4\varpi + j_5\Omega' + j_6\Omega, \tag{7.3}$$

where ($'$) indicates the orbital elements of the external body, and the coefficients must obey the D'Alembert relation

$$\sum_{i=1}^{6} j_i = 0. \tag{7.4}$$

Once we fixed j_1 and j_2, there will be an infinite number of combinations among j_3 to j_6 that satisfy the condition, but we are interested in those that the sum of the coefficients j_1 and j_2 in module is minimum (Murray & Dermott 1999).

The 129:125 resonance between Daphnis and Prometheus carries nineteen resonant arguments. The same number of resonant arguments is carried for the two fourth order resonances with Atlas. For the second and third orders with Atlas, there are six and ten arguments, respectively. Finally, for each fifty order, there are twenty resonant arguments. Hence, the seven resonances displayed on Table 7.3 represents a total of ninety-four possible resonant arguments.

For each resonant argument, we plotted the temporal evolution of the angle and looked for features that could indicate any relevance to the resonance.

From those numeral possibilities, we verified that some effects arise from specific resonant arguments of the 129:125 resonance with Prometheus and the 157:155 resonance with Atlas. Fig. 7.2 shows the time evolution of these resonant angles.

For the Prometheus case, the $129\lambda_P - 125\lambda_D - 4\Omega_P$ angle is librating during the interval of t $\sim$ [5.7, 8.7] yrs and again over t $\sim$ [12.7, 15.1] yrs. Each interval consists of approximately 1800 orbital periods of Daphnis.

The Atlas mean motion resonant angle $157\lambda_A - 155\lambda_D - 2\Omega_A$ is librating during the intervals of t $\sim$ [3.0, 4.7] yrs and t $\sim$ [6.7, 11.2] yrs, approximately 1000 and 2700 periods of Daphnis, respectively.

Such behavior of the Prometheus 129:125 and Atlas 157:155 mean motion resonant angles, alternating between libration and circulation over the years, indicate that both satellites and their related mean motion resonances contribute to Daphnis chaotic orbital motion.

So, we calculated the FLI for Daphnis orbit with the same initial conditions from Section 7.1, except we took Prometheus and Atlas out of the simulation at the same time. The result is shown in Fig. 7.3.

From Fig. 7.3, it is clear the Daphnis orbit turns into a stable orbit when we did not include Prometheus and Atlas on the numerical simulation. That reinforced that the satellites are somehow responsible for Daphnis orbital chaos.

Other measurements may be done before to define these resonances are the only reason why Daphnis orbit is chaotic, but the results are enough to show that Prometheus and Atlas and their mean motion resonances are playing a role in Daphnis chaotic behavior.

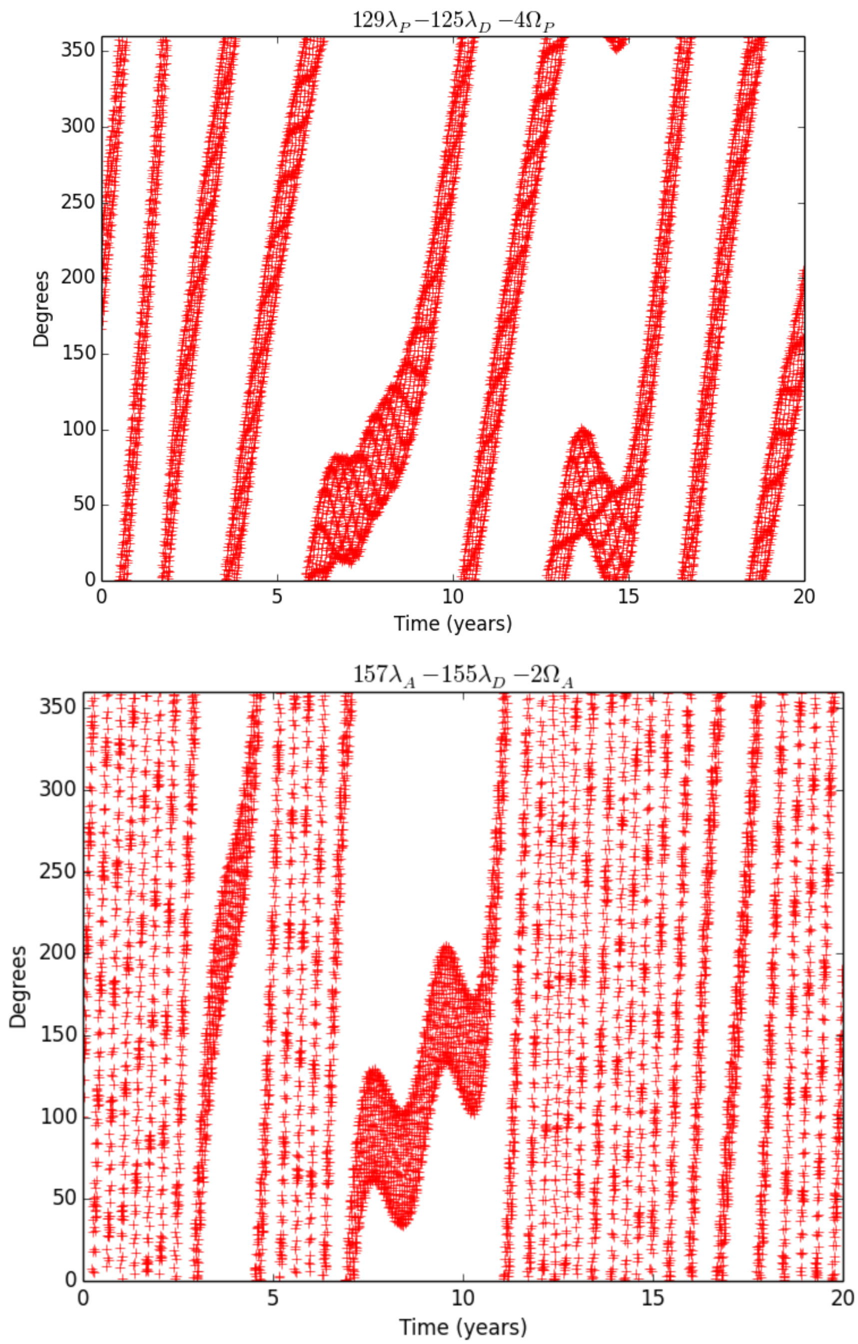

Figure 7.2: Temporal evolution of the resonant angles $129\lambda_P - 125\lambda_D - 4\Omega_P$ between Daphnis and Prometheus (top) and $157\lambda_A - 155\lambda_D - 2\Omega_A$ between Daphnis and Atlas (bottom).

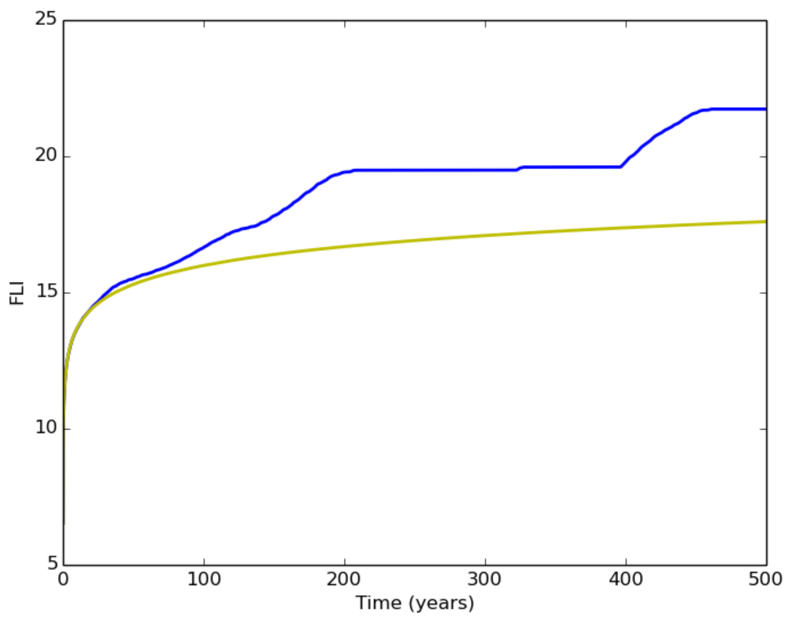

Figure 7.3: FLI vs Daphnis orbit. The blue line is from the simulation using the nominal semi-major axis value of Daphnis and considering Atlas, Prometheus, Pandora and Mimas from Section 7.1. The yellow line is from a simulation with the same initial condition except Prometheus and Atlas were not included.

7.3 Final Comments on Part II

In this part, we performed the astrometry of Daphnis using the CAVIAR software in a select set of images from the ISS-NAC camera of Cassini. The result indicated that Daphnis could not be resolved in one orbit during the years of the Cassini mission, but it changed through three different orbits, implying Daphnis has been changing orbit in an unpredictable way, raising the possibility of the moon to be into an unstable region.

So, we investigate if Daphnis is orbiting in a stable region, and for this, we implement numerical simulations using an implementation of RADAU 15th order algorithm (Everhart 1985), we consider Saturn plus five satellites: Daphnis, Atlas, Prometheus, Pandora, and Mimas.

By computing the evolution of the Fast Lyapunov Indicator FLI, it was showed that Daphnis orbit is chaotic with a Lyapunov time of $\sim$22 years. It consists of a short Lyapunov time, implying that Daphnis is into a highly chaotic region.

After that, we investigated the existence of some possible resonances between Daphnis and other moons that could be relevant for Daphnis' orbital motion and found that the Prometheus and Atlas and their mean motion resonances with Daphnis 129:125 and 157:155, respectively, are playing a role in Daphnis behavior. To conclude, we found that when Prometheus and Atlas are not included in the simulation, Daphnis' orbit became regular.

Part III

Charon, Styx, Nix, Kerberos and Hydra

Chapter 8

Introduction

The large number of objects in an extremely compact region makes the Pluto system a very intriguing environment with many open questions. One of the main questions without a satisfactory explanation is the system formation process and its evolution to the current configuration. Pluto's four small satellites Styx, Nix, Kerberos, and Hydra, were discovered close to, but not in, the 1:3, 1:4, 1:5, and 1:6 mean motion resonances with Charon, respectively (Cheng et al. 2014). Later, Styx, Nix, and Hydra were found to be in at least one three body resonance, a particular configuration not so common among satellites, and that provides clues to the origin of the system (Showalter & Hamilton 2015).

In the next chapters, we propose and seek evidence for a path to explain the satellite's current positions.

This work has been developed in a collaboration with Dr. Douglas P. Hamilton that started during a Ph.D. internship at the University of Maryland.

8.1 The Binary System

Discovered in 1930 by Clyde Tombaugh, Pluto was classified as the ninth planet of the Solar System. Pluto has a mass of 1.3030×10^{22} kg (Brozović et al. 2015), and it orbits the Sun at a distance of 5,906,440,628 km in an eccentric and highly-tilted orbit in the Kuiper Belt region. It has a thin atmosphere of nitrogen, methane, and carbon monoxide.

Pluto presents a rich geological composition. It has a heart-shaped glacier, Sputnik Planitia, that may have been formed by sublimation. Pluto also has mountains, craters and also some unusual feature that consists of at least six extensional fractures across Pluto's icy landscape. The longest one, called Sleipnir Fossa, is more than 580 kilometers long (Stern et al. 2015, 2018).

In 1978 Charon was discovered as the first satellite of Pluto by Christy & Harrington (1978). However, Charon mass is about 12% of Pluto's, and around half of its radius (Stern et al. 2015), so the two objects are comparable, and the center of mass of the system is located at a point outside of the two bodies (Fig. 8.1). In 1993, the first additional Kuiper Belt was discovered (Brown et al. 2005), and there are now many thousands known. In 2006, Pluto was reclassified as a dwarf-planet.

In the past, a collision of a minor body with a proto Pluto is the most likely pathway

Figure 8.1: Pluto and Charon - The binary System. Composite of enhanced color images of Pluto (right) and Charon (left), taken by NASA's New Horizons spacecraft on July 14, 2015. Source: NASA/JHUAPL/SwRI

for Charon's formation, and it is possible that such collision would not entirely destroy the original Charon (Canup 2005).

However, even before the reclassification of Pluto, the system showed to be much more complex than expected. Observations performed in 2005 by Weaver et al. (2006) with the Hubble Space Telescope (*HST*) revealed the existence of two more bodies in the system, Nix and Hydra.

Buie et al. (2006) presented the astrometry of Pluto and the three satellites known at that time, Charon, Nix, and Hydra. Using *HST* images from 2002 and 2003, they fitted orbits for all three and founded they are coplanar. Charon and Nix have eccentricities zero, and Hydra has a significant eccentricity of 0.0052. The orbital periods are 38.2065, 24.8562 and 6.3872304 days, for Hydra, Nix, and Charon, respectively.

Five years later, new satellites were also discovered with Hubble Space Telescope images: Kerberos and Styx, in 2011 and 2012, respectively (Showalter et al. 2011, 2012).

The satellites' orbits were reported to be coplanar and circular (Brozović et al. 2015, Showalter & Hamilton 2015), which indicated that the most likely theory for their origin is the same impact on Pluto that formed Charon. Some authors tried to reproduce this process including Ward & Canup (2006), Lithwick & Wu (2008), Kenyon & Bromley (2014) and Walsh & Levison (2015) but none of them has been fully successful.

Among other formation theories for the satellites is the one studied by dos Santos et al.

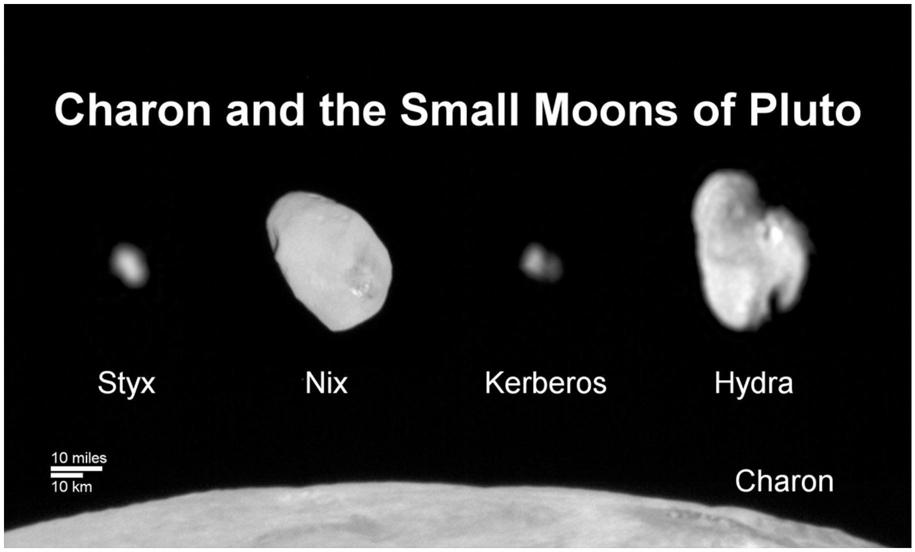

Figure 8.2: Family Portrait of Pluto's Moons: Charon, and all four of Pluto's small moons, Nix, Hydra, Kerberos and Styx resolved by the Long Range Reconnaissance Imager (LORRI) on the New Horizons spacecraft. Source: NASA/JHUAPL/SwRI

(2012), which was suggested by Lithwick & Wu (2008). It consists of a collisional capture scenario where a planetesimal temporarily captured by Pluto-Charon would collide with another planetesimal and would form a disk of debris that collided among themselves, damping the orbital eccentricities and inclinations, resulting in a coplanar disk from where the satellites would be formed near their current positions. However, dos Santos et al. (2012) found that the timescale for the captured object and the collider object are incompatible. While the temporally capture of the bodies with enough mass to produce Nix and Hydra is happen fast, it takes to long for other bodies to collide with it.

Showalter et al. (2013) reported preliminary orbital elements for Kerberos and Styx, and also stated that they are near to, but not in, the 1:3 and 1:5 mean motion resonances with Charon. Additionally, Nix and Hydra are also near to the 1:4 and 1:6 resonances. These near resonant relationships make the system dynamically rich and exciting to be studied (Fig.8.2).

Woo & Lee (2018) performed N-body simulations with the small satellites considered as test particles and Pluto–Charon evolving by tidal forces to validate the scenario that suggests the small moons were formed close to their current locations resulted from a disk of debris product from the Charon-forming impact before its tidal evolution. The survivors' particles with final eccentricities matching the current moons do not present any preference to be in or near the 4:1, 5:1, and 6:1 resonances with Charon. Therefore, an alternative scenario may be needed to explain the unique current configuration of Pluto's small satellites.

8.2 New Horizons

To know more about the system, in January 2006, the spacecraft New Horizons was launched toward Pluto. It was the first mission with destination to the Pluto system and the Kuiper Belt. After a nine year journey, the spacecraft spent six months getting data from Pluto, Charon, and their satellites, with a close approach with the dwarf planet on July 14th, 2015. The mission main goal was to characterize Pluto and its satellites' geology and morphology.

On January 1st, 2019, as the second mission goal, the spacecraft made a flyby with the Kuiper Belt local object 2014 MU69, also called Ultima Thule. It was the farthest exploration of an object in history.

The New Horizons spacecraft carried a considerable set of scientific instruments: a visible and infrared spectrometer Ralph, an ultraviolet imaging spectrometer (Alice), a telescopic camera (LORRI), the Radio Science EXperiment (REX), a solar wind and plasma spectrometer (SWAP), an energetic particle spectrometer for plasma (PEPSSI) and an instrument built by students to measure space dust (VBSDC).

The initial results from the New Horizons observations, presented by Stern et al. (2015), show a complex variety on Pluto's surface, with different geological forms, structures resulted from impacts, tectonic activities, cryovolcanic and mass loss processes. This suggests a dynamic history of the dwarf planet.

Weaver et al. (2016), also using New Horizons data, derived the elongated satellite shapes and identified craters at least 4 billion years old on the surfaces of Nix and Hydra. The authors also suggested that the surfaces of the satellites are composed of water ice, what could explain their high albedos. Furthermore, it was verified that the four satellites rotate much faster than the corresponding synchronous periods and have poles with unusual orientations (almost orthogonal to the expected positions). These results reinforce the hypothesis that the satellites are the outcome of the collision that originated Pluto and Charon, and indicate the complexity of dynamical mechanisms involving the Pluto system.

8.3 Resonances among the moons

Before the New Horizons made its way to Pluto, Cheng et al. (2014) performed numerical simulations of tested particles to analyze the effects of the mean motion commensurabilities 3:1, 4:1, 5:1, 6:1 between Charon and each one of the four small satellites Styx, Nix, Kerberos, and Hydra respectively, earlier reported by Showalter et al. (2013). They investigated the satellites migration from a more compact configuration to their current positions. These commensurabilities would cause the satellites to migrate together with Charon, once it experiences the tidal force due to Pluto. The authors concluded that transport due to resonances would be quite unlikely because of the instability of the system.

In the following year, by the observational data obtained in preparation for the New Horizons arrival, Showalter & Hamilton (2015) analyzed in detail the satellites orbits and found that Styx, Nix, and Hydra could be in a three body resonance, similar to the Laplace resonance of Jupiter satellites Io, Europa, and Ganymede. Besides, based on Hubble Space Telescope data, the authors suggested that the rotation of Nix and Hydra is chaotic, although later analysis of New Horizons data indicates that this is not the case (Showalter, private communication).

Chapter 9

Capture into multiple resonances

9.1 Using forced resonance migration

An impact between Charon and Pluto that ended in the capture of Charon is a likely scenario proposed by Canup (2005) for the formation of the binary system. The impact is assumed to have happened in the distant past when the Kuiper belt population had more members than nowadays. The Charon orbit after the impact would be eccentric and with a semimajor axis around four times the Pluto radius. The tidal evolution would take the two bodies into the double synchronous state, with equal orbital and spin frequencies, ending up in a circular orbit.

Ward & Canup (2006) proposed that the small satellites were formed from debris produced by the giant impact that originated Charon. Thus, the satellites would have been formed close to Pluto and Charon so, once Charon starts moving out due to tidal evolution, the small satellites might have been captured into corotation resonances, that allowed them to also move outwards with Charon. Because corotation resonances do not cause eccentricity growth, this should be a stable migration. As Charon migrates, its orbital eccentricity starts to damp to zero, allowing the small satellites to escape from the resonances.

Some authors tried to reproduce the resonance migration. Lithwick & Wu (2008) found that it is possible to migrate Nix or Hydra along with Charon. In this scenario, Charon's eccentricity must be smaller than 0.024, otherwise the Lindblad and corotation resonances 4:1 would overlap, originating chaos. At this point, the migration would be faster than libration, making Hydra exit the resonance.

Walsh & Levison (2015) explored collisional interactions among debris orbiting the Pluto-Charon system. They found this mechanism can move some material outwards; meanwhile, it also retains some material unstably bounded to the Pluto-Charon system. This debris did not show preference to originate satellites in or near mean motion resonances with Charon.

Zhang & Hamilton (2007) investigating the two Neptune's satellites Proteus and Larissa argued that during past tidal migration, those satellites passed through a 2:1 mean motion resonance that resulted in their excited eccentricities and inclinations. Thus, the authors identified a new type of three-body resonance between small satellites that involved the pair of small moons and Triton that surprisingly proved stronger than the two-body resonances between the pair.

In a next work Zhang & Hamilton (2008) extended their study adding the satellites

Galatea and Despina to test the hypothesis that those moons were formed with zero inclinations that later were excited by mean motion resonances. They found that Proteus, Galatea, and Despina inclinations are consistent with this hypothesis. However, Larissa's inclination seems to be too large.

These works imply that future models to explain capture into mean motion resonances during tidal migration must account for non-zero eccentricities and inclinations of the small satellites. They also suggest that resonances no longer active may have excited the system in the past.

As we have seen before, all the small moons of the Pluto-Charon system are close to a mean motion resonance with Charon. Styx is close to 2:1, Nix is close to 3:1, Kerberos to the 4:1, and Hydra is close to the 5:1 (Buie et al. 2013). Moreover, Styx, Nix, and Hydra seem to be in a three-body resonance 3:5:2, while Styx, Nix, and Kerberos also seem to be at 42:85:43 according to Showalter & Hamilton (2015).

Gallardo et al. (2016) using a semianalytical method, computed the strengths on each massive body in a three-body mean motion resonance. They explored the dependence among the strength and the masses, the orbital parameters, and the resonance order.

The authors confirmed that lower order resonances of eccentricity and inclinations are stronger. However, higher order resonances turned out to also be relevant when it comes to three-body mean motion resonances.

Another significant result reported by Gallardo et al. (2016) is the higher probability to trap a satellite system into a three-body resonance through capture in a chain of two-body resonances.

Inspired by these results, we want to find scenarios for the origin of the current configuration of the Pluto satellites, considering the growth of the satellites' orbital eccentricity as a key for the resonance captures and migration to carry them on the three-body resonance.

So, in this work, we hypothesize a series of events, essentially multiple captures into two-body mean resonance motion among Pluto's satellites, to be able to reproduce a three-body resonance capture.

Unlike previous works that have investigated the forced migration resonance by tidal forces without considering excited eccentricities and inclinations for the small satellites, we will be considering it in our model inspired by Zhang & Hamilton (2007, 2008).

Of the two resonances pointed out by Showalter & Hamilton (2015), we have chosen to focus on the $3\lambda_S - 5\lambda_N + 2\lambda_H$ resonance among Styx, Nix, and Hydra due the more robust of the two possible resonances.

The representation of the proposed chain of events that may result in the capture can be seen in Fig. 9.1, described as follows. We start considering the system back in the past, when Charon is migrating outwards from Pluto by tidal forces as proposed by Canup (2005) *(a)*. Then we expect a first resonance capture to happen with one of the small moons into a two-body resonance with Charon. The first small moon will start moving outward while simultaneously, it has its eccentricity raised by the resonance *(b)*. Afterward, a second capture should happen with another small moon into a two-body resonance, but this time between it and the migrating small moon *(c)*. The eccentricity of the second small moon will start to increase, allowing an additional capture with a third small moon. At this point, the three-body resonance must be activated instantly *(d)*. At the end, when the three-body resonance takes control, the small satellites captured, in principle, may be adiabatically removed from

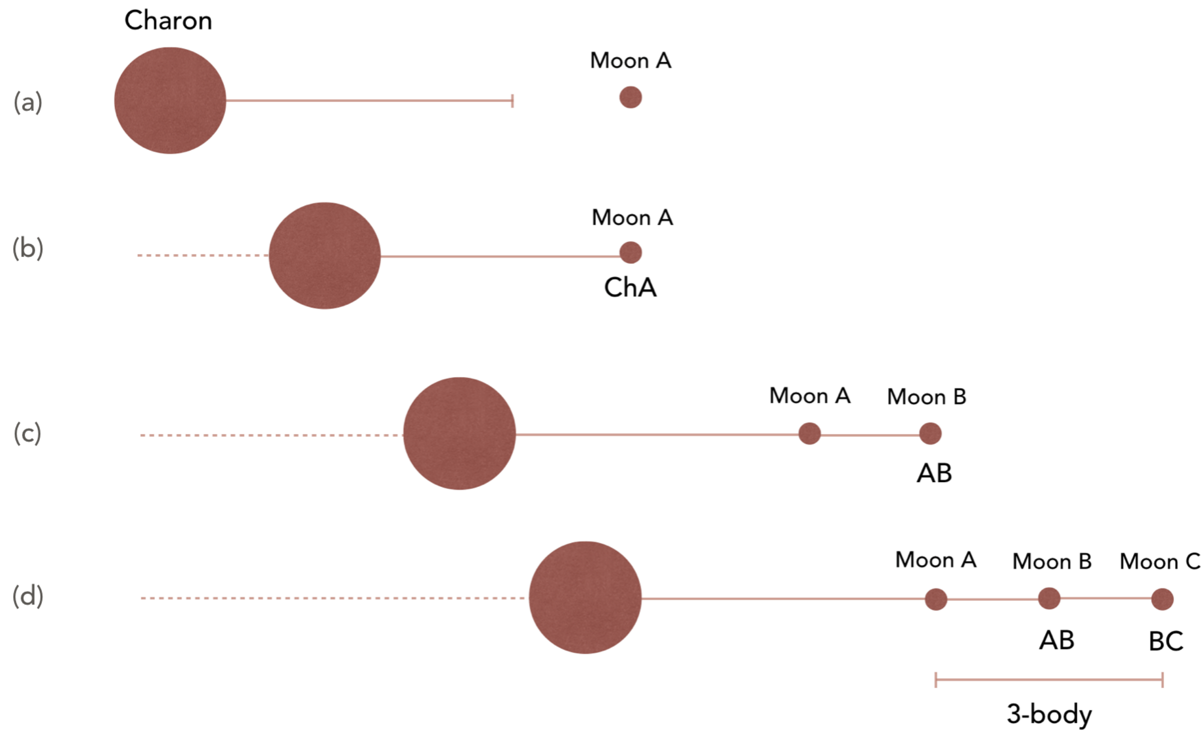

Figure 9.1: Tidal migration scenario. (a) Charon starts moving outwards by tidal force. (b) Charon captures Moon A [ChA]. (c) Moon A captures Moon B [AB]. (d) Moon A or Moon B captures Moon C [BC] and Three-body resonance among the small moons takes over.

its resonance with Charon and have their eccentricities driven back to zero.

An example of this dynamical path is the Laplace resonance at Jupiter. In that system, the satellite Io captures Europa into the 2:1 mean motion resonance, Europa captures Ganymede into another 2:1 mean motion resonance and then the three-body resonance 1:3:2 is activated.

9.2 Looking for special resonances

Mathematically, to the scenario presented in Fig. 9.1 be possible, it requires a pair of resonances in a specific format where the arguments must have equal terms in the pericenter. Such a particular configuration among the resonant arguments will allow the addition of each other to result in the expected resonant argument, as we show in this section.

There are infinite possibilities for this pair of resonant arguments. The low order resonances are usually stronger and, consequently, more probable to happen. Therefore, we search only for first order resonances as

$$\psi_1 = A\lambda_a - (A-1)\lambda_b - \varpi_b \tag{9.1}$$

Resonant angle pair
$\psi_1 = 2\lambda_H - \lambda_S - \varpi_S$
$\psi_2 = 5\lambda_N - 4\lambda_S - \varpi_S$
$\psi_1 = 6\lambda_H - 5\lambda_N - \varpi_H$
$\psi_2 = 4\lambda_H - 3\lambda_S - \varpi_H$
$\psi_1 = 2\lambda_H - \lambda_N - \varpi_N$
$\psi_2 = 4\lambda_N - 3\lambda_S - \varpi_N$
$\psi_1 = 7\lambda_N - 6\lambda_S - \varpi_N$
$\psi_2 = 4\lambda_H - 3\lambda_N - \varpi_N$

Table 9.1: Some pairs of the candidate resonances of two-body mean motion that could result in the three-body resonance $\psi = 3\lambda_S - 5\lambda_N + 2\lambda_H$ when both are active, and hence ψ is active too.

and

$$\psi_2 = B\lambda_c - (B-1)\lambda_b - \varpi_b, \tag{9.2}$$

where A and B are integers, λ and ϖ are the mean longitude and longitude of pericentre respectively and indexes a, b and c represent each body on these resonances. Pairs of resonances with ϖ_c are also possible.

Once both resonances are actives, we have

$$\dot{\psi}_1 = \dot{\psi}_2 = 0, \tag{9.3}$$

so

$$\dot{\psi}_1 - \dot{\psi}_2 = (B-A)n_b - Bn_c + An_a. \tag{9.4}$$

Thus, we can define a third resonant angle of ψ as

$$\psi = (B-A)\lambda_b - B\lambda_c + A\lambda_a, \tag{9.5}$$

where

$$\dot{\psi} = \dot{\psi}_1 - \dot{\psi}_2. \tag{9.6}$$

Following this idea, Table 9.1 shows a list of first order resonances found considering the smaller coefficients of the mean longitudes that could have happened between the small moons in the past. We call them *candidate resonances*.

Even reducing the possibilities to four possible pairs of resonant arguments, there are still many to be tested. Perhaps among these pairs, there is a better candidate to be the pair we

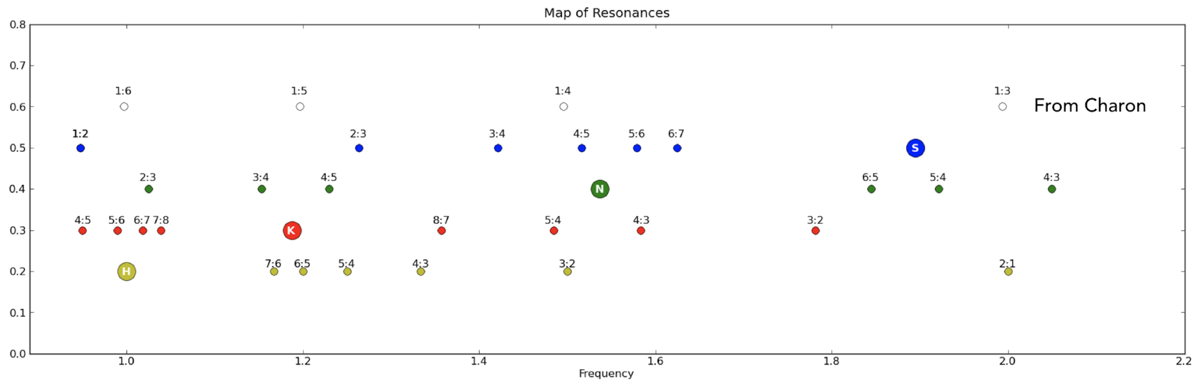

Figure 9.2: Pluto system resonances map. The frequency is normalized by Hydra's mean motion. The bigger colorful circles represent the nowadays satellites' mean motions, with the first letter for each satellite name in it as follows: yellow H for Hydra, red K for Kerberos, green N for Nix and blue S for Styx. The smaller circles lie in the place of the moons' resonances, while the colors relate it to the correspondent moon.

are looking for. Somehow such a pair of arguments would be more likely to have happened in the past between Pluto's small satellites.

To find which one may be the most likely pair of resonant arguments, we create a map of resonance locations at the current region of Pluto and the small satellites. The map is shown in Fig. 9.2. The purpose is to investigate which resonances are nearby the satellites' locations. We use the mean motion frequencies for each moon from Showalter & Hamilton (2015) and normalize them by Hydra's mean motion.

The bigger colorful circles represent the nowadays satellites' mean motions, with the first letter for each satellite name in it as follows: yellow H for Hydra, red K for Kerberos, green N for Nix and blue S for Styx. The smaller circles lie in the location of the moons' frequencies commensurabilities, while the colors relate them to the correspondent moon.

Examining Fig. 9.2, it is possible to measure two indicators that are helpful to select a good pair of resonance to investigate deeper.

For each first order resonance indicated, we look for if there is any other first order resonance located between it and the body we want to capture, which may indicate that the body could be captured into the other resonance first. We call this a *Intervening resonance*. Then, we look at how far away it is from the satellite's current frequencies. To calculate this distance, we use a simple arithmetic average of the distance. These indicators for each first order mean motion resonance are shown in Table 9.2. For example, the third resonance pair in Table 9.2, the 2:1 resonance between Hydra and Styx has no intervening resonance, but the 4:3 resonance between Nix and Styx there is the 5:4 resonance between Nix and Styx, so the 4:3 mean motion resonance candidate between Nix and Styx has one intervening resonance.

From Fig. 9.2 and Table 9.2 it is possible to see that the first pair of mean motion resonance arguments, $\psi_1 = 2\lambda_H - \lambda_S - \varpi_S$ and $\psi_2 = 5\lambda_N - 4\lambda_S - \varpi_S$ between Hydra and Styx, and Nix and Styx, respectively, is the best choice once it has no intervening resonance between

Resonance angle pair	Difference	# Intervening resonances
$\psi_1 = 2\lambda_H$ - λ_S - ϖ_S	5%	0
$\psi_2 = 5\lambda_N$ - $4\lambda_S$ - ϖ_S	1%	0
$\psi_1 = 6\lambda_H$ - $5\lambda_N$ - ϖ_H	22%	3
$\psi_2 = 4\lambda_H$ - $3\lambda_S$ - ϖ_H	30%	1
$\psi_1 = 2\lambda_H$ - λ_N - ϖ_N	30%	0
$\psi_2 = 4\lambda_N$ - $3\lambda_S$ - ϖ_N	8%	1
$\psi_1 = 7\lambda_N$ - $6\lambda_S$ - ϖ_N	5%	1
$\psi_2 = 4\lambda_H$ - $3\lambda_N$ - ϖ_N	14%	1

Table 9.2: Some pairs of the candidates resonances of two-body mean motion that could result in the three-body resonance $3\lambda_S - 5\lambda_N + 2\lambda_H$ when both simultaneously active. The difference of the commensurability from the satellite position in percentage, calculated by arithmetic average. Intervening resonances mean the number of other resonances frequencies between the tabulated one and the actual satellite position.

both resonances frequencies and their related satellites. Additionally, both arguments are the closest to their expected positions. These properties suggest that a simple capture into this pair of two body resonances is the most likely origin of the three-body resonance.

9.3 The Charon's problem

The presence of such a massive second body as Charon makes the study of the system challenging. Since the binary-system can not be considered a point mass, there is no conversion between state vectors and the orbital elements that can properly take the Charon effects into account for the small orbiting bodies.

For weakly perturbed orbits, the *keplerian* or *osculating* orbital elements $(a, e, i, \Omega, \varpi, M)$ are the most usual representation for a celestial object movement, and they are employed to translate the output data resulted from a numerical simulation. On the simple two-body problem, five of those elements are constant in time and represent the geometry of the orbit. The other element increases in time and indicates the angular position of the body in the orbit.

Depending on how close to the real system its representation in orbital elements is needed, it will be necessary that those elements do not be stationary. For example, in an oblate planet, the stationary orbital elements can not represent the geometry of the orbit well anymore since now it will be a precessing ellipse, where Ω and ϖ will vary over time. Renner & Sicardy (2006) algorithm, based in Borderies-Rappaport & Longaretti (1994) equations, is the typically used method to transform velocities and positions into the *epicyclic* orbital elements and vice versa. It takes into account the oblateness of the central body and provides an improved approximation over the osculating elements.

Lee & Peale (2006) developed an analytical theory considering Nix and Hydra as test particles orbiting around the binary system. They represented the motion of the satellite as a superposition of four components: a circular motion of a guiding center, the epicyclic

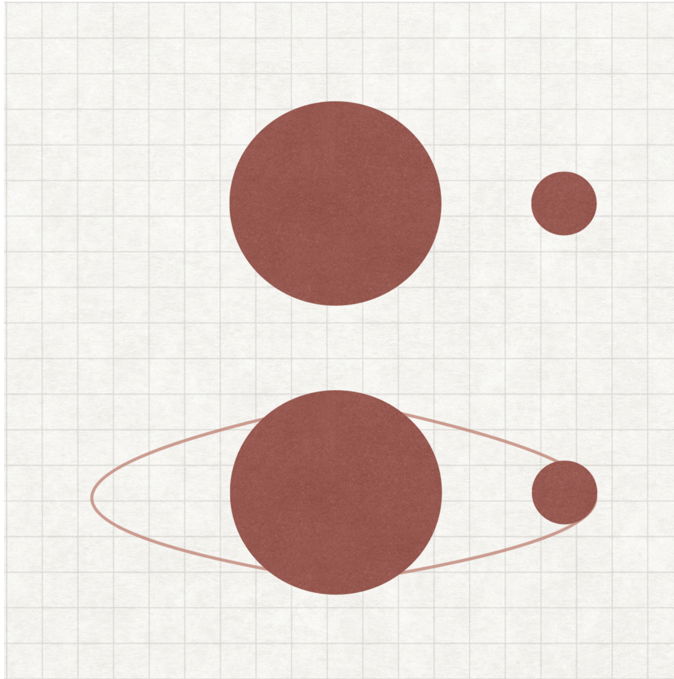

Figure 9.3: J_2 effective idea illustration. Similar to the case of an oblate planet, the J_2 effective consider Pluto plus Charon as a single body with a J_2 term in its gravitational potential.

motion, the vertical motion, and the forced oscillation due to the potential rotating on the mean motion of Pluto-Charon. The authors used the average gravitational potential ignoring the perturbations from the Sun and reported their results to match that of an oblate planet with $J_2 = m_P m_C/[2(m_P + m_C)^2]$, where m_P is Pluto mass and m_C Charon mass. Here the reference is taken to be the radius of Charon's orbit rather than that of the planet. Fig. 9.3 illustrates the idea of mimicking the Charon perturbations on the small satellites with Pluto and Charon combined as one single body with a J_2 coefficient.

Here we employ this approximation, that we call J_2 effective , to convert the state vector to orbital elements for the small satellites. We define J_2 effective as

$$J_2 \text{ effective } = J_2 \text{ Pluto} + J_2 \text{ Charon}. \tag{9.7}$$

Since J_2 Pluto is very small, we disregard it and for the J_2 Charon we have

$$J_2 \text{ Charon} = \frac{1}{2}\left(\frac{m_C}{m_P + m_C}\right)\left(\frac{a_C}{R_P}\right)^2, \tag{9.8}$$

where R_P means Pluto's radius.

We tested the improvement of using this model by integrating some orbits of a test particle around the Pluto-Charon system. Fig. 9.4 shows the semimajor axis and eccentricity over

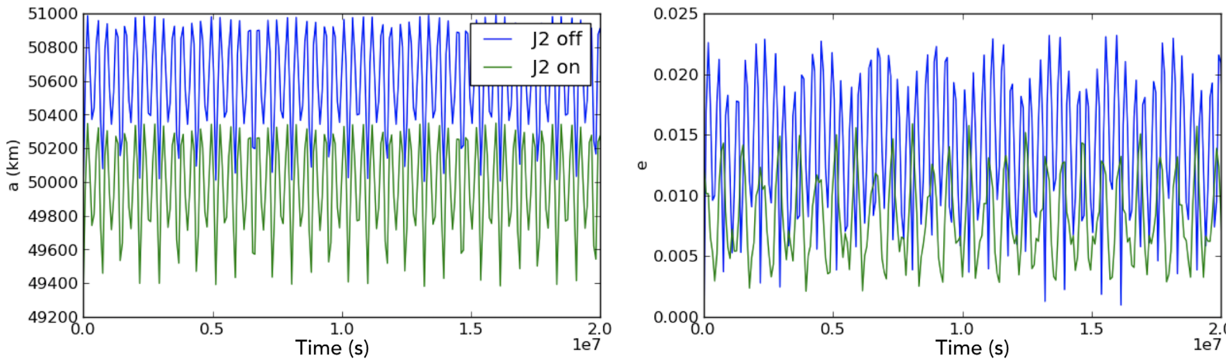

Figure 9.4: Test of the J_2 *effective* approximation. A test particle with initial semi-major axis of 50,000 km and zero eccentricity is converted to state vector with and without considering the J_2 effective. The system is evolved in time for 2×10^7 s. The green curves with J_2 effective do a better job of representing the orbit than the blue curves.

time of a particle that we start with a semimajor axis of 50000 km and zero eccentricity.

We consider two conversions from state vector to orbital elements to be used as an input to the numerical simulation, and then again from the state vector output to geometric orbital elements: with using the J_2 effective (in green) and without (in blue).

It is clear by Fig. 9.4 that when we do not consider the J_2 effective, the resulted orbit is too far from its initial semimajor axis. At the same time, the eccentricity is higher, and with a larger oscillation than when J_2 effective is considered. The high frequency oscillations are at Charon's orbital period and result from terms in the time-dependent potential that are not captured with our averaged potential approach.

By using the J_2 effective we can calculate a set of orbital elements instantly, allowing us to investigate the resonances actives or nearby the satellites of the Pluto-Charon System with better visualization of the orbits. This approach has been used in other works (Showalter & Hamilton 2015, Amarante 2017, Vieira Martins 1989).

Chapter 10

Numerical simulations

To develop the study on the origin of the resonances among the satellites, we perform N-body numerical simulations placing the satellites in an orbital configuration more compact than the current one and evolving the system in time under the influence of the tidal force due to the Pluto-Charon binary.

10.1 Hnbody, a n-body integrator

Here we use the Hnbody package by Rauch & Hamilton (2002) to perform the numerical simulations. It consists of a hierarchical n-body package that integrates the motion of self-gravitating particles where a single body dominates the total mass. The main algorithms are based on Wisdom-Holman type symplectic integration techniques, where Keplerian motion is treated exactly.

The package also includes ODE integrators such as Bulirsch-Stoer and Runge-Kutta. Among many other options, the user can choose the system coordinates that can be either Jacobi (barycentric) or canonical bodycentric. The particles can be considered into three different groups:

- HWPs (*Heavy Weight Particles*), which includes the dominant body, whose self- and external-interactions are accounted for.
- LWPs (*Light Weight Particles*), whose interactions with HWPs (and, optionally, ZWPs) is computed, but their mutual interaction is ignored.
- ZWPs (*Zero Weight Particles*), are the particles treated as massless. They are always perturbed by HWPs, but may or may not be perturbed by LWPs.

The package also enables the user to add external forces such as tidal and drag forces. A modular and intuitive interface allows the user to decide on which body the external force will be applied and for how long. Moreover, it is possible to choose the magnitude and direction of these external forces.

	Scenario RC	Scenario AC
Central body	Pluto	Pluto+Charon
GM (km^3/s^2)	8.70×10^2	9.75×10^2
J_2 *effective*	-	14.79

Table 10.1: Central Body Approach used in the numerical simulations. The Scenario RC one consists in having Pluto as the central body. In the Scenario AC a single body with the mass equivalent to the sum of the masses of Pluto and Charon, taking into account a J_2 *effective* in the central body.

	GM
Pluto	8.70×10^2
Charon	1.05×10^2
Nix	3.0 ± 2.7
Hydra	3.2 ± 2.8
Styx	$0.0 + 1.0$
Kerberos	1.1 ± 0.6

Table 10.2: GM given in 10^{-3} km^3/s^{-2} considered on the numerical simulations for Pluto, Charon, Nix, Hydra, Styx, and Kerberos. We consider only the nominal values (Showalter & Hamilton 2015).

10.2 Setting up input and output parameters

In this work we have performed numerical simulation using two different approaches to describe the Pluto and Charon binary system.

The first one consists in having Pluto as the central body, Charon and the small moons are declared as *Heavy Weight Particle*, so they are disturbed by Pluto, Charon and themselves. The tidal force is applied on Charon, making it to migrate outwards. This is the case we just use J_2 *effective* to convert the output state vectors to geometrical orbital elements at the end of the simulations. We call it *Scenario RC (Real Charon)*.

In the second approach, the only difference from the first is that Charon is removed from the simulation and the central body is replaced by a single body with an oblate radius of 1187 km and a mass equivalent to the sum of the masses of Pluto and Charon, taking into account a J_2 *effective* $= 14.79$ as a central body (Table 10.1). We call it *Scenario AC (Artificial Charon)*.

The masses used for each satellite are reported in Table 10.2 and are from Showalter & Hamilton (2015).

We consider a range of initial semimajor axis for each satellite, all closer to Pluto than their current orbits, in order to simulate the system starting before tidal migration, has begun.

For each initial semimajor axis and considering circular orbits, we calculate the satellites' state vectors, and vice versa, at the end of the simulation, we convert the geometrical orbital

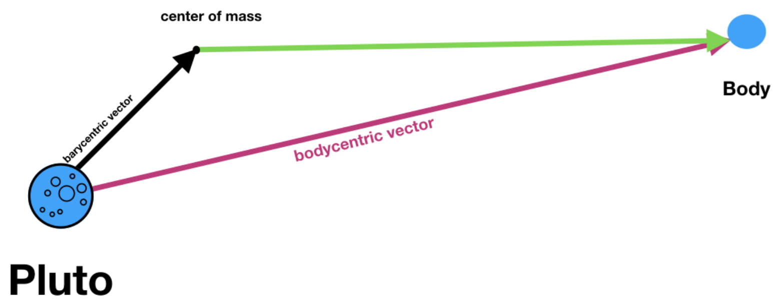

Figure 10.1: Barycenter conversion illustration. To convert the moon position on the barycentric frame at the end of the simulation, we subtract the barycentric vector from the bodycentric vector.

elements from the output state vectors using a routine called *Corrected Potential elements*. These elements are slightly different from those by Borderies-Rappaport & Longaretti (1994) and will be discussed in a forthcoming paper by Rimlinger and Hamilton (private communication).

Barycenter conversion

Because Charon is so massive, orbits are best described relative to the barycenter of the system rather than Pluto itself. An indispensable conversion to be made is to place the data of the small moons in relation to Pluto before starting the simulation inside HNbody, because we use the bodycentric frame. Then, convert the output back to the barycentric frame, once we want to look the orbits of the small moon. Charon is the only moon we do not need to make this conversion. In our integrations we do that by simply adding and subtracting the barycentric vector to/from the bodycentric vector/moon vector on barycentric frame, respectively, for each small moon (See Fig. 10.1).

10.3 Results

Captures by Charon

The first step we want to produce is the capture of the small satellites by the resonances with Charon. We are looking for the resonances currently close to the satellites: Styx on the 3:1, Nix on 4:1, Kerberos on 5:1, and finally Hydra on 6:1 (Buie et al. 2006, 2013).

To the following simulations, we considering the Scenario RC, Charon plus a particle, and a tidal force applied on Charon.

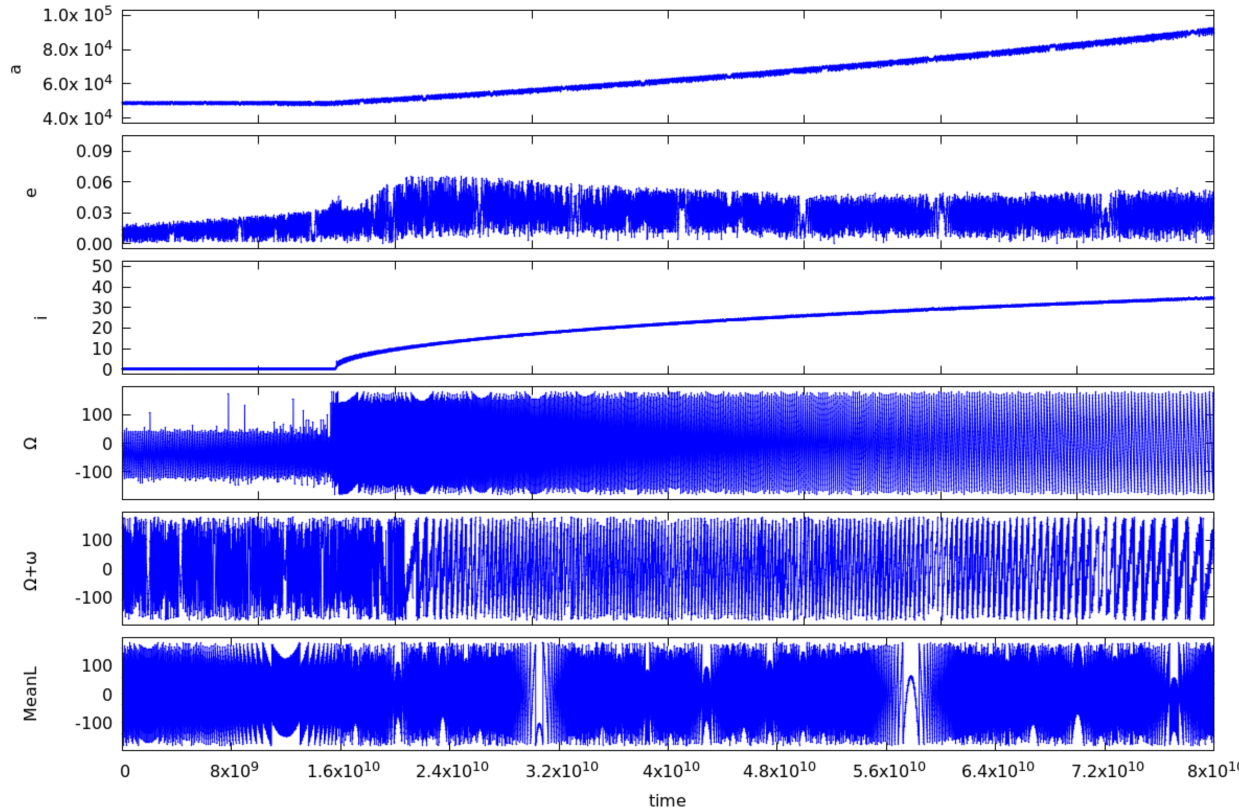

Figure 10.2: Geometric orbital elements of a satellite being captured on a 3:1 mean motion resonance by Charon under a tidal force with characteristic time scale 1×10^{-11} seconds. Charon is initially located at a semi-major axis of 19,595 km and the particle at a semi-major axis of 48,690 km.

3:1 Resonance

To try to capture a particle into the 3:1 resonance with Charon, we use a small tidal force acting on Charon with characteristic time scale $\times10^{-11}$ seconds. Charon is initially located at a semi-major axis of 19,595 km and the particle at a semi-major axis of 48,690 km.

Fig. 10.2 shows the variation of a small moon geometric orbital elements. The semi-major axis a, eccentricity e, inclination i, argument of the nodo ascendent Ω, pericenter longitude $\Omega + \varpi$ and the mean longitude λ over time in seconds.

Analyzing the semi-major axis evolution with time, we see the moment when it starts to grow (around $t = 1.5 \times 10^{10}$ s) which means Charon has captured the moon that starts to migrate forwards along with it. We also see that the inclination also starts to increase at the same time, so the resonance that has captured the moon is of the inclination type, *i.e.*, with an inclination term in the resonance angle.

To confirm if this is the 3:1 resonance between Charon and the moon, we checked the ratio between the semi-major axes of Charon and the moon (Fig. 10.3). If they are migrating

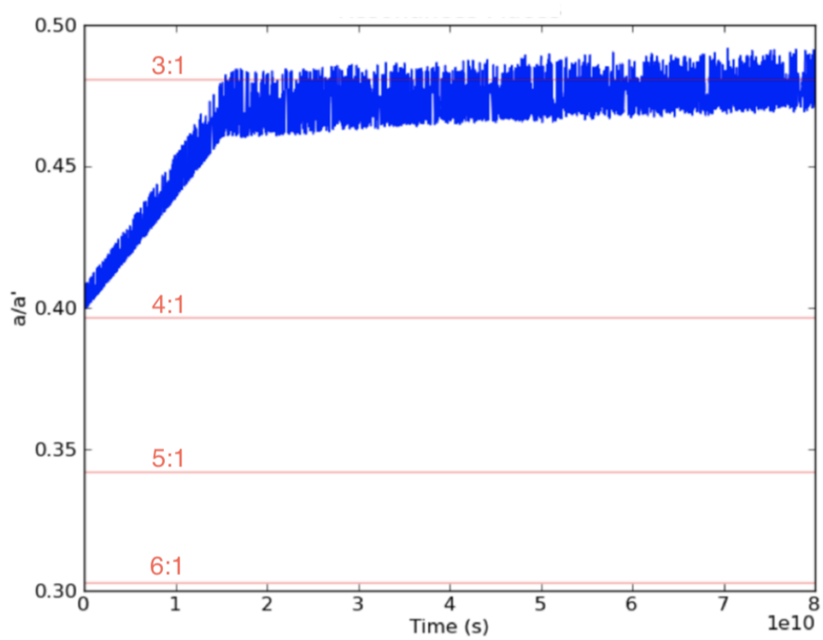

Figure 10.3: Ratio between Charon's semi-major axis (a) and the moon's semi-major axis (a'). Charon is migrating under tidal force. The red lines denote resonances 3:1, 4:1, 5:1 6:1, from top to bottom.

at the same rate, and also if the migration starts around the 3:1 resonance location, then we will know it is, in fact, the 3:1 resonance. An equivalent analysis using the mean motion is possible. Note here we are not concerned with the exact resonant angles that are captured, otherwise, we should plot the resonance angle and check for the libration of it. Here it is enough to know if it is a 3:1 mean motion resonance.

In Fig. 10.3 Charon is migrating under a tidal force, so its semimajor axis increases in time, which results in a ratio between Charon and the moon semimajor axes also increasing in time. At the moment the moon is captured, it starts to have its semimajor axis also moving outward at the same rate, so the ratio between both migrating semimajor axes is almost constant.

4:1 Resonance

To reproduce a capture between Charon and a small moon on the 4:1 mean motion resonance, we repeated almost the same process of the 3:1 resonance, except for the location of Charon, that was started at a semi-major axis of 19,992 km and the particle at a semi-major axis of 50,865 km.

We started trying the capture within the same magnitude of the tidal force used at the 3:1 case. However, only with a tidal drag force 1000× weaker was possible to reach a capture. This slower timescale is indicative of a weaker high-order resonance.

The Fig. 10.4 show the orbital elements of a moon that has been captured by Charon on

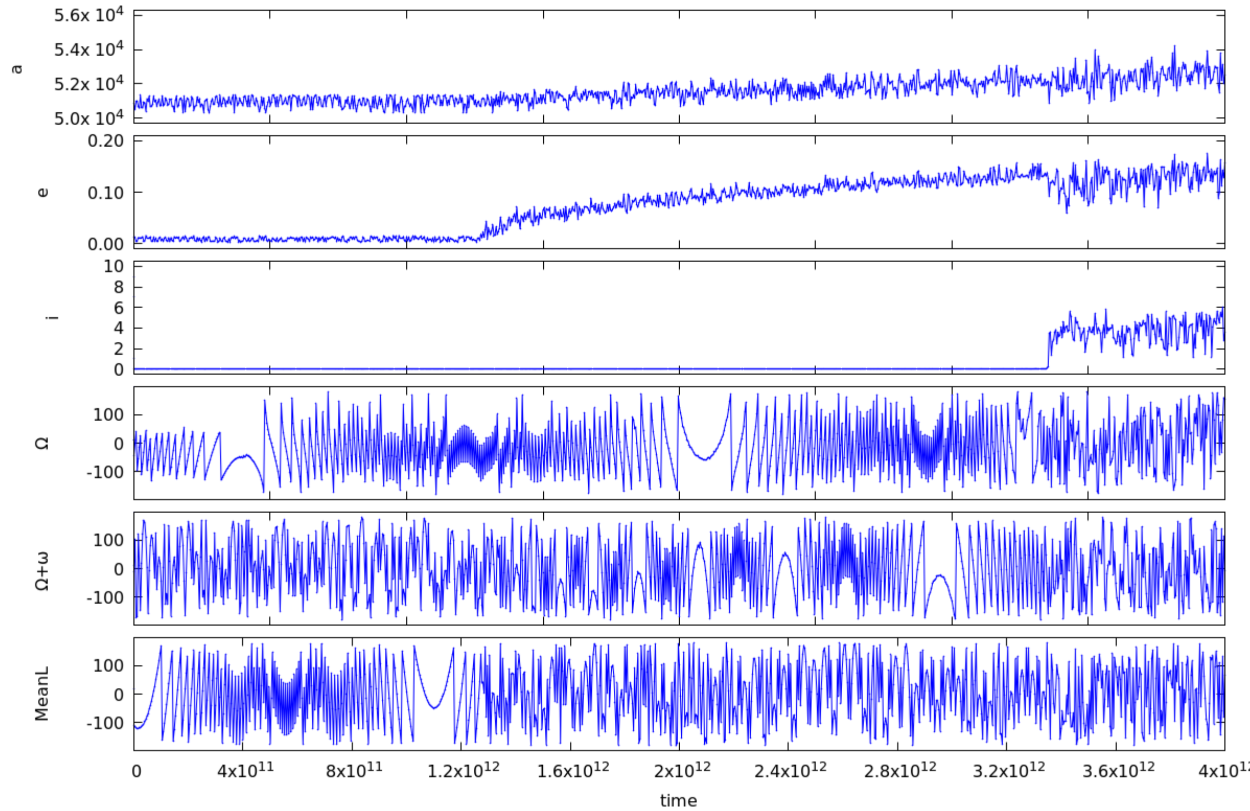

Figure 10.4: Geometric orbital elements of a satellite being captured on a 4:1 mean motion resonance by Charon under a tidal force with characteristic time scale 1×10^{-14} seconds. Charon is initially located at a semi-major axis of 19,992 km and the particle at a semi-major axis of 50,865 km.

a 4:1 mean motion resonance.

The eccentricity evolution shows a change in its behavior around t$\sim 1.2 \times 10^{12}$, when it starts to increase. There is also a correlated small increase of the semimajor axis.

In this case, the capture was into an eccentricity type of mean motion resonance, though the moon inclination is weakly affected as well.

Fig. 10.5 shows the moment the moon is captured by Charon on the 4:1 resonance, which is when Charon's and the moon's semimajor axes start to grow at the same rate, so the ratio between them changes from increasing to nearly constant.

5:1 Resonance

For the 5:1 mean motion resonance, it was not possible to produce the capture without adding an artificial eccentricity to Charon. We were able to capture into the 5:1 resonance when Charon had eccentricity $e = 0.01$.

Fig. 10.6 shows the evolution of the moon's orbital elements. Moreover, Charon must

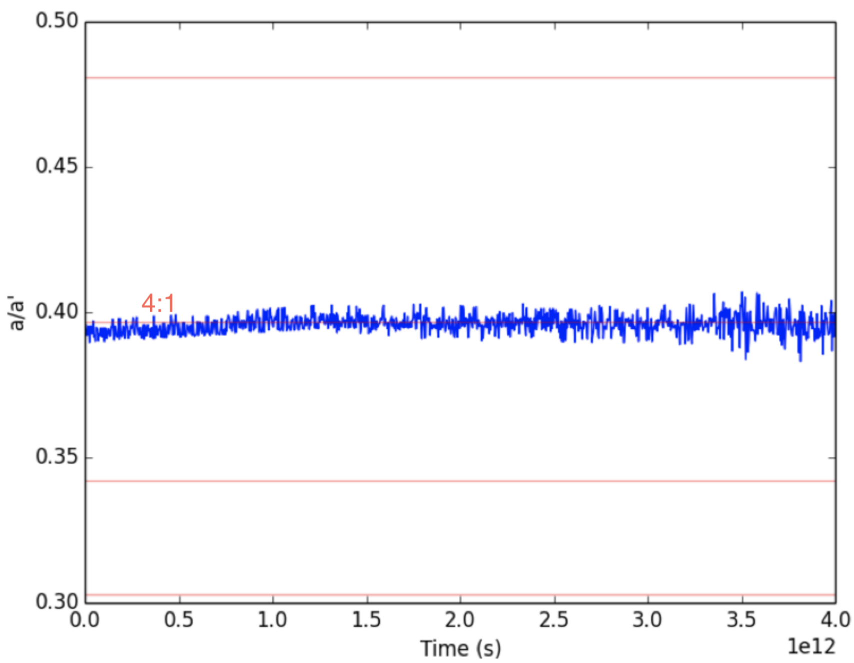

Figure 10.5: Ratio between Charon's semi-major axis (a) and the moon's semi-major axis (a'). Charon is migrating under tidal force. The red lines denote resonances 3:1, 4:1, 5:1 6:1, from top to botton.

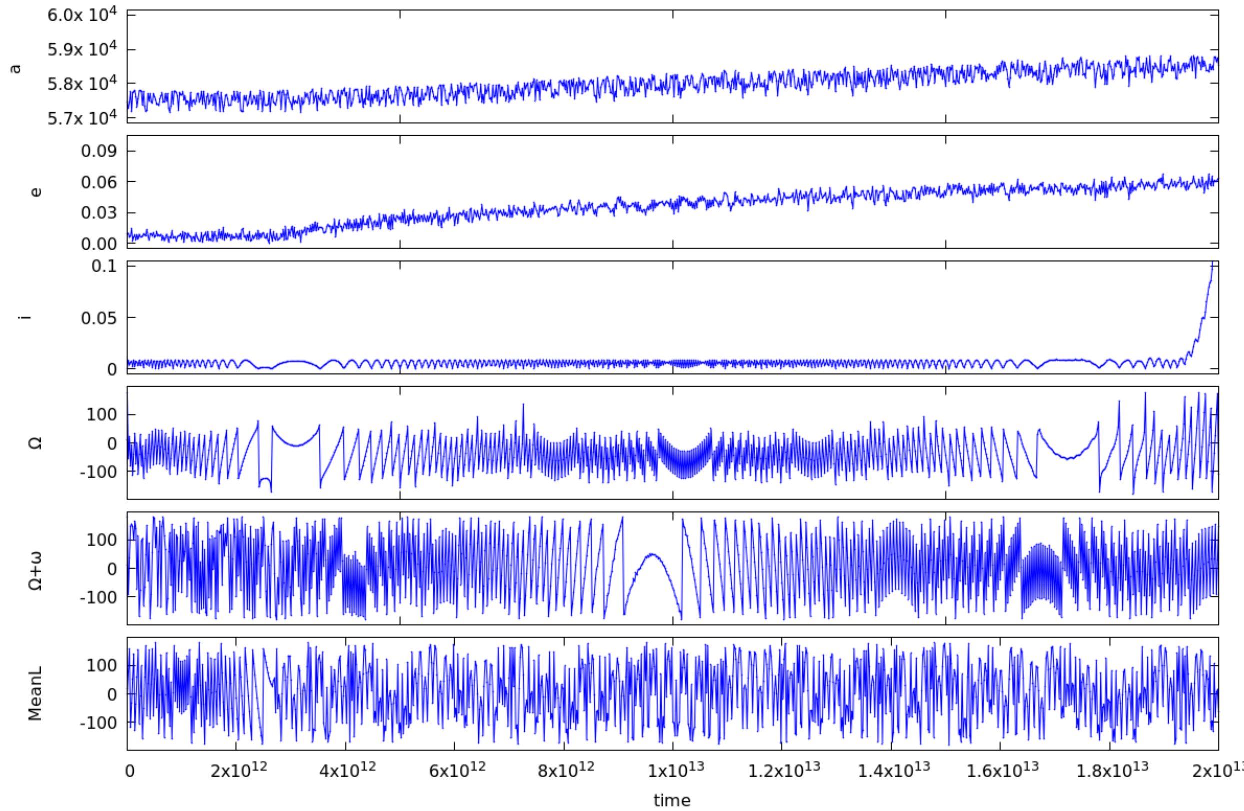

Figure 10.6: Geometric orbital elements of a moon being captured on a 5:1 mean motion resonance by Charon under a tidal force with characteristic time scale 1×10^{-15} seconds and eccentricity of 1×10^{-2}. Charon is initially located at a semimajor axis of 19,596 km and the particle at a semimajor axis of 57,461 km.

migrate even slower in this case, so the magnitude of the tidal force was reduced by a factor of 10 from the previous 4:1 experiments. Charon is initially located at a semimajor axis of 19,596 km and the particle at a semimajor axis of 57,461 km.

The moon's semimajor axis starts to grow around t$\sim 3 \times 10^{12}$ s. Simultaneously, the eccentricity also starts to increase, indicating that the capture was into an eccentricity type of mean motion resonance.

Around t$\sim 1.9 \times 10^{13}$ s, the inclination starts to grow suddenly, what indicates that the moon was captured into another mean motion resonance, this time in an inclination type.

The ratio between Charon's and the moon's semimajor axes is shown in Fig. 10.7. It can be seen that the 5:1 commensurability is active for nearly the entire duration of the integration.

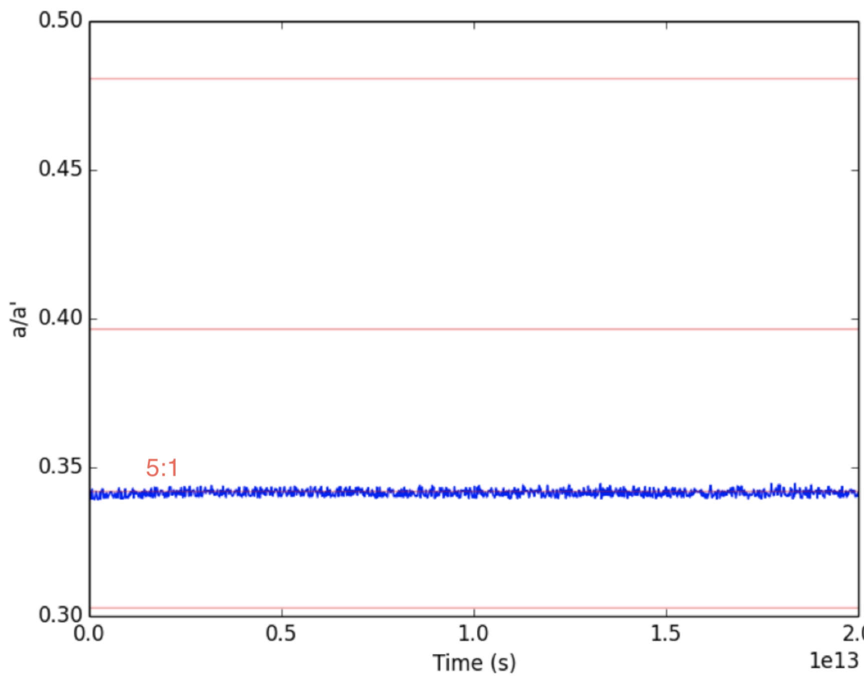

Figure 10.7: Ratio between Charon's semi-major axis (a) and the moon's semi-major axis (a'). Charon is migrating under tidal force. The red lines denote resonances 3:1, 4:1, 5:1 6:1, from top to bottom.

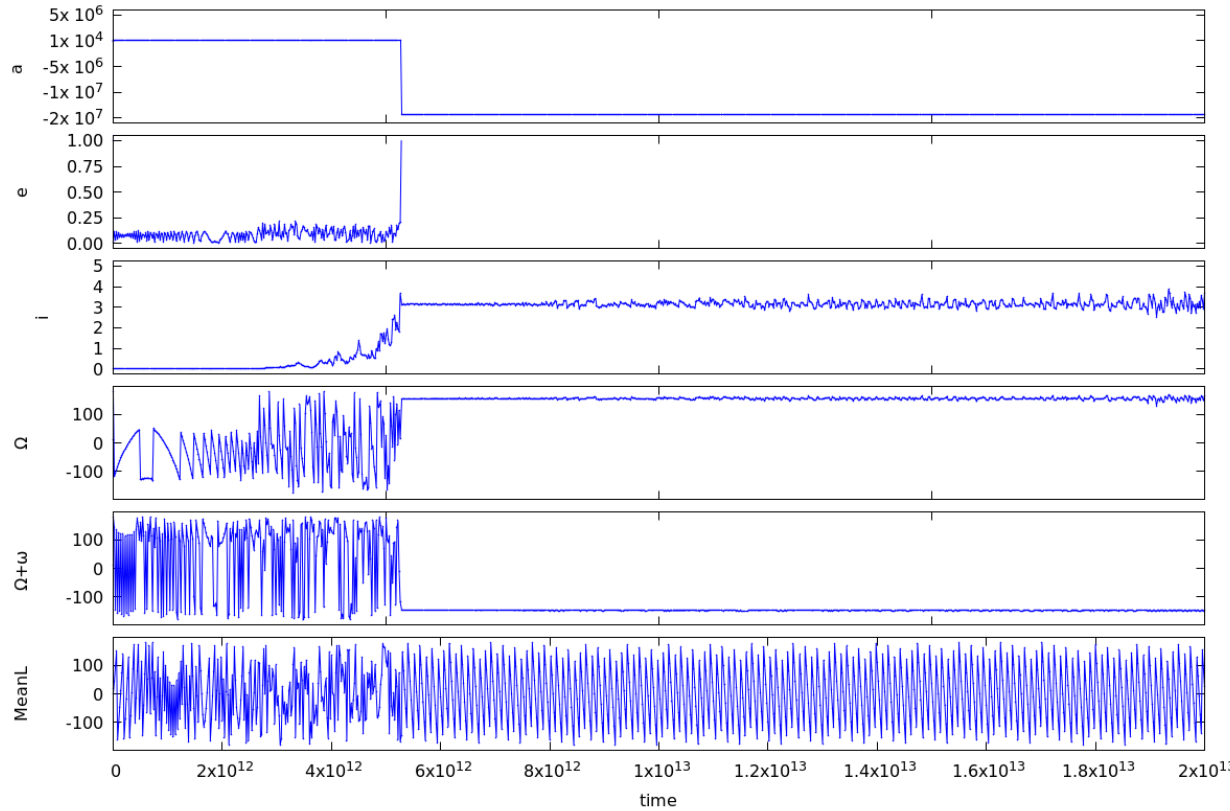

Figure 10.8: Geometric orbital elements of a moon being captured on a 6:1 mean motion resonance by Charon under a tidal force with characteristic time scale 1×10^{-15} seconds and eccentricity of 1×10^{-1}. Charon is initially located at a semi-major axis of 19,596 km and the particle at a semi-major axis of 62,325 km.

6:1 Resonance

The last mean motion resonance we want to test the capture by Charon is the 6:1. In this case, again, it is necessary to add an initial artificial eccentricity to Charon, so an eccentricity of 1×10^{-1} s was considered. The tidal force magnitude is still the same as the 5:1 resonance case. The geometric orbital elements of the moon are shown in Fig. 10.8. Charon is initially located at a semimajor axis of 19,596 km and the particle at a semimajor axis of 62,325 km.

The capture into the 6:1 mean motion resonance seems to happen around t$\sim 3\times10^{12}$ s, the time the inclination starts to increase, indicating the resonance is of the inclination type (Fig. 10.8).

Unlike the other captures, the 6:1 capture resulted in an ejection of the moon from the system around t $\sim 5\times10^{12}$ s. Chaotic overlap of different eccentricity resonances is most likely the cause of the instability. Fig. 10.9 also shows clearly the moment that the moon escapes.

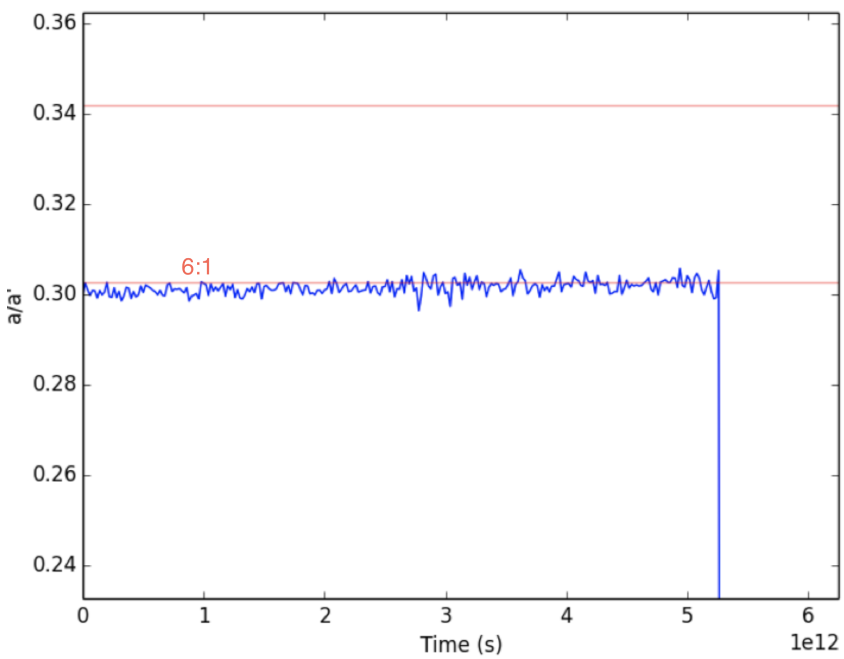

Figure 10.9: Ratio between Charon's semi-major axis (a) and the moon's semi-major axis (a'). Charon is migrating under tidal force. The red lines denote resonances 3:1, 4:1, 5:1 6:1, from top to botton.

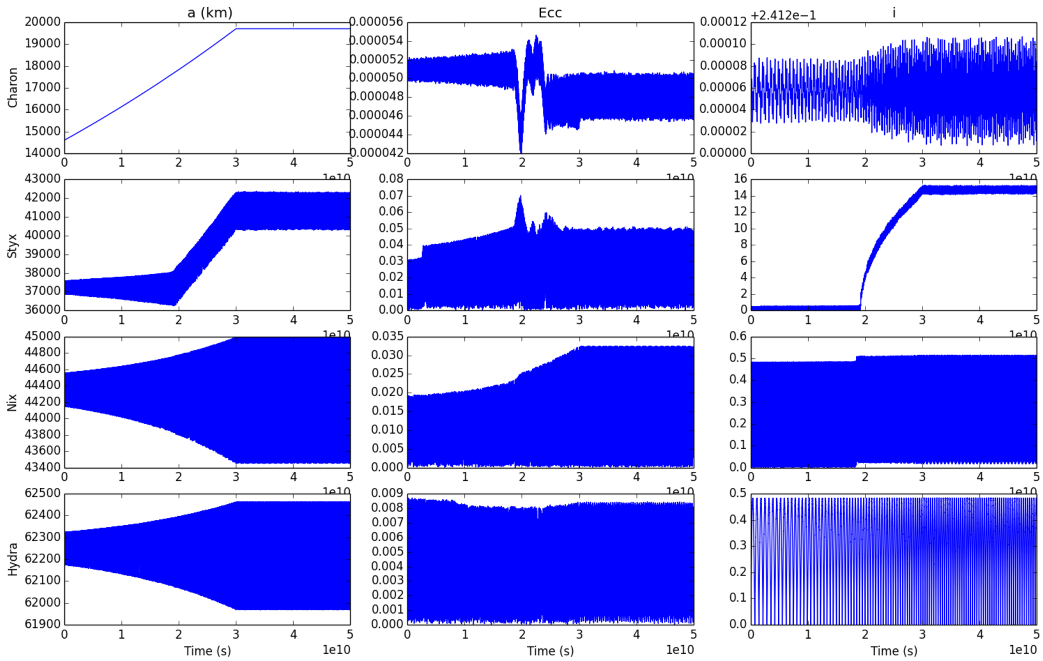

Figure 10.10: Charon, Styx, Nix, and Hydra geometric orbital elements over time. Charon captured Styx into the 3:1 mean motion resonance, while Nix and Hydra seems to be perturbed by its presence, but was not captured into any resonance.

Most likely Charon resonance

The simulation shown in Fig. 10.10 has three small moons, Styx, Nix and Hydra, to verify which resonance is easier to happen and with which moon. Charon captured Styx into the 3:1 mean motion resonance around t$\sim 2 \times 10^{10}$ s, while Nix and Styx seem to be perturbed by its presence, but were not captured into any resonance. The growing in the inclination of Styx revels a capture into an inclination resonance type. Fig. 10.11 confirmed it and showed the resonant argument responsible for the capture, $3\lambda_S - \lambda_C - 2\Omega_S$, that is librating from t$\sim 2 \times 10^{10}$ s to the end of the simulation.

These results demonstrate that the small satellites of the Pluto-Charon system can be captured into the 3:1, 4:1, 5:1, 6:1 mean motion resonances with Charon. However, for the case of the 5:1 and 6:1 resonances, it was possible to capture into, except when some non-zero eccentricity was added to Charon. We find that the 3:1 mean motion resonance between Charon and Styx, in inclination, is the most common outcome of tidal migration.

Captures by small moons

We now proceed to investigate resonance capture among the small moons.

As described above, we are looking for two particular mean motion resonances among

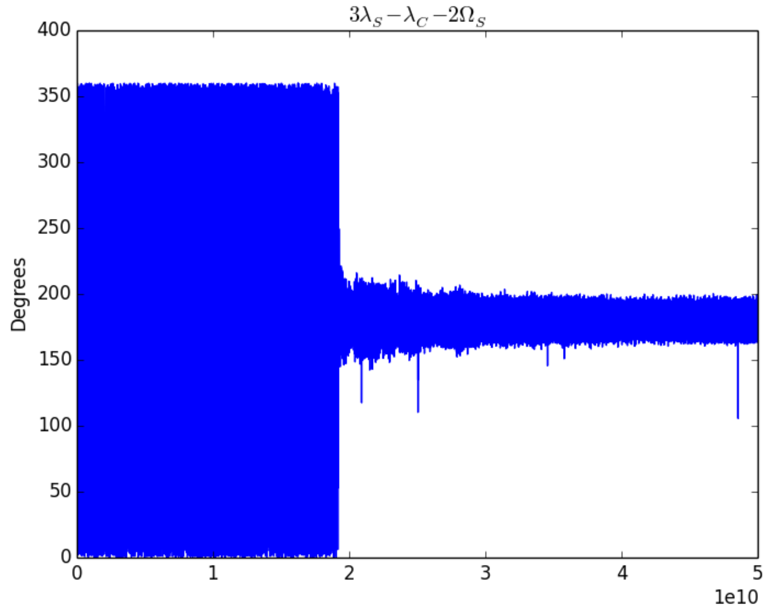

Figure 10.11: Argument of 3:1 resonance over time. Charon captured Styx into the $3\lambda_S - \lambda_C - 2\Omega_S$ resonance angle, that is librating from the time of the capture t$\sim 2 \times 10^{10}$ s to the end of the simulation.

two small moons that, once activated at the same time, will result in the three body mean motion resonance $\psi = 3\lambda_S - 5\lambda_N + 2\lambda_H$.

Since the three body mean motion resonance $3\lambda_S - 5\lambda_N + 2\lambda_H$ only involves Styx, Nix, and Hydra, for simplicity, we will not consider Kerberos in the following numerical simulations.

We tested different initial semi-major axes for the small moons on a range of 3,000 km around their current semi-major axes.

From the pair of resonances we have identified at Chapter 9, $\psi_1 = 2\lambda_H - \lambda_S - \varpi_S$ and $\psi_2 = 5\lambda_N - 4\lambda_S - \varpi_S$, ψ_1 between Hydra and Styx has the smaller coefficients of the longitudes, so it may be easier to capture another moon into once it should be stronger.

So in the following simulations, we focus on capturing into these two 2-body resonances. Each simulation is a select example of dozens of simulations results that we had varying the semi-major axis of each moon and the tidal force magnitude.

Simulation 1

In the Simulation 1 we consider the Scenario RC, Charon's initial semi-major axis is 17,935 km, with characteristic time scale 1×10^{-16} seconds, Styx already captured in the Charon 3:1 resonance and starting at a semi-major axis of 37,563 km and Hydra initial semi-major axis is 62,455 km. Nix and Kerberos were not include in this simulation. Table 10.3 summarizes the initial parameters to this and the next simulations.

Fig. 10.12 shows the orbital evolution in time of Charon's, Styx's, and Hydra's semi-major axis (a), eccentricity (Ecc) and inclination (i).

<table>
<tr><th>Simulation</th><th></th><th></th><th>Charon</th><th>Styx</th><th>Nix</th><th>Hydra</th></tr>
<tr><td rowspan="2">1</td><td rowspan="2">Scenario RC</td><td>a (km)</td><td>17,935</td><td>37,563</td><td>-</td><td>62,455</td></tr>
<tr><td>Forces</td><td>$1 \times 10^{-16}\hat{v}$</td><td>-</td><td>-</td><td>-</td></tr>
<tr><td rowspan="2">2</td><td rowspan="2">Scenario AC</td><td>a (km)</td><td>-</td><td>38,460</td><td>48,486</td><td>64,721</td></tr>
<tr><td>Forces</td><td>-</td><td>$1{\times}10^{-13}\hat{v}$</td><td>-</td><td>-</td></tr>
<tr><td rowspan="2">3</td><td rowspan="2">Scenario RC</td><td>a (km)</td><td>-</td><td>41,154</td><td>48,512</td><td>64,932</td></tr>
<tr><td>Forces</td><td>-</td><td>$1{\times}10^{-15}\hat{v}$
$1{\times}10^{-14}\hat{S}$</td><td>-</td><td>-
$1{\times}10^{-15}\hat{S}$</td></tr>
<tr><td rowspan="2">4</td><td rowspan="2">Scenario AC</td><td>a (km)</td><td>-</td><td>41,154</td><td>47,798</td><td>64,932</td></tr>
<tr><td>Forces</td><td>-</td><td>$1{\times}10^{-15}\hat{v}$
$1{\times}10^{-14}\hat{S}$</td><td>-</td><td>-
$1{\times}10^{-15}\hat{S}$</td></tr>
</table>

Table 10.3: Initial parameters of the satellites for the simulations 1, 2, 3 and 4. Charon, Styx, Nix and Hydra semi-major axes, external forces applied and the correspondent scenarios.

It is possible to see that when Styx achieves the semi-major axis of 39,000 km it captures Hydra into an eccentric mean motion resonance. From that moment on, Hydra starts to migrate outwards together with Styx and Charon, and its eccentricity starts to grow.

Fig. 10.13 shows the two resonance argument angles from the mean motion resonances identified in Fig. 10.12: the 3:1 resonance between Styx and Charon $3\lambda_S - \lambda_C - 2\Omega_S$ and 2:1 between Styx and Hydra $2\lambda_H - \lambda_S - \varpi_H$.

We did not find other capture into the 2-body resonances among the small satellites besides the resonance between Styx and Hydra. The resonance argument has Hydra's pericenter instead of Styx's pericenter.Although in this simulation we have achieved a capture between Hydra and Styx into the 2:1 resonance, we are seeking the resonance argument with the other pericenter (See Table 9.1)

Simulation 2

In order to find other constraints on the capture conditions, in Simulation 2 we use the Scenario AC instead of having Charon during the next numerical simulations. This eliminates most of the short-period oscillations visible in Fig. 9.4 and makes the system easier to interpret.

So, the central body is a single body with Pluto and Charon's mass combined (GM=$9.75{\times}10^2$) and a J_2 *effective* of 14.79. In this case, we apply the tidal force directly on Styx, assuming the captures 3:1 between Charon and Styx has already happened.

Styx initial semi-major axis is 38,460 km, with characteristic time scale $1{\times}10^{-13}$ seconds. Nix and Hydra initial semi-major axes are 48,486 km and 64,721 km, respectively. Kerberos was not include in this simulation.

Fig. 10.14 shows an example of the results using these parameters. The geometric orbital elements eccentricity and semi-major axis for Styx, Hydra and Nix over time shows a capture of Nix by Styx around t$\sim 5{\times}10^{11}$ s, when Nix semi-major axis starts to grow, as it migrates in tandem with Styx. The eccentricity plot shows that Styx eccentricity is growing, so the term on the resonance argument must be related to Styx's eccentricity. This result is established in Fig. 10.15, which shows our resonant argument of interest $4\lambda_N - 3\lambda_S - \varpi_S$ librating.

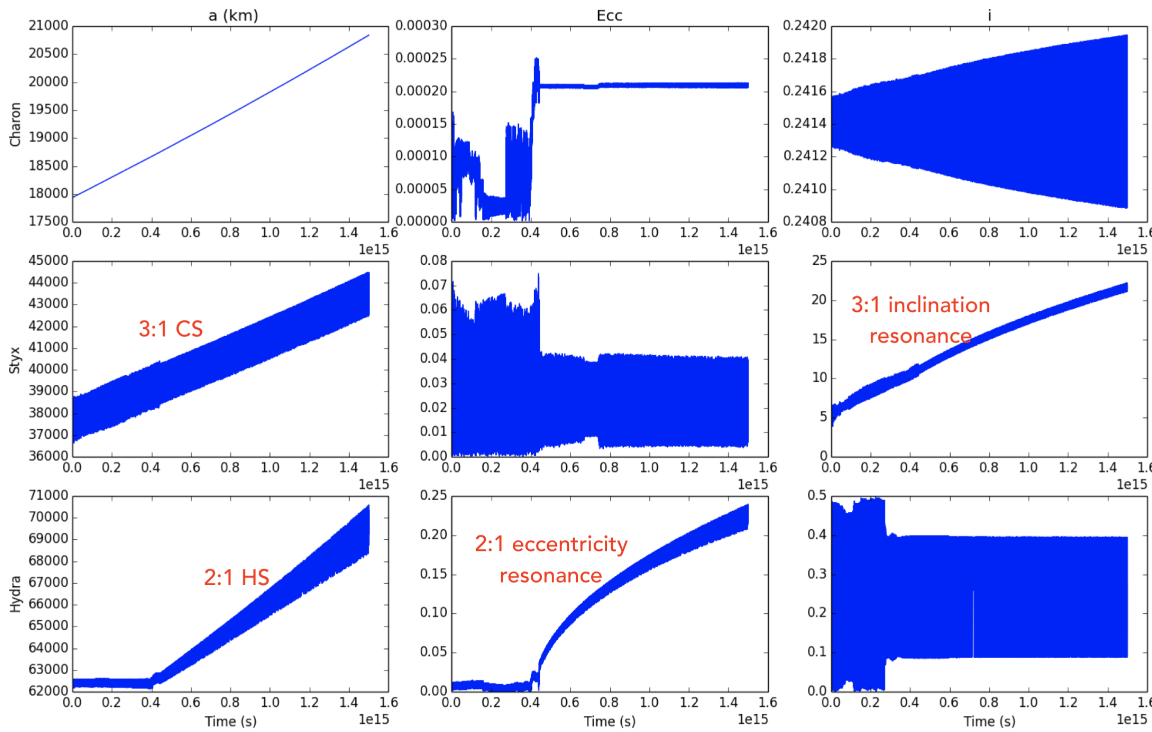

Figure 10.12: Charon, Styx and Hydra geometric orbital elements over time. Styx starts captured by Charon in inclination 3:1 resonance. Around t$\sim 4 \times 10^{14}$ Styx captures Hydra into the 2:1 mean motion resonance in eccentricity.

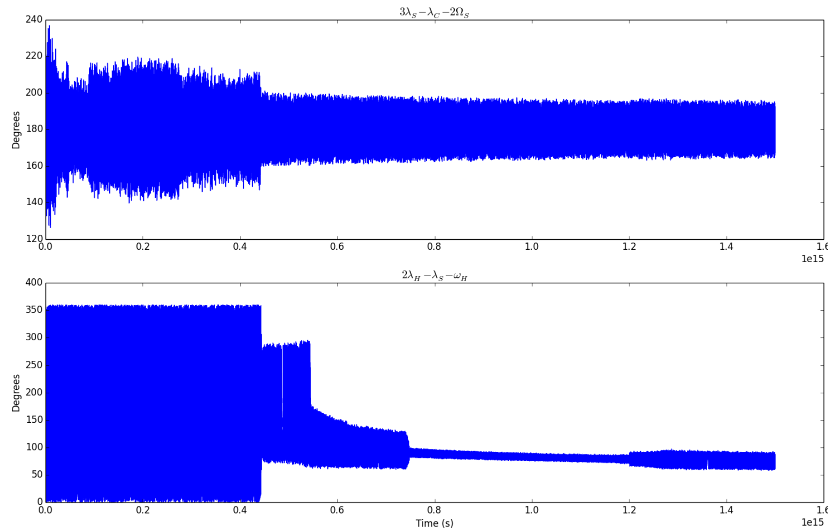

Figure 10.13: Argument of 3:1 and 2:1 resonances over time. Charon captured Styx into the $3\lambda_S - \lambda_C - 2\Omega_S$ resonance angle, that is librating. The 2:1 resonance between Styx and Hydra angle $2\lambda_H - \lambda_S - \varpi_H$ is also librating, starting from t$\sim 4.5 \times 10^{14}$ s until the end of the simulation.

After that, around t$\sim 5\times10^{12}$ s, Hydra seems to be captured by Styx into an eccentricity mean motion resonance. Fig. 10.15 shows the moment when the capture into the argument $2\lambda_H - \lambda_S - \varpi_H$ happens, resulting in the angle libration.

These results show some of the possible captures into resonances among the small satellites, but we still could not reproduce the specific captures that we need to result on the three body resonance. Even with the J_2 *effective* approximation, the sensitivity of the system makes hard to achieve this task. One important point is the growing eccentricities that make the moons' captures even less stable. More realistic simulation would include tidal damping of eccentricity.

Accordingly, in the next numerical simulations we will use an artificial force to damp the orbital eccentricity of the moons captured by resonances. We expect that a drag force or even the tidal force can circularize those orbits after the chain of resonances happen. But we leave a detailed study for future work.

Simulation 3

In Simulation 3, besides experiencing a tidal force of characteristic time scale 1×10^{-15} seconds, Styx also has an external eccentricity damping force of from $\vec{F} = 1 \times 10^{-14}\hat{S}$. We apply a similar force but 10× weaker to Hydra to damp its eccentricity.

Styx initial semi-major axis is 41,154 km, Nix initial semi-major axis is 48,512 km and Hydra initial semi-major axis is 64,932 km. Kerberos was not include in this simulation.

The semi-major axis and eccentricities of Styx, Hydra, and Nix plus some mean motion

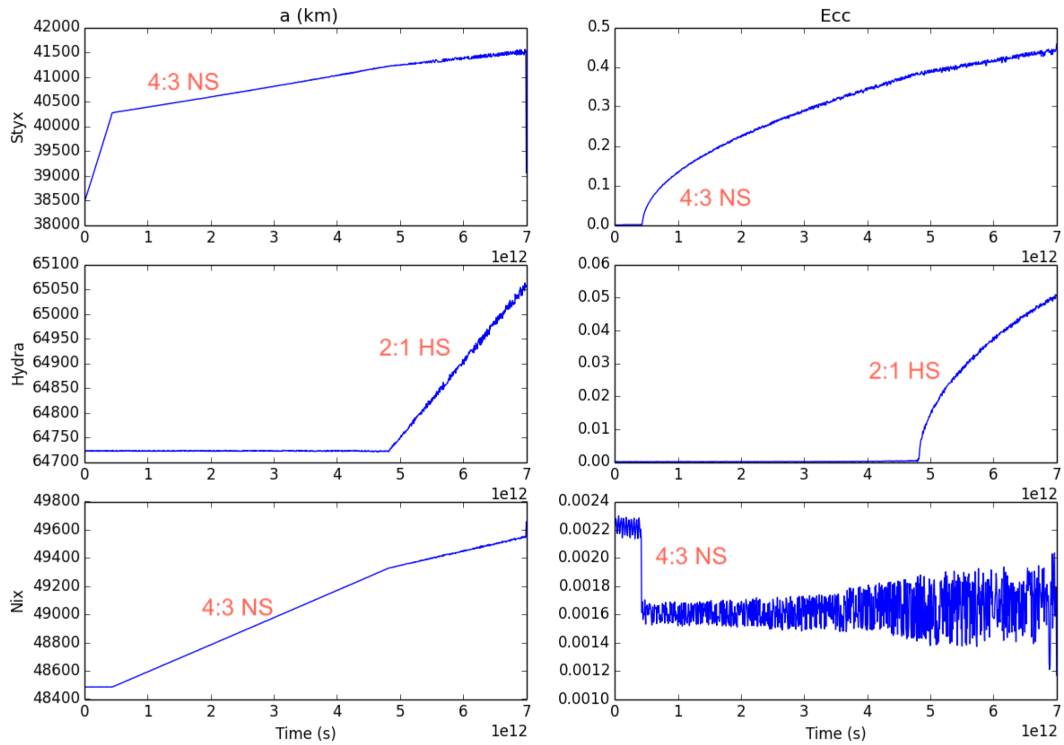

Figure 10.14: Styx, Hydra and Nix geometric semi-major axis and eccentricities over time. Styx starts captured by Charon in a inclination 3:1 resonance. Around t$\sim 5 \times 10^{11}$ s Styx captures Nix into the 4:3 mean motion resonance in eccentricity. Around t$\sim 4.8 \times 10^{12}$ s Styx captures Hydra into the 2:1 mean motion resonance in eccentricity.

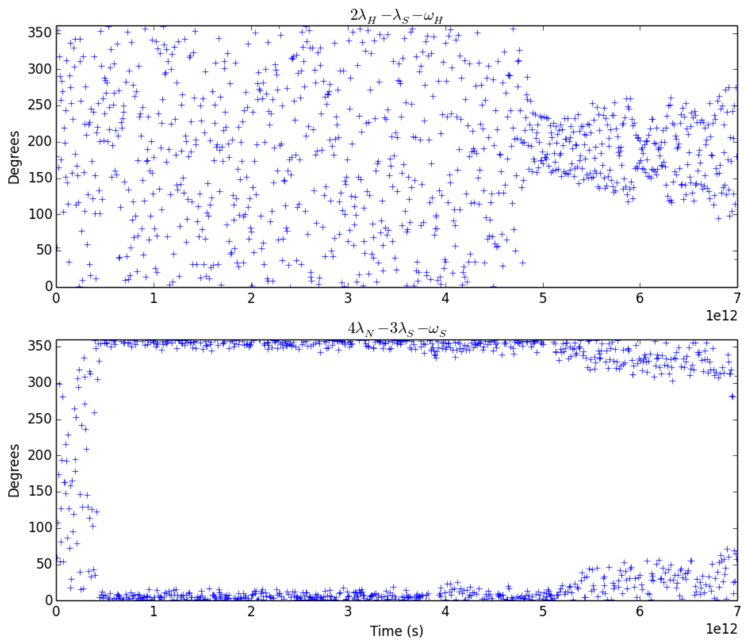

Figure 10.15: Argument of 2:1 and 4:3 resonances over time. The 2:1 resonance between Styx and Hydra angle $2\lambda_H - \lambda_S - \varpi_H$ is librating around 0 degree, starting from t$\sim 5 \times 10^{12}$ s until the end of the simulation. Around t$\sim 5 \times 10^{11}$ s Styx captured Nix into the $4\lambda_N - 3\lambda_S - \varpi_S$ resonance angle, that is librating around 180 degrees.

resonance angles over time using this setup are shown in Fig. 10.16.

In this example, we have more complex evolution with captures into different resonant arguments of the 2:1 mean motion resonance between Hydra and Styx and the 5:4 resonance, which happens more than one time.

Starting to analyze the semi-major axis of Styx, it is possible to see five captures in resonances. They correspond to the times when the migration is slower, what means the tidal force is pushing Styx as well as additional mass, the moons that are being captured.

We have assumed that Styx and Hydra start captured in the 2:1 mean motion resonance. Styx is moving slower, and Hydra is pushed outwards. As a consequence, the resonant angle $2\lambda_H - \lambda_S - \varpi_H$ appears to librate at the beginning of the simulation in Fig. 10.17. Later, the 2:1 mean motion resonance between Hydra and Styx is activated again, but this time with the Styx pericenter argument $2\lambda_H - \lambda_S - \varpi_S$. Every time Styx goes into a resonance, its eccentricity starts to grow slower as indicated on the plot.

For Styx and Nix 5:4 mean motion resonance, there are two captures during the simulation time, the first around t$\sim 1 \times 10^{13}$ s and the second around t$\sim 4.3 \times 10^{13}$ s. By the evolution of the resonant angle $5\lambda_N - 4\lambda_S - \varpi_S$, both are related to Styx eccentricity.

In this result, we have the two 2-body resonances we were looking for ($2\lambda_H - \lambda_S - \varpi_S$ and $5\lambda_N - 4\lambda_S - \varpi_S$) to form the three body resonance, but this does not happen simultaneously as we need.

Fig. 10.16 also shows how dynamic this system can be considering captures into resonances that allow eccentricity to grow.

We have tried to change the initial semi-major axes of the small moons, in order to allow the 5:4 mean motion resonance to happen earlier, along with the 2:1, but the system is extremely sensitive: every time we change when the 5:4 resonance starts, the 2:1 appears to late to overlap.

Simulation 4

Trying to avoid the result of Simulation 3, if we consider that the resonance 5:4 is more stable than the 2:1 in this case, we can make the former to happen first and maybe, when the resonance 2:1 activates, the first one will remain on.

So, on Simulation 4, we changed the Nix semimajor axis around 700 km closer to the central body. In this way, Styx initial semimajor axis is 41,154 km, Nix initial semimajor axis is 47,798 km, and Hydra's initial semimajor axis is 64,932 km. Kerberos was not include in this simulation.

The external forces still the same from Simulation 3. The semimajor axis and eccentricity for Styx, Hydra and Nix evolution are presented in Fig. 10.18.

Hydra and Styx start the simulation already captured in the 2:1 mean motion resonance $2\lambda_H - \lambda_S - \varpi_H$. This is shown by both semimajor axes growing together in Fig. 10.18 and in Fig. 10.19 (top) it is possible to see the resonant angle librating. Nix presents an increase in its eccentricity, starting around t$\sim 3.5 \times 10^{13}$ s, pointing a capture into an eccentricity mean motion resonance. This result is confirmed in Fig. 10.19 (bottom) that shows the angle $5\lambda_N - 4\lambda_S - \varpi_S$ librating.

Changing Nix initial position made it possible to have both 2:1 and 5:4 mean motion resonances activated at the same time. In this example, on the interval t$\sim [4-6] \times 10^{13}$ s

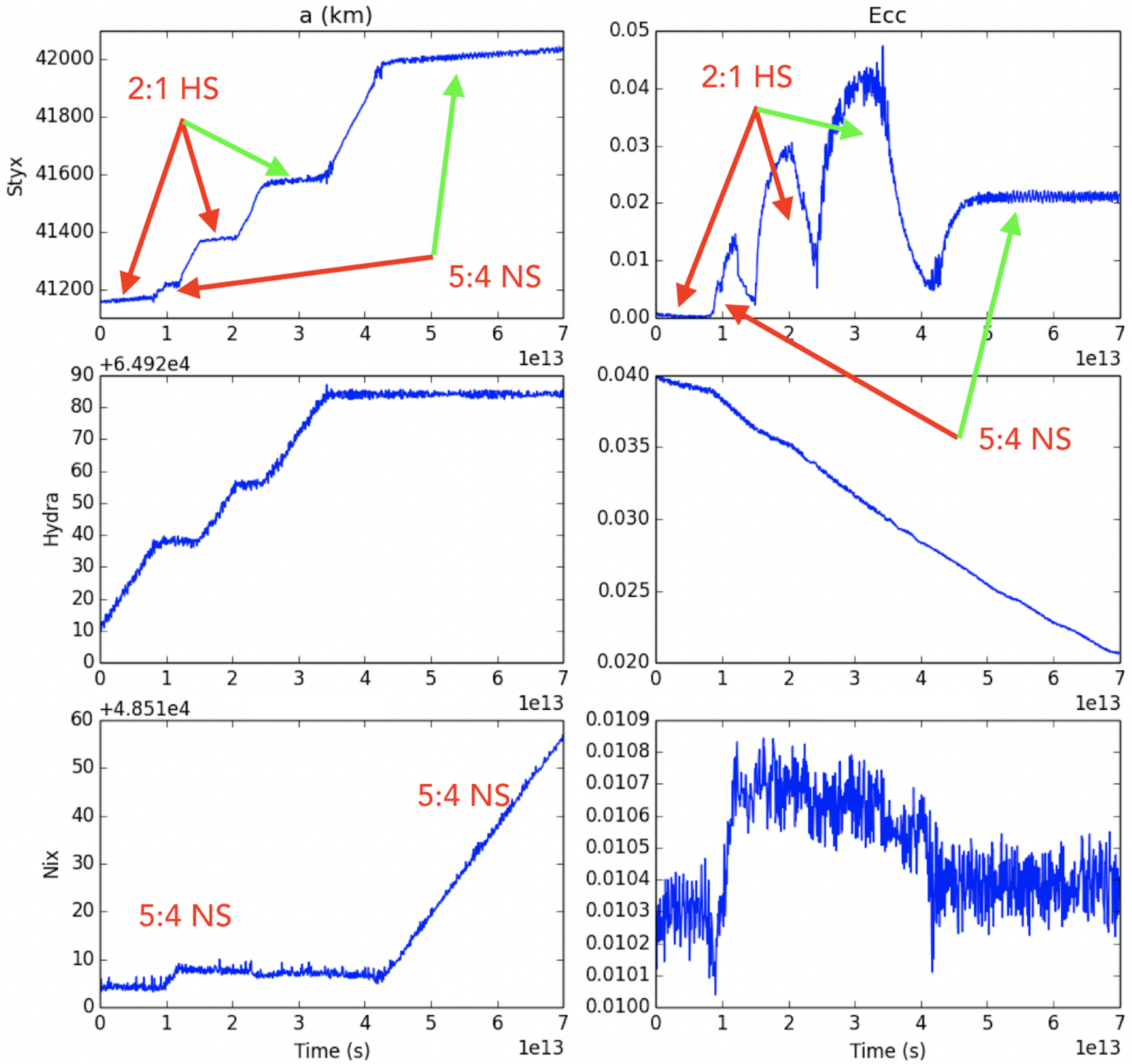

Figure 10.16: Styx, Hydra, and Nix geometric semi-major axis and eccentricities over time. Styx starts captured by Charon in a 3:1 inclination resonance, and Hydra starts captured by Styx in a 2:1 eccentricity resonance, so their semi-major axes start the simulation increasing. Around t$\sim 1\times10^{13}$ s Styx quickly captures Nix into the 5:4 mean motion resonance, and Styx eccentricity starts to grow. As a consequence, the 2:1 resonance between Styx and Hydra is turned off, and Hydra's semi-major axis ceases to grow. From t$\sim$1.5$\times10^{13}$ s to 3.5$\times10^{13}$ s, Styx captures Hydra into 2:1 resonance two times, and its effect is seen on Styx's eccentricity behavior. Around t$\sim$ 4.2 $\times$ 10^{13} s Styx captures Nix into the 5:4 mean motion resonance in eccentricity again, making Styx eccentricity grow again until it reaches an equilibrium in which tidal damping balances resonant excitation.

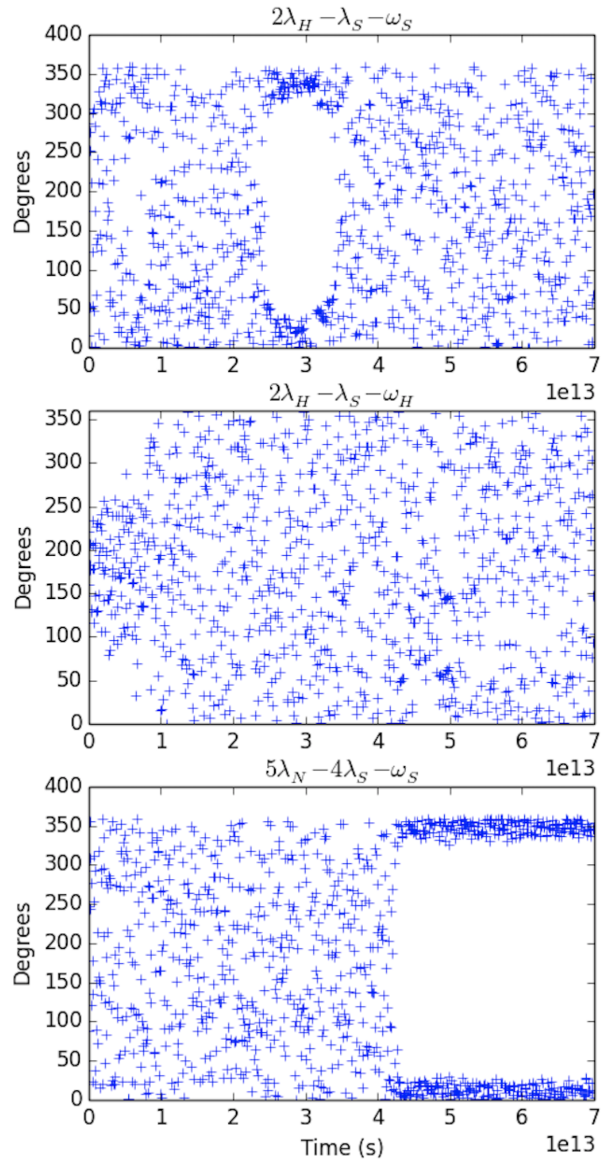

Figure 10.17: Argument of 2:1 and 5:4 resonances over time. Hydra starts captured by Styx in the $2\lambda_H - \lambda_S - \varpi_H$ resonance that is librating until around t$\sim 1\times10^{13}$ Around t$\sim 2.5\times10^{13}$ s Styx captured Hydra into the $5\lambda_N - 4\lambda_S - \varpi_S$ resonance angle, that starts to librate until it stops around t$\sim 3.5\times10^{13}$ s. Around t 4.3×10^{13} s Styx captures Nix into the $5\lambda_N - 4\lambda_S - \varpi_S$ resonance and it remains librating until the end of the simulation.

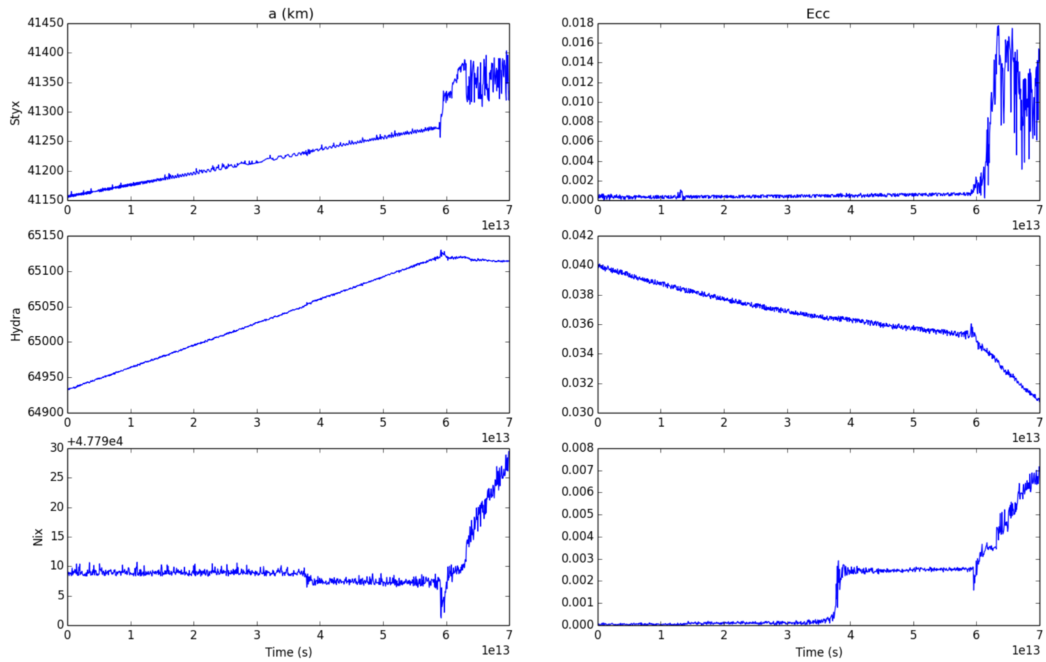

Figure 10.18: Styx, Hydra, and Nix geometric semimajor axis and eccentricities over time. Styx starts captured by Charon in a 3:1 inclination resonance, and Hydra starts captured by Styx in a 2:1 eccentricity resonance, so their semimajor axes start the simulation increasing. Around t$\sim 6\times10^{13}$ s Styx captures Nix into the 5:4 mean motion resonance in eccentricity. As a consequence, Styx and Hydra escape the 2:1 resonance.

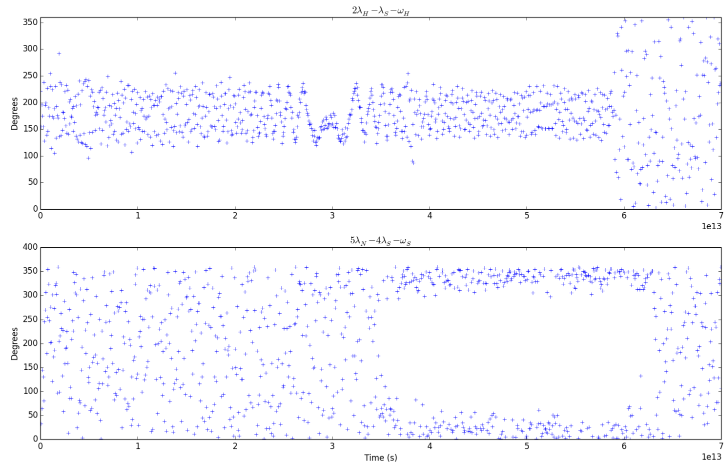

Figure 10.19: Argument of the 2:1 and 5:4 resonances over time. Hydra starts captured by Styx in the $2\lambda_H - \lambda_S - \varpi_H$ resonance that is librating until around t$\sim$ 6×10^{13} seconds. Around t$\sim$ 3.5×10^{13} s Styx captured Nix into the $5\lambda_N - 4\lambda_S - \varpi_S$ resonance, that starts to librate until it around t$\sim$ 6×10^{13} s.

we have have $5\lambda_N - 4\lambda_S - \varpi_S$ and $2\lambda_H - \lambda_S - \varpi_H$ active at the same time. Unfortunately, the last term of each resonance argument are not both on Styx pericenter, and consequently, can not result in the expected three body resonance.

Anyhow, we have parameters that allow capturing the small bodies into the exact two two body resonances arguments we need, but not at the same time. On the other hand, we have parameters that allow the capture at the same time as the resonances we want, but not for the arguments we need.

In this way, we perceive that we are close to finding the right setup to represent the complete path of the Pluto's moons from their past to the present intriguing configuration.

10.4 Final Comments on Part III

To develop the study of the origin of resonance between the satellites of Pluto, we performed N-body numerical simulations taking into account the satellites' initial conditions different from the current and evolving in time under the influence of the tidal force due of Pluto on Charon.

Using the J_2 *effective* we were able to calculate a set of corrected orbital elements, by considering a central body as a single oblate body with radius of 1187 km and a mass equivalent to the sum of the masses of Pluto and Charon, taking into account a J_2 *effective* $= 14.79$. This approximation allows us to more easily investigate the resonances actives or nearby the satellites of the Pluto-Charon system.

We showed that the small satellites could be captured into the 3:1, 4:1, 5:1, 6:1 mean motion resonances with Charon. For the case of the 5:1 and 6:1 mean motion resonances, it was possible to achieve a capture only when some non-zero eccentricity was added to Charon. Moreover, the 3:1 mean motion resonance between Charon and Styx, in inclination, was the easiest to happen among the mean motion resonances with Charon.

At this first approach, we found only one resonance between Styx and Hydra, and the resonant argument is on the Hydra's pericenter instead Styx's pericenter. We were unsuccessful at reproducing the 5:4 mean motion resonance between Styx and Nix when we consider a physical Charon presence on the system.

Then, to find other constraints on the captures besides to reproduce more captures into resonances among the small satellites, we used the J_2 *effective* approximation instead of having Charon present in the system. Later we used an artificial force to damp the orbital eccentricity of the moons captured.

We have tried to change the initial semimajor axes of the small moons in order to allow the 5:4 mean motion resonance to happen earlier, simultaneously with the 2:1. However, every time we change when the 5:4 resonance starts, the 2:1 appears later, and we have not yet been able to get them both to become active simultaneously.

We tried reducing the Nix semimajor axis by 400 km in order to change which resonance would be activated first. Changing the Nix initial position, it was possible to have both mean motion resonances 2:1 and 5:4 activated at the same time.

Unfortunately, the last term of each resonant argument was not the Styx pericenter, and consequently, could not activate the three body resonance.

Summarizing, we have parameters that allow the capture of the small bodies into the exact two 2-body resonant arguments we need, but not at the same time. On the other hand, we have other parameters that allow the capture at the same time as the resonances we want, but not for the arguments we need.

We believe that a solution is possible but that it will require a more thorough search. The magnitude of the tidal force, the magnitude of the drag force, and the initial position of all moons are the variables of this problem, making it hard to match all those at the same time. Large uncertainties make this search a bit like looking for a needle in a haystack.

Nevertheless, we perceive that we are close to finding the right parameters to represent all the path of the Pluto's moons from their past to the nowadays intriguing configuration and have ideas to test that may bring us to a viable scenario.

Some of those ideas are applying a damping eccentricity force on Nix and lining up the captures to happen a little bit earlier or later, provoking a bigger or smaller eccentricity on the small satellites that will allow the capture to happen when the body passes through the resonance location.

Chapter 11

Final Remarks

In this work, we have passed through different studies involving the mean motion resonances of small satellites.

In Part I we presented a quick review on Saturn's satellites Prometheus and Pandora lags problem and analyzed the ratio between them ($\mathcal{Q} = \left|\Delta\lambda_{\rm pro}/\Delta\lambda_{\rm pan}\right|$). The 121:118 mean motion resonance between Prometheus and Pandora is the explanation proposed by Goldreich & Rappaport (2003b) for the lags. Through the conservation of the angular momentum, we expect that the ratio of the lags due to this mutual interaction must be almost constant. However, the values obtained using observational data fit French et al. (2003), $\mathcal{Q}_{\rm obs}$ does not agree with the assumed masses $m_{\rm pan}/m_{\rm pro} = 0.56$ and is not even nearly constant. It presents a robust linear increasing rate given by $\mathcal{Q}_{\rm obs}(t) = 0.667 + 0.013t$, with t given in years. In this way, we show that only the gravitational interaction between the satellites does not fully explain the lags values, indicating that a non-mutual mechanism should provoke at least a mean motion changing of $0.45°$/year, also affecting Prometheus or Pandora, contributes to the lag values. We have listed a set of known gravitational interactions involving Prometheus or Pandora.

In Part II, we performed the astrometry of the satellite Daphnis using the CAVIAR software in a selected set of images from the ISS-NAC camera of Cassini spacecraft. The results indicated that only one orbit does not describe Daphnis positions during the years of the Cassini mission. Instead, it changed through three different orbits, implying Daphnis has been unpredictably changing orbit. So, we have investigated if Daphnis is orbiting in a stable region, and for this, we implemented numerical simulations considering Saturn plus five satellites: Daphnis, Atlas, Prometheus, Pandora, and Mimas. By computing the evolution of the Fast Lyapunov Indicator FLI over time for Daphnis orbit, we showed that the moon is on a chaotic orbit with a Lyapunov time of $\sim$22 years. It is a short Lyapunov time, implying that Daphnis is within a highly chaotic region. Thereafter, we investigated the existence of some possible resonances between Daphnis and other moons that could be relevant for Daphnis' orbital motion. It was found that Prometheus and Atlas and 129:125 and 157:155 mean motion resonant angles present some features that could indicate chaos. Later, we found that when Prometheus and Atlas are not included in the numerical simulation, Daphnis' orbit became regular, reinforcing the suggestion that both satellites are playing a role in Daphnis' chaotic behavior.

In Part III, we presented a study of the origin of resonance between the satellites of Pluto.

We performed N-body numerical simulations considering the small satellites and Charon at initial semimajor axes closer to Pluto than their current positions and evolved the system in time under the influence of the tidal force due to Pluto-Charon. Using the J_2 *effective*, we were able to calculate a set of orbital elements instantly on time from the output state vector from the simulation by considering a central object as a single oblate body with a radius of 1187 km and a mass equivalent to the sum of the masses of Pluto and Charon. We showed that the small satellites can be captured into the 3:1, 4:1, 5:1, 6:1 mean motion resonances with Charon. For the case of the 5:1 and 6:1 mean motion resonances, it was possible to achieve a capture only when some artificial eccentricity was added to Charon. Moreover, the 3:1 mean motion resonance between Charon and Styx, in inclination, was the easiest to happen. To find the three body resonance 3:5:2 among Styx, Nix, and Hydra, we looked for two particular resonances among them: 2:1 between Styx and Hydra and 5:4 between Nix and Styx. For several simulations, it was found only one resonance between Styx and Hydra, and not those we need to form the three bodies one.

Then, to find other constraints on the captures into resonances among the small satellites, besides, the use of the J_2 *effective* simulations' output, we also adopted the J_2 *effective* approximation idea through all the evolution. In other words, instead of having Charon present during the simulation, we suppressed it and replaced Pluto for a body with Pluto and Charon masses and a J_2 coefficient, as we have said earlier. Also, we used an artificial force to damp the orbital's eccentricity of the moons captured and have changed the initial semimajor axes of them in order to allow the 5:4 and 2:1 mean motion to happen simultaneously. Unfortunately, it turned out to be harder than we expected.

Summarizing, we have parameters that allow the capture of the small bodies into the exact two 2-body resonant arguments we need, but not at the same time. On the other hand, we have other parameters that allow the capture at the same time as the resonances we want, but not for the arguments we need.

The magnitude of the tidal force, the magnitude of the drag force, and the initial position of all moons are the variables of this problem, making it hard to suit all those simultaneously. That is why we had passed through each mechanism individually, trying to identify in what conditions such things can happen.

In this way, we perceive that we are close to find the right parameters to represent all the paths of the Pluto's moons from their past to the current intriguing configuration.

Some different ideas may be tested to bring us to the present scenario. Some of these ideas are applying a damping eccentricity force on Nix and allowing the captures to happen a little bit earlier or later, provoking a bigger or smaller eccentricity on the small satellites that will allow the capture to happen when the body passes through the resonance location.

Bibliography

AMARANTE, A. *Origem e Estabilidade de Satélites Planetários: alguns casos peculiares*. Ph.D. thesis, UNESP - Faculdade de Engenharia de Guaratinguetá, 2017.

BARBARA, J. M. & ESPOSITO, L. W. Moonlet collisions and the effects of tidally modified accretion in saturn's f ring. *Icarus*, 160:161–171, 2002.

BORDERIES-RAPPAPORT, N. & LONGARETTI, P. Y. Test particle motion around an oblate planet. Icarus, 107:129, 1994.

BOSH, A. S. & RIVKIN, A. S. Observations of saturn's inner satellites during the may 1995 ring-plane crossing. *Science*, 272:518–521, 1996.

BROWN, M. E., TRUJILLO, C. A., & RABINOWITZ, D. 2003 EL_61, 2003 UB_313, and 2005 FY_9. IAU Circ., 8577:1, 2005.

BROZOVIĆ, M., SHOWALTER, M. R., JACOBSON, R. A., & BUIE, M. W. The orbits and masses of satellites of pluto. Icarus, 246:317–329, 2015.

BUIE, M. W., GRUNDY, W. M., & THOLEN, D. J. ASTROMETRY AND ORBITS OF NIX, KERBEROS, AND HYDRA. *The Astronomical Journal*, 146(6):152, 2013.

BUIE, M. W., GRUNDY, W. M., YOUNG, E. F., YOUNG, L. A., & STERN, S. A. Orbits and photometry of pluto's satellites: Charon, s/2005 p1, and s/2005 p2. *The Astronomical Journal*, 132(1):290–298, 2006.

BULIRSCH, R. & STOER, J. *Introdution to Numerical Analysis*. Springer Verlag, New York, 1980.

CANUP, R. M. A giant impact origin of pluto-charon. *Science*, 307:546–550, 2005.

CHAMBERS, J. E. A hybrid symplectic integrator that permits close encounters between massive bodies. MNRAS, 304:793–799, 1999.

CHENG, W. H., PEALE, S. J., & LEE, M. H. On the origin of pluto's small satellites by resonant transport. Icarus, 241:180–189, 2014.

CHRISTY, J. W. & HARRINGTON, R. S. The satellite of pluto. AJ, 83:1005, 1978.

Cooper, N. J., Lainey, V., Meunier, L.-E., Murray, C. D., Zhang, Q.-F., Baillie, K., Evans, M. W., Thuillot, W., & Vienne, A. The caviar software package for the astrometric reduction of cassini ISS images: description and examples. *Astronomy & Astrophysics*, 610:A2, 2018.

Cooper, N. J. & Murray, C. D. Dynamical influences on the orbits of prometheus and pandora. AJ, 127:1204–1217, 2004.

Cooper, N. J., Renner, S., Murray, C. D., & Evans, M. W. Saturn#700s inner satellites: Orbits, masses, and the chaotic motion of atlas from new cassini imaging observations. AJ, 149:27, 2015.

Cruz, C. *Estudo da Dinâmica do Sistema Prometeu – Pandora – Anel F de Saturno*. Master's thesis, Faculdade de Engenharia do Campus de Guaratinguetá, Universidade Estadual Paulista, 2004.

Cuzzi, J. N. & Burns, J. A. Charged particle depletion surrounding saturn's f ring - evidence for a moonlet belt? *Icarus*, 74:284–324, 1988.

dos Santos, P. M. P., Morbidelli, A., & Nesvorný, D. Dynamical capture in the pluto–charon system. *Celestial Mechanics and Dynamical Astronomy*, 114(4):341–352, 2012.

Esposito, L. Drunken shepherds: Random walk models for pandora and prometheus. In A. Tzanis, editor, *EGS General Assembly Conference Abstracts*, volume 27 of *EGS General Assembly Conference Abstracts*, page 5215. 2002.

Evans, M. W. *The Determination of Orbits From Spacecraft Imaging*. Ph.D. thesis, Queen Mary College, University of London, 2001.

Everhart, E. An efficient integrator that uses gauss-radau spacings. In A. Carusi & G. B. Valsecchi, editors, *Dynamics of Comets: Their Origin and Evolution, Proceedings of IAU Colloq. 83, held in Rome, Italy, June 11-15, 1984. Edited by Andrea Carusi and Giovanni B. Valsecchi. Dordrecht: Reidel, Astrophysics and Space Science Library. Volume 115, 1985, p.185*, page 185. 1985.

French, R. G., McGhee, C. A., Dones, L., & Lissauer, J. J. Saturn's wayward shepherds: the peregrinations of prometheus and pandora. *Icarus*, 162:143–170, 2003.

Froeschlé, C., Gonczi, R., & Lega, E. The fast lyapunov indicator: a simple tool to detect weak chaos. application to the structure of the main asteroidal belt. *Planetary and Space Science*, 45(7):881–886, 1997.

Froeschlé, C. & Lega, E. On the structure of symplectic mappings. the fast lyapunov indicator: a very sensitive tool. *Celestial Mechanics and Dynamical Astronomy*, 78:167–195, 2000.

Gallardo, T., Coito, L., & Badano, L. Planetary and satellite three body mean motion resonances. Icarus, 274:83–98, 2016.

Giorgini, J. D., Yeomans, D. K., Chamberlin, A. B., Chodas, P. W., Jacobson, R. A., Keesey, M. S., Lieske, J. H., Ostro, S. J., Standish, E. M., & Wimberly, R. N. Bulletin of the american astronomical society. In *Bulletin of the AAA*, page 1158. 1996.

Goldreich, P. & Rappaport, N. Chaotic motions of prometheus and pandora. *Icarus*, 162:391–399, 2003a.

Goldreich, P. & Rappaport, N. Origin of chaos in the prometheus-pandora system. *Icarus*, 166:320–327, 2003b.

Goldreich, P. & Tremaine, S. Towards a theory for the uranian rings. Nature, 277:97–99, 1979.

Hedman, M. M. & Carter, B. J. A curious ringlet that shares prometheus' orbit but precesses like the f ring. Icarus, 281:322–333, 2017.

Hedman, M. M. & Nicholson, P. D. Axisymmetric density waves in saturn's rings. *Monthly Notices of the Royal Astronomical Society*, 485(1):13–29, 2019.

Høg, E., Fabricius, C., Makarov, V. V., Urban, S., Corbin, T., Wycoff, G., Bastian, U., Schwekendiek, P., & Wicenec, A. The Tycho-2 catalogue of the 2.5 million brightest stars. A&A, 355:L27–L30, 2000.

Jacobson, R. A. The small saturnian satellites – chaos and conundrum. In *AAS/Division of Dynamical Astronomy Meeting #45*, volume 45 of *AAS/Division of Dynamical Astronomy Meeting*, page 304.05. 2014.

Jacobson, R. A., Antreasian, P. G., Bordi, J. J., Criddle, K. E., Ionasescu, R., Jones, J. B., Mackenzie, R. A., Meek, M. C., Parcher, D., Pelletier, F. J., Owen, J., W. M., Roth, D. C., Roundhill, I. M., & Stauch, J. R. The Gravity Field of the Saturnian System from Satellite Observations and Spacecraft Tracking Data. AJ, 132(6):2520–2526, 2006.

Jacobson, R. A. & French, R. G. Orbits and masses of Saturn's coorbital and F-ring shepherding satellites. Icarus, 172:382–387, 2004.

Jacobson, R. A., Spitale, J., Porco, C. C., Beurle, K., Cooper, N. J., Evans, M. W., & Murray, C. D. Revised Orbits of Saturn's Small Inner Satellites. AJ, 135:261–263, 2008.

Kaasalainen, M. & Tanga, P. Photocentre offset in ultraprecise astrometry: Implications for barycentre determination and asteroid modelling. A&A, 416:367–373, 2004.

Kenyon, S. J. & Bromley, B. C. The formation of pluto's low-mass satellites. AJ, 147:8, 2014.

Lee, M. H. & Peale, S. J. On the orbits and masses of the satellites of the pluto charon system. Icarus, 184:573–583, 2006.

Lissauer, J. J. & Peale, S. J. The production of 'braids' in saturn's f ring. Icarus, 67:358–374, 1986.

Lithwick, Y. & Wu, Y. On the origin of pluto's minor moons, nix and hydra. *arXiv e-prints*, 2008.

McGhee, C. A. *Comet Shoemaker-Levy's 1994 collision with Jupiter and Saturn's 1995 ring plane crossings*. Ph.D. thesis, CORNELL UNIVERSITY, 2000.

McGhee, C. A., Nicholson, P. D., French, R. G., & Hall, K. J. Hst observations of saturnian satellites during the 1995 ring plane crossings. *Icarus*, 152:282–315, 2001.

Morgado, B. E. *Estudo Astrométrico dos Satélites Galileanos de Júpiter*. Ph.D. thesis, Observatório Nacional, 2019.

Murray, C. D. & Dermott, S. F. *Solar System Dynamics*. Cambridge University Press, Cambridge, 1999.

Murray, C. D. & Giuliatti Winter, S. M. Periodic collisions between the moon prometheus and saturn's f ring. Nature, 380:139–141, 1996.

Nicholson, P. D., Showalter, M. R., Dones, L., French, R. G., Larson, S. M., Lissauer, J. J., McGhee, C. A., Seitzer, P., Sicardy, B., & Danielson, G. E. Observations of saturn's ring-plane crossings in august and november 1995. *Science*, 272:509–515, 1996.

Porco, C. C. S/2005 s 1. IAU Circ., 8524, 2005.

Porco, C. C., Baker, E., Barbara, J., Beurle, K., Brahic, A., Burns, J. A., Charnoz, S., Cooper, N., Dawson, D. D., Del Genio, A. D., Denk, T., Dones, L., Dyudina, U., Evans, M. W., Giese, B., Grazier, K., Helfenstein, P., Ingersoll, A. P., Jacobson, R. A., Johnson, T. V., McEwen, A., Murray, C. D., Neukum, G., Owen, W. M., Perry, J., Roatsch, T., Spitale, J., Squyres, S., Thomas, P., Tiscareno, M., Turtle, E., Vasavada, A. R., Veverka, J., Wagner, R., & West, R. Cassini imaging science: Initial results on saturn's rings and small satellites. *Science*, 307:1226–1236, 2005.

Poulet, F. & Sicardy, B. Dynamical evolution of the prometheus-pandora system. MNRAS, 322:343–355, 2001.

Rauch, K. P. & Hamilton, D. P. The hnbody package for symplectic integration of nearly-keplerian systems. In *AAS/Division of Dynamical Astronomy Meeting #33*, volume 34 of *Bulletin of the American Astronomical Society*, page 938. 2002.

Renner, S., Cooper, N. J., El Moutamid, M., Sicardy, B., Vienne, A., Murray, C. D., & Saillenfest, M. Origin of the chaotic motion of the saturnian satellite atlas. AJ, 151:122, 2016.

Renner, S. & Sicardy, B. Consequences of the chaotic motions of prometheus and pandora. In *AAS/Division of Dynamical Astronomy Meeting 34*, volume 35 of *Bulletin of the American Astronomical Society*, page 1044. 2003.

Renner, S. & Sicardy, B. Use of the geometric elements in numerical simulations. *Celestial Mechanics and Dynamical Astronomy*, 94:237–248, 2006.

Renner, S., Sicardy, B., & French, R. G. Prometheus and pandora: masses and orbital positions during the cassini tour. Icarus, 174:230–240, 2005.

Showalter, M., Weaver, H., Buie, M., Merline, D., Mutchler, M., Soummer, R., Steffl, A., Stern, S. A., Throop, H., & Young, L. Update on pluto's tiniest moons. In *EGU General Assembly Conference Abstracts*, volume 15 of *EGU General Assembly Conference Abstracts*, pages EGU2013–13786. 2013.

Showalter, M. R., Dones, L., & Lissauer, J. J. Interactions between prometheus and the f ring. In *AAS/Division of Dynamical Astronomy Meeting 31*, volume 31 of *Bulletin of the American Astronomical Society*, page 1228. 1999a.

Showalter, M. R., Dones, L., & Lissauer, J. J. Revenge of the sheep: effects of saturn's f ring on the orbit of prometheus. In *Bulletin of the American Astronomical Society*, volume 31 of *Bulletin of the American Astronomical Society*, page 1141. 1999b.

Showalter, M. R. & Hamilton, D. P. Resonant interactions and chaotic rotation of pluto's small moons. Nature, 522:45–49, 2015.

Showalter, M. R., Hamilton, D. P., Stern, S. A., Weaver, H. A., Steffl, A. J., & Young, L. A. New satellite of (134340) pluto: S/2011 (134340) 1. *Central Bureau Electronic Telegrams*, 2769, 2011.

Showalter, M. R., Weaver, H. A., Stern, S. A., Steffl, A. J., Buie, M. W., Merline, W. J., Mutchler, M. J., Soummer, R., & Throop, H. B. New satellite of (134340) pluto: S/2012 (134340) 1. IAU Circ., 9253, 2012.

Spahn, F., Hoffmann, H., Rein, H., Seiss, M., Sremčević, M., & Tiscareno, M. S. *Moonlets in Dense Planetary Rings*, pages 157–197. 2018.

Spitale, J. N., Jacobson, R. A., Porco, C. C., & Owen, W. M., Jr. The Orbits of Saturn's Small Satellites Derived from Combined Historic and Cassini Imaging Observations. AJ, 132:692–710, 2006.

Stern, S. A., Bagenal, F., Ennico, K., Gladstone, G. R., Grundy, W. M., McKinnon, W. B., Moore, J. M., Olkin, C. B., Spencer, J. R., Weaver, H. A., Young, L. A., Andert, T., Andrews, J., Banks, M., Bauer, B., Bauman, J., Barnouin, O. S., Bedini, P., Beisser, K., Beyer, R. A., Bhaskaran, S., Binzel, R. P., Birath, E., Bird, M., Bogan, D. J., Bowman, A., Bray, V. J., Brozovic, M., Bryan, C., Buckley, M. R., Buie, M. W., Buratti, B. J., Bushman, S. S., Calloway, A., Carcich, B., Cheng, A. F., Conard, S., Conrad, C. A., Cook, J. C., Cruikshank, D. P., Custodio, O. S., Dalle Ore, C. M., Deboy, C., Dischner, Z. J. B., Dumont, P., Earle, A. M., Elliott, H. A., Ercol, J., Ernst, C. M., Finley, T., Flanigan, S. H., Fountain, G., Freeze, M. J., Greathouse, T., Green, J. L., Guo, Y., Hahn, M., Hamilton, D. P., Hamilton, S. A., Hanley, J., Harch, A., Hart, H. M., Hersman, C. B., Hill, A., Hill, M. E., Hinson, D. P., Holdridge, M. E., Horanyi, M., Howard, A. D., Howett, C. J. A., Jackman, C., Jacobson, R. A., Jennings, D. E., Kammer, J. A., Kang, H. K., Kaufmann, D. E., Kollmann, P., Krimigis, S. M., Kusnierkiewicz, D., Lauer, T. R., Lee, J. E., Lindstrom, K. L., Linscott, I. R., Lisse, C. M., Lunsford, A. W., Mallder, V. A., Martin, N., McComas, D. J., McNutt, R. L., Mehoke, D., Mehoke, T., Melin, E. D., Mutchler, M., Nelson, D., Nimmo, F., Nunez, J. I., Ocampo, A., Owen, W. M., Paetzold, M., Page, B., Parker, A. H., Parker, J. W., Pelletier, F., Peterson, J., Pinkine, N., Piquette, M., Porter, S. B., Protopapa, S., Redfern, J., Reitsema, H. J., Reuter, D. C., Roberts, J. H., Robbins, S. J., Rogers, G., Rose, D., Runyon, K., Retherford, K. D., Ryschkewitsch, M. G., Schenk, P., Schindhelm, E., Sepan, B., Showalter, M. R., Singer, K. N., Soluri, M., Stanbridge, D., Steffl, A. J., Strobel, D. F., Stryk, T., Summers, M. E., Szalay, J. R., Tapley, M., Taylor, A., Taylor, H., Throop, H. B., Tsang, C. C. C., Tyler, G. L., Umurhan, O. M., Verbiscer, A. J., Versteeg, M. H., Vincent, M., Webbert, R., Weidner, S., Weigle, G. E., White, O. L., Whittenburg, K., Williams, B. G., Williams, K., Williams, S., Woods, W. W., Zangari, A. M., & Zirnstein, E. The pluto system: Initial results from its exploration by new horizons. *Science*, 350:aad1815, 2015.

Stern, S. A., Grundy, W. M., McKinnon, W. B., Weaver, H. A., & Young, L. A. The pluto system after new horizons. *Annual Review of Astronomy and Astrophysics*, 56(1):357–392, 2018.

Synnott, S. P., Peters, C. F., Smith, B. A., & Morabito, L. A. Orbits of the small satellites of saturn. *Science*, 212:191, 1981.

Synnott, S. P., Terrile, R. J., Jacobson, R. A., & Smith, B. A. Orbits of saturn's f ring and its shepherding satellites. *Icarus*, 53:156–158, 1983.

Tajeddine, R., Nicholson, P. D., Tiscareno, M. S., Hedman, M. M., Burns, J. A., & El Moutamid, M. Dynamical phenomena at the inner edge of the keeler gap. Icarus, 289:80–93, 2017.

Thomas, P. Sizes, shapes, and derived properties of the saturnian satellites after the cassini nominal mission. *Icarus*, 208(1):395–401, 2010.

Tiscareno, M. S., Nicholson, P. D., Cuzzi, J. N., Spilker, L. J., Murray, C. D., Hedman, M. M., Colwell, J. E., Burns, J. A., Brooks, S. M., Clark, R. N., Cooper, N. J., Deau, E., Ferrari, C., Filacchione, G., Jerousek, R. G., Le Mouélic, S., Morishima, R., Pilorz, S., Rodriguez, S., Showalter, M. R., Badman, S. V., Baker, E. J., Buratti, B. J., Baines, K. H., & Sotin, C. Close-range remote sensing of saturn's rings during cassini's ring-grazing orbits and grand finale. *Science*, 364(6445), 2019.

Vieira Martins, R. The perturbation of triton on nereid's motion. In R. Vieira Martins, D. Lazzaro, & W. Sessin, editors, *Orbital Dynamics of Natural and Artificial Objects*. 1989.

Walsh, K. J. & Levison, H. F. Formation and evolution of pluto's small satellites. AJ, 150:11, 2015.

Ward, W. R. & Canup, R. M. Forced resonant migration of pluto's outer satellites by charon. *Science*, 313:1107–1109, 2006.

Weaver, H. A., Buie, M. W., Buratti, B. J., Grundy, W. M., Lauer, T. R., Olkin, C. B., Parker, A. H., Porter, S. B., Showalter, M. R., Spencer, J. R., Stern, S. A., Verbiscer, A. J., McKinnon, W. B., Moore, J. M., Robbins, S. J., Schenk, P., Singer, K. N., Barnouin, O. S., Cheng, A. F., Ernst, C. M., Lisse, C. M., Jennings, D. E., Lunsford, A. W., Reuter, D. C., Hamilton, D. P., Kaufmann, D. E., Ennico, K., Young, L. A., Beyer, R. A., Binzel, R. P., Bray, V. J., Chaikin, A. L., Cook, J. C., Cruikshank, D. P., Dalle Ore, C. M., Earle, A. M., Gladstone, G. R., Howett, C. J. A., Linscott, I. R., Nimmo, F., Parker, J. W., Philippe, S., Protopapa, S., Reitsema, H. J., Schmitt, B., Stryk, T., Summers, M. E., Tsang, C. C. C., Throop, H. H. B., White, O. L., & Zangari, A. M. The small satellites of pluto as observed by new horizons. *Science*, 351:aae0030, 2016.

Weaver, H. A., Stern, S. A., Mutchler, M. J., Steffl, A. J., Buie, M. W., Merline, W. J., Spencer, J. R., Young, E. F., & Young, L. A. Discovery of two new satellites of pluto. Nature, 439:943–945, 2006.

Winter, S. M. G., Sfair, R., Mourão, D. C., & Bastos, T. A. Analysing the new saturnian rings, r/2004 s1 and r/2004 s2. *Earth, Moon, and Planets*, 97(3-4):189–201, 2006.

Woo, J. M. Y. & Lee, M. H. On the early in situ formation of pluto's small satellites. AJ, 155:175, 2018.

Zacharias, N., Finch, C., & Frouard, J. UCAC5: New Proper Motions Using Gaia DR1. AJ, 153:166, 2017.

Zhang, K. & Hamilton, D. P. Orbital resonances in the inner neptunian system. *Icarus*, 188(2):386–399, 2007.

Zhang, K. & Hamilton, D. P. Orbital resonances in the inner neptunian system. *Icarus*, 193(1):267–282, 2008.